Spectral functions from lattice QCD at finite temperature

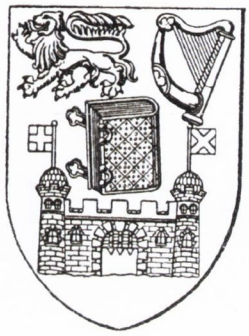

Tim Harris
School of Mathematics
Trinity College Dublin

A thesis submitted for the degree of
Doctor of Philosophy
September 2014

I declare that this thesis has not been submitted as an exercise for a degree at this or any other university and it is entirely my own work. I agree to deposit this thesis in the University's open access institutional repository or allow the library to do so on my behalf, subject to Irish Copyright Legislation and Trinity College Library conditions of use and acknowledgement.

Summary

An investigation of the bottomonium spectrum above and below the QCD deconfinement crossover temperature, T_c, was performed using a non-relativistic treatment of the heavy quark on anisotropic lattices with $N_f = 2 + 1$ flavours of Wilson-clover fermion and a Symanzik-improved gauge action. The spectral functions were reconstructed from the Euclidean correlators using two Bayesian methods to tackle the ill-posed inverse problem, known as the Maximum Entropy Method (MEM) and the Bayesian Reconstruction (BR) method. The survival of the S wave ground-state well into the deconfined phase up to at least $1.90T_c$ was concluded from both methods. In the less tightly bound P wave channel, a discrepancy was observed in the interpretation of the effect of the thermal medium. MEM suggested that the P wave ground-state dissociates immediately in the deconfined phase. However, some remnant of this state was observed at all temperatures up to $1.90T_c$ in the spectral function reconstructed with the BR method. On comparing the spectral function in this channel with the reconstruction of the free lattice spectral function, the significance of this remnant is less clear. Finally, the spectral functions of correlators of Wilson lines were examined at finite temperature from which the medium-modified heavy-quark potential can be extracted in a systematic way. Above the crossover temperature, effects that could be interpreted as colour-Debye screening and Landau damping are visible, but systematic uncertainties of the reconstruction suggest further investigation is required at the highest temperature.

Acknowledgements

I wish to thank my supervisor Sinéad for her continued support throughout the past three years. This work would not have been possible without the patience of the members of the FASTSUM collaboration and in particular I thank Gert Aarts, Chris Allton and Simon Hands for their hospitality during my stay in Swansea. I learned a lot from the permanent and transient members the lattice group at Trinity College, so I extend my thanks to Mike, Stefan, John, Jonivar and Christopher. Much of this work could not have been completed without the expertise of Alexander Rothkopf and Yannis Burnier who graciously gave me permission to reproduce the preliminary results on the heavy-quark potential and allowed me access to their implementation of the BR method. My colleagues Mattia Dalla Brida, Pol Vilaseca and Graham Moir were a great support during my time in the School of Maths. My friends and family deserve everything for keeping me going this year.

Contents

1 QCD at finite temperature

The success of the model-independent framework of thermodynamics has hardly been surpassed as a physical theory. Its power lies in its generality which casts a system's bulk properties in terms of the same thermodynamic variables and potentials which can be used across a wide range of scales from nuclear to cosmological in size. Investigating these general properties, which arise from the statistical treatment of large numbers of particles, or degrees of freedom, has successfully expanded the remit of classical, quantum and relativistic models. Macroscopic ensembles are worth examining in their own right due to the vast array of phenomena, such as new phases and collective dynamics, observed in nature. Furthermore, the study of bulk properties offers an arena to constrain and test the underlying dynamics of new or established physical models by comparing predictions of thermodynamic observables with experimental measurements.

In particular, non-Abelian gauge theories have a rich phase structure owing to their inherently complex interactions and vacuum structure. *Quantum chromodynamics (QCD)* is the prototypical strongly-coupled gauge theory coupled to fermions which exhibits asymptotic freedom [1, 2] and low-energy confinement [3]. It is understood to describe the interactions between quarks, their binding to form nucleons, and consequently explain the origin of most of the mass of the everyday objects around us.

Asymptotic freedom suggests some change in the properties of QCD matter at temperatures on the order of the hadronic scale $\approx$ 1GeV, when quarks and gluons become liberated from hadronic degrees of freedom as the running coupling diminshes. One realization of such temperatures was during the hot and dense phase of the universe just after the Big Bang, when the expanding universe passed through temperatures on the order of the hadronic scale as it cooled and the matter content comprised light quarks and leptons. In order to correctly model the evolution of the early universe it is neccessary to account for the relevant dynamics of these degrees of freedom at temperatures above the con-

tinuous crossover to the *quark-gluon plasma (QGP)*, formed around 150MeV [4]. Additionally, the description of the dense QCD matter found in compact stars requires the *equation of state* – a relation between thermodynamic state variables – at finite quark or baryon chemical potential. QCD thermodynamics is therefore relevant in astrophysical and cosmological contexts in order to describe such systems from first principles.

While these applications motivate the study of quarks and gluons at high temperatures and density, human ingenuity has circumvented the non-observability of the QGP in the early universe with the possiblity of its direct creation in terrestrial collider experiments. Generically, these experiments, from the Super Proton Synchrontron (SPS) at CERN and the Relativistic Heavy Ion Collider (RHIC) at BNL to the Large Hadron Collider (LHC) at CERN, collide nuclei with a large enough number of participants to warrant a thermodynamic treatment, complementary to collider experiments with hadron or lepton projectiles at the energy frontier. These experiments provide further opportunities for stringent tests of QCD as the correct theory of the strong interaction through determination of a number of thermodynamic quantities and the modification of its spectrum outside the vacuum phase.

In addition to providing a test-bed for fundamental physics theory, collider experiments simultaneously require diagnostics such as tools to calibrate the temperature and density achieved in collisions. Another valuable challenge for theorists and phenomenologists is to provide observables which can be used to deduce the existence of exotic states of matter. In particular, this work is largely motivated by providing reliable data for such thermometers [5]. In this expository chapter the established phase structure of QCD is briefly reviewed after which the dynamics of the heavy-ion collision is outlined with a motivation for using bound states of a heavy quark and antiquark, or *heavy quarkonium*, as probes of the plasma.

1.1 Phase structure of QCD

A simple heuristic argument for a transition to a new state of matter at high densities exists analogous to the one which suggests the phase transition at temperatures on the order of the hadronic scale from renormalization group arguments. If the density of matter is increased beyond nuclear density, the constituent quarks necessarily lose the identity of their parent nucleon and are consequently liberated, leading again to a *deconfined phase*. Furthermore, Hagedorn's argument for a limiting temperature for hadronic matter, based on the exponential growth

of the number of states with temperature, also hints at the emergence of new degrees of freedom at temperatures of a few hundred MeV [6].

More precisely, the phase structure can be understood through the spontaneous breaking of global symmetries of QCD in two limits. First, in the quenched limit with static quarks, namely in pure gauge theory, QCD possesses an exact global *centre symmetry* of the gauge group, $\mathbb{Z}_3$. The generators of the centre symmetry form the Cartan subalgebra of $\mathfrak{su}(3)$, the algebra of the gauge group.

At high temperatures, this symmetry is spontaneously broken in the deconfined phase. An interpretation of the spontaneous breaking of this symmetry can be made through an order parameter for this symmetry, the *Polyakov loop*. The Polyakov loop, $P(\mathbf{x})$, is a Wilson loop with with non-trivial winding around the compact temporal direction,

$$P(\mathbf{x}) = \mathcal{P} e^{-\oint_\gamma \mathrm{d}x^\mu A_\mu}, \tag{1.1}$$

where $\mathcal{P}$ denotes that the path-ordering of the gauge potential is taken along the path $\gamma : [0,1] \to S_1 \times \mathbb{R}^3$, here taken to be a straight line path based at $\mathbf{x}$, that is $\gamma(s) = (s\beta, \mathbf{x})$. In the Matsubara formalism, the inverse temperature, $\beta = 1/T$, is the extent of the compact direction and $(\tau, \mathbf{x})$ are global coordinates on $S_1 \times \mathbb{R}^3$ with a Euclidean line element. In the vacuum, this observable vanishes as a consequence of the action of the symmetry on $P(\mathbf{x})$, namely multiplication by the complex roots of unity, which cancel in the average. However, if the symmetry is broken, its vacuum expectation value is not constrained to vanish, as a good order parameter should behave.

By identifying the Polyakov loop with the static-quark creation operator, the expectation value of the trace of the Polyakov loop is related to the free energy of a static quark inserted into the vacuum, after renormalization [7]. Likewise, the Polyakov-loop correlator can be related to the free energy of the static quark-antiquark pair, projected into some colour representation.

From the cluster decomposition of the Polyakov loop correlator,

$$\langle \mathrm{Tr} P(\mathbf{x}) \mathrm{Tr} P^\dagger(\mathbf{0}) \rangle = e^{-\beta F_{\mathrm{Q}\bar{\mathrm{Q}}}(|\mathbf{x}|)} \overset{|\mathbf{x}|\to\infty}{\longrightarrow} |\langle \mathrm{Tr} P(\mathbf{x}) \rangle|^2, \tag{1.2}$$

$$\langle \mathrm{Tr} P(\mathbf{x}) \rangle = e^{-\beta F_{\mathrm{Q}\bar{\mathrm{Q}}}(\infty)/2}, \tag{1.3}$$

where $\langle \cdot \rangle$ denotes the expectation value of the observable in the thermal ensemble, it is clear that the confinement of quarks in the low-temperature phase results in an infinite static-quark free energy and the vanishing of the Polyakov loop[8]. Non-perturbative calculations of the colour-averaged free energy have been known to exhibit a form which invites the interpretation of a screened Cor-

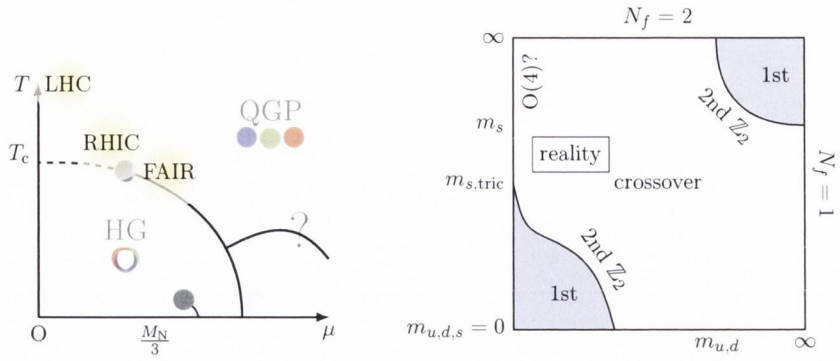

Figure 1.1: Schematic depictions of the phase diagram of QCD and the Columbia plot illustrating the order of the QCD phase transition, adapted from [11]. The question of the existence of the chiral critical end-point remains unanswered [12].

nell potential at high temperatures, so, just as for electrodynamic plasmas, the free movement of colour-electric charges results in screening phenomena. Various correlators of Polyakov loops have been defined in order to probe the interactions between heavy quarks, such as the manifestly non-gauge-invariant operator $\mathrm{Tr}\{P(\mathbf{x})P^\dagger(\mathbf{0})\}$, which couples to the free energy of two static quarks in a colour singlet [9].

However, the interpretation of these thermodynamic potentials, and especially employing them as potentials in models of heavy quarkonium is not satisfactorily understood [10].

The introduction of dynamical fermions breaks the centre symmetry explicitly at all temperatures, and the screening of the potential at large distances in the vacuum can be attributed to pair production or string breaking effects. The deconfinement phase transition becomes a smooth crossover in the presence of dynamical fermions, and the crossover temperature is no longer exactly coincident for every thermodynamic observable, but is usually defined from the peak of the Polyakov loop susceptibility, namely its first derivative with respect to temperature, see figure 3.1.

Closely linked with the deconfinement transition is the restoration of chiral symmetry which is spontaneously broken in the limit of vanishing quark masses at low temperatures by the chiral condensate, the order parameter for this symmetry. The Goldstone modes of the broken symmetry at low temperatures are the light pseudoscalar mesons. Furthermore, the axial $\mathrm{U_A}(1)$ symmetry is anomalous, broken by fluctuations of the topological charge, which results in the splitting of the η' meson from the rest of the pseudoscalar nonet. Just as for the deconfinement transition, chiral symmetry is only approximately realized in nature, broken

by the finite quark masses, so this transition is a smooth crossover.

The order of the transition and its dependence on the quark masses is summarized in the Columbia plot shown in figure 1.1. Empirically, the deconfinement and chiral phase transitions coincide in physical QCD and qualitative arguments based on constituent quark masses can provide some intuition for why this is the case [13]. Complementary to probing the chiral transition using with the properties of the light hadron spectrum [14], the deconfinement transition is naturally examined with heavy mesons, whose small size, it is posited, allow them to survive into the deconfined phase [15].

It is a great challenge to extend the knowledge of the phase structure to finite density, where numerical simulations, which have provided much of the quantitative data for QCD phase structure at zero chemical potential, fail due to the sign problem of the oscillating Gibbs factor. In addition to standard approaches such as reweighting of the Monte Carlo sum, dual representations or Taylor expansions, novel approaches based on the complexification of the field variables show promising avenues to begin to provide accurate predictions [16, 17]. Incidentally, analytic continuations of the path integral offer some hope to understand asymptotic series in quantum field theories [18].

1.2 Anatomy of a heavy-ion collision

As alluded to in the opening section, the only experimental access to probe QCD matter in exotic phases is through violent heavy-ion collisions whose products are short-lived. In this section, the evolution of the heavy-ion collision is surveyed in order to understand how to relate thermodynamic observables to the measurements of the particle yields and their momentum distributions. Modelling of the dynamic evolution of the fireball, the hot and dense volume whose characteristics depend on the centrality and centre-of-mass energy of the reactants, is required at all stages of the collision to connect these particle spectra with the thermodynamics of the hot matter. A collision proceeds in more or less four stages [19]. In the very early initial reaction hard partons are created in perturbative processes which become valuable probes of the hot medium which they traverse. Soft gluons in the initial state can possibly be treated in some classical approximation due to the saturation of these modes for energetic-enough collisions. The approach to thermalization and local equilibrium of the hot medium happens quickly and is modelled by some variant of kinetic theory. The expansion of this hot medium causes it to cool and eventually the quark and gluon degrees of freedom must bind to form hadrons, called chemical freeze-out which is treated in a statistical way.

Before chemical freeze-out occurs, hydrodynamics is the appropriate effective description for this strongly-coupled fluid. At this point the particle abundances are fixed as elastic scatterings dominate the cross-sections. Finally, kinetic freeze-out fixes the momentum distributions after the last scattering occurs.

One of the most important results of the RHIC experiment was the inference of the almost-ideal fluid nature of the QGP phase with a small viscosity to entropy density ratio manifested in the elliptic flow observable [20]. The implication of this measurement was that the fluid is in fact strongly-coupled and consequently the thermalization of the initial state happens on very short timescales. The applicability of a hydrodynamic description to the plasma also facilitates the connection between thermodynamic transport coefficients and experimental results. However, the strongly-coupled nature of the plasma, unlike familiar electromagnetic plasmas, immediately calls for the use of non-perturbative theoretical tools to investigate this phase of matter.

1.2.1 Approaches to strong-coupling

Gravity duals offer a framework to predict thermodynamic observables such as transport coefficients in a strongly-coupled conformal field theory. Since the viscosity to entropy density ratio was observed to be encouragingly close to the universal bound predicted from this framework [21, 22] it may be hoped that other observables in this approach are closely related to their counterparts in the real strongly-coupled plasma, such as the heavy-quark potential [23]. Ultimately, the uncontrolled nature of the approximation of working with only a QCD-like theory must be confronted, although the differing microscopic nature of the strongly-coupled theory is apparently less problematic in the deconfined phase [24].

Numerical lattice QCD is a systematically improvable non-perturbative framework which has been successful in elucidating the phase structure of QCD. For example, it has corroborated evidence of the strongly-coupled nature of the plasma through the observations of deviations from non-interacting limits in the equation of state [25]. However transport properties, being real-time phenomena, are challenging to extract from the Euclidean theory [26]. Nevertheless, lattice gauge theory calculations are beginning to make progress on numerous fronts relating to real-time observables, including, for example, data on the quenching parameter relevant to the fragmentation of hard partons into collimated jets of hadrons which is strongly affected by the presence of a hot medium [27, 28]. The lattice has also been successful in providing measurements which are suitable for diagnostics, in particular thermometers and baryometers, through fluctuations of conserved charges like electric, baryon and strangeness [29, 30]. These observ-

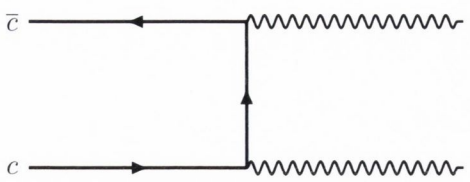

Figure 1.2: Lowest-order kinematically allowed process contributing to charm production from gluon radiation from initial reaction.

ables can be used to map out the freeze-out curve, the loci of the threshold for inelastic scattering in the phase diagram, of heavy-ion collisions [31].

The calibration of the temperature of the hot medium using heavy probes is another area to which the lattice can contribute [32]. The modification of the spectrum of heavy hadrons in a thermal medium has had a significant impact on the interpretation of the phase structure of QCD. These in-medium properties can be connected with the suppression of yields captured by nuclear modification factors or dilepton and photon production rates in heavy-ion phenomenology described below. In the following section, the motivation for using heavy quarkonium is outlined along with the desirable input from the lattice.

1.2.2 Heavy quarkonium probes

The prototypical thermometer of the quark-gluon plasma is the direct thermal photon, which, as a colour-blind probe, propagates through the plasma without interacting and allow inferences to be made about the hot medium formed in the early stages of the reaction. However, they are also produced copiously throughout the lifetime of the plasma, so the integrated history is required and the signal may be difficult to extract from a large background from non-direct decays.

The initial suggestion that quarkonia, in particular charmonium, are senstive probes of the medium goes back to the famous proposal of Matsui and Satz that the suppression of the yield of charmonium may be due to the presence of a deconfined medium [33]. Charm-anticharm pairs are created in initial hard processes of a reaction, e.g. from allowed processes such as in figure 1.2, which in the absence of any medium, may form a hidden-charmed bound state when the pair are relatively displaced on the order of the binding radius of that state, due to their large transverse momentum. However, in the presence of a deconfined medium, with effective screening of the binding potential from the thermal medium, the distance between the quarks may exceed this binding radius and the charm quarks may escape each other's attraction. Upon exiting the plasma

they hadronize with whatever is in their vicinity, most probably a light quark to form an open-charmed hadron, thereby the presence of the medium causes a suppression in the total yield of charmonium.

The criterion for the effective enough screening is when the temperature-dependent Debye screening length is smaller than, or comparable with, the binding radius. The argument follows analogously for radially and orbitally excited charmonium states, where the relevant binding radius is larger and hence the dissolution of these excitations occurs at lower temperatures [34]. This explanation of suppression was invoked to explain some tantalising results at the SPS experiment and courted controversy when other conventional suppression mechanisms were invoked to explain the observed suppression [35]. Cold nuclear matter effects in the initial and final state, such as nuclear absorption, exist even when a deconfined medium is not created [36]. Therefore, the term anomalous suppression is often applied to refer to the suppression caused by the hot medium effects. Careful disentangling of suppression mechanisms is necessary in order to infer the existence of a quark-gluon plasma from quarkonium yields.

Relevant differential observables such as the transverse-momentum and centrality dependence in the nuclear modification factor, which measures the ratio of the production cross-section in heavy-ion to hadronic collisions, normalized by the number of binary collisions, help differentiate between the suppression mechanisms [37]. As well as inelastic scattering which contributes to the suppression of charmonium yields, other processes are responsible for the *regeneration* of charmonium, including the statistical recombination of uncorrelated charm quarks in the medium. Such regeneration effects must also be included in the proper modelling of the production of charmonium in a hot medium and these counteract the suppression arising from the dissolution of direct charmonium. The inclusion of the contributions of feed-down from excited states is naturally important in these predictions due to the significant fraction of production due to radiative decays of higher states [38].

The suppression of bottomonium follows exactly the same argument of Matsui and Satz for charmonium. At the energies of the LHC it is produced copiously in heavy-ion collisions. It provides a more experimentally and theoretically clean probe due to a number of considerations. Cold nuclear matter effects are less important due to the smaller nuclear absorption cross section of the b-quark, so anomalous suppression is more easily distinguished [39]. The larger binding energies in the bottomonium system, and consequently smaller radii mean the bottomonium states are expected to survive well into the plasma. In addition, the regeneration effects are smaller than the charm case due to the reduced num-

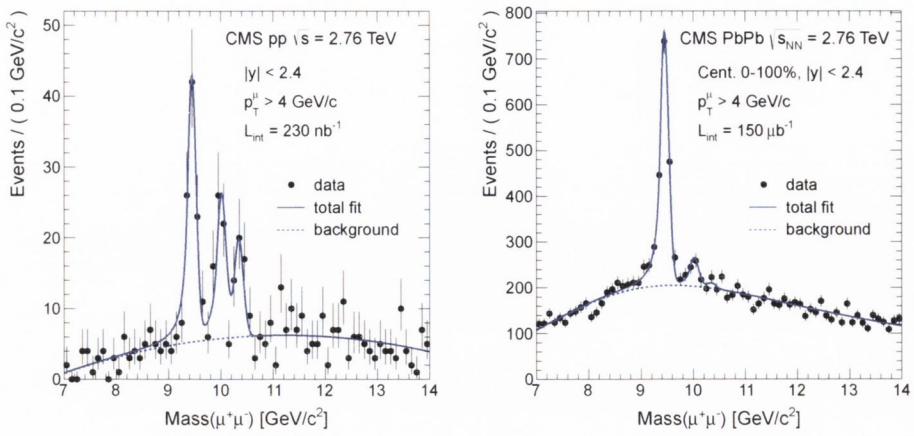

Figure 1.3: Dilepton invariant-mass spectra for hadronic (left) and heavy-ion (right) collisions from CMS [40] which illustrates the suppression of the excited states corresponding to the second and third peaks in the plasma phase.

bers of heavier quarks produced in the initial collision event due to their higher mass. The applicability of potential models and effective field theories which rely on separations of scales is more theoretically sound for the heavier bottom quark. Finally, whereas B-meson decays contribute to charmonium production, feed-down from open-heavy states is absent in bottomonium as feed-down can only occur from excited bottomonium states. The assumption of the lack of thermalization of the heavy-quark is more plausible for the heavier bottom quark as opposed to charm.

The sequential suppression of bottomonium states therefore provides an ideal diagnostic thermometer for the quark-gluon plasma. In addition to the complexity of modelling all of the aspects of the production, a detailed knowledge of the equilibrium in-medium properties of these states is required [41, 42]. This is the primary motivation for the study of the spectral functions of heavy-quarkonium states which control the abundances and reaction rates through the binding energies and widths, with non-perturbative tools such as lattice QCD.

The McLerran-Toimela formula connects the spectral function of thermalized heavy quarks in the vector channel with the dilepton and photon differential cross sections [43]:

$$\left.\frac{dN_{\ell_+\ell_-}}{d\omega\, d^3p}\right|_{\boldsymbol{p}=\boldsymbol{0}} \propto \alpha_{\mathrm{em}}^2 n_{\mathrm{B}}(\omega)\frac{\rho_{\mathrm{V}}(\omega)}{\omega^2} \tag{1.4}$$

$$\left.\omega\frac{dN_\gamma}{d^3p}\right|_{\omega=|\boldsymbol{p}|} \propto \alpha_{\mathrm{em}} n_{\mathrm{B}}(\omega)\rho_{\mathrm{V}}(\omega) \tag{1.5}$$

The thermalization of the heavy-quark, however, is neither valid for the bottom quark in the experimental context. The LHC's impressive mass resolution and high luminosity have allowed it to produce dilepton invariant-mass spectra, shown in figure 1.3, which directly illustrates the suppression of the excited bottomonium states in the heavy-ion collision versus the hadronic collision [40]. The PHENIX and STAR collaborations at RHIC have also recently reported suppression in the bottomonium Υ system [44, 45]. The spectral function in the vector channel is therefore a powerful observable, and the definitions in the following section relate it to the Euclidean and retarded propagators following the standard presentation [46, 47].

1.3 Spectral functions and Euclidean correlators

As well as being directly relevant through its connection to the dilepton and photon production rates, the spectral function is a valuable object to connect the real and imaginary-time correlation functions. In this section, the definition of the spectral function is introduced and related to the Euclidean correlators relevant to the lattice setting. The imaginary time, or Matsubara formalism is used to obtain the path-integral representation of the QCD canonical partition function, Z, through the Trotter formula,

$$Z \equiv \mathrm{Tr}_n(e^{-\beta H_{\mathrm{QCD}}}) \tag{1.6}$$

$$= \int_{\mathrm{per}.\beta} e^{-\int_0^\beta \mathrm{d}\tau \int \mathrm{d}^3\mathbf{x}\, \mathcal{L}_E[\bar{c},c,\bar{\psi},\psi,A_\mu]}, \tag{1.7}$$

where $\mathrm{Tr}_n(\cdot) = \sum_n \langle n| \cdot |n\rangle$ and $\{|n\rangle\}$ are the eigenstates of the Hamiltonian and $\mathcal{L}_e$ is the Euclidean Lagrangian density. The symbol $\int_{\mathrm{per}.\beta}$ indicates that the path integral is performed over fields in the action which are defined on Euclidean space with temporal extent equal to the inverse temperature, β, corresponding to the thermal compactification on $S_1 \times \mathbb{R}^3$. The appropriate boundary conditions are periodic ones for bosonic fields and antiperiodic ones for the fermionic fields owing to the cyclicity of the trace and anticommuting nature of the fermionic Grassmann fields, with ghosts obeying wrong statistics.

The Minkowskian and Euclidean coordinates are related by $t \to -i\tau$, so that integrals over the real temporal domain are Wick rotated in the complex plane. Due to the finite temporal extent and boundary conditions, the Euclidean frequencies appearing in Fourier representations are quantized *Matsubara frequencies*, $\omega_n = 2n\pi/\beta$ in the bosonic case, and the corresponding Fourier integrals are replaced with discrete sums, $\int \mathrm{d}k^0 \to 2\pi\beta^{-1}\sum_n$. The thermal averages of

composite operators, $\langle \mathcal{O}(\tau, \mathbf{x}) \rangle \equiv Z^{-1} \mathrm{Tr}_n(e^{-\beta H} \mathcal{O}(\tau, \mathbf{x}))$, can be expressed in the path integral representation

$$\langle \mathcal{O}(\tau, \mathbf{x}) \rangle = \int_{\mathrm{per.}\beta} \mathcal{O}(\tau, \mathbf{x}) e^{-\int_0^\beta \mathrm{d}\tau \int \mathrm{d}^3\mathbf{x}\, \mathcal{L}_E}. \tag{1.8}$$

In the following, spatial coordinates are omitted for clarity. The spectral function of a Hermitian bosonic composite operator, $\mathcal{O}(\tau)$, is defined as the difference between the Fourier transform of the forward and reverse two-point functions

$$\rho(k^0) \equiv \frac{1}{2\pi}(\tilde{D}^>(k^0) - \tilde{D}^<(k^0)), \tag{1.9}$$

$$\tilde{D}^>(k^0) \equiv \int_{-\infty}^{\infty} \mathrm{d}t\, e^{ik^0 t} \langle \mathcal{O}(t)\mathcal{O}(0) \rangle, \tag{1.10}$$

$$\tilde{D}^<(k^0) \equiv \int_{-\infty}^{\infty} \mathrm{d}t\, e^{ik^0 t} \langle \mathcal{O}(0)\mathcal{O}(t) \rangle, \tag{1.11}$$

where the insertion of a complete set of states gives the familiar spectral decomposition using the definition of the operators in the Heisenberg picture

$$\tilde{D}^>(k^0) = \sum_{n,m} \frac{e^{-\beta E_m}}{Z} \delta(k^0 + E_{nm}) |\langle n|\mathcal{O}(0)|m\rangle|^2, \tag{1.12}$$

$$\tilde{D}^<(k^0) = \sum_{n,m} \frac{e^{-\beta E_m}}{Z} \delta(k^0 - E_{nm}) |\langle n|\mathcal{O}(0)|m\rangle|^2, \tag{1.13}$$

where $E_{nm} = E_n - E_m$ is the difference between the n^{th} and m^{th} eigenenergies of the Hamiltonian. The relation between the spectral function and the retarded two-point function,

$$\tilde{D}_R(k^0) = i \int_{-\infty}^{\infty} \mathrm{d}t\, e^{ik^0 t} \langle \theta(t)[\mathcal{O}(t), \mathcal{O}(0)] \rangle, \tag{1.14}$$

can be made manifest by substituting the distributional representation of the θ-function

$$\theta(t) = i \int_{-\infty}^{\infty} \frac{\mathrm{d}k^0}{2\pi} \frac{e^{-ik^0 t}}{k^0 + i\epsilon}, \tag{1.15}$$

in eqn. (1.14) and using the definition of the spectral function, eqn. (1.11), to arrive at

$$\tilde{D}_R(k^0) = \int_{-\infty}^{\infty} \mathrm{d}k\, \frac{\rho(k)}{k - k^0 - i\varepsilon}, \tag{1.16}$$

which demonstrates the analyticity of the retarded propagator in the upper-half

plane. The Euclidean two-point function, $D_E(\tau) = \langle O(\tau)O(0)\rangle$, is related to the forward propagator through

$$D_E(\tau) = \int_{-\infty}^{\infty} \frac{\mathrm{d}k^0}{2\pi}\, e^{-k^0\tau}\tilde{D}^{>}(k^0). \tag{1.17}$$

Its Fourier transform, $\tilde{D}_E(\omega_n) = \int_0^\beta \mathrm{d}\tau\, e^{i\omega_n\tau} D_E(\tau)$, has a spectral representation obtained performing the τ-integral and using the definition of the spectral function to arrive at

$$\tilde{D}_E(\omega_n) = \int_{-\infty}^{\infty} \mathrm{d}k \frac{\rho(k)}{k - i\omega_n}. \tag{1.18}$$

In this way it is clear that the spectral function effectuates the connection between real and imaginary times and that the retarded propagator can be expressed as the analytic continuation of the Euclidean one

$$\tilde{D}_R(k^0) = \tilde{D}_E(-i(k^0 + i\varepsilon)). \tag{1.19}$$

Under the assumption of a real spectral function and employing the representation of the δ-function

$$\lim_{\varepsilon\to 0^+} \frac{1}{x + i\varepsilon} = \text{p.v.}\frac{1}{x} - i\pi\delta(x), \tag{1.20}$$

the spectral function is related to the imaginary part of the retarded two-point function or the cut discontinuity in the analytic continuation of the Euclidean two-point function

$$\rho(k^0) = \frac{1}{\pi}\Im\tilde{D}_R(k^0) \tag{1.21}$$

$$= \frac{1}{\pi i}(\tilde{D}_E(-ik^0 + i\varepsilon) - \tilde{D}_E(-ik^0 - i\varepsilon)). \tag{1.22}$$

The generalization of all of the above to the field theory setting is straightforward by taking the spatial degrees of freedom into account. When the spectral function is odd it is easy to verify using eqn. (1.17) a particularly useful mixed representation of the Euclidean correlator,

$$D_E(\tau, \mathbf{p}) = \int_{-\infty}^{\infty} \mathrm{d}\omega\, K(\omega,\tau)\rho(\omega,\mathbf{p}), \qquad K(\omega,\tau) = \frac{\cosh(\omega\tau - \beta\omega/2)}{\sinh(\beta\omega/2)}, \tag{1.23}$$

relevant to the correlation functions investigated in lattice studies which are even around the midpoint $\beta/2$. Alternative prescriptions to analytic continuation to

investigate real-time thermal field theory include the Schwinger-Keldesh contour or double-field theory [47].

1.3.1 Non-relativistic QCD

The motivation for using an effective field theory in non-perturbative simulations stems from the fact that the cutoff scale provided by the lattice spacing, a, is conveniently close to the heavy-quark mass scale, m_Q. While this fact precludes the use of a relativistic action on account of inducing large cutoff effects which scale generically as $\mathrm{O}(am_Q)$, it also enables the effective field theory approach to be applicable in capturing the relevant dynamics of the heavy-quarkonium system. In this section and the next the presentation of ref. [48] is followed.

An effective theory relies on a power-counting scheme to order the operators in the action [49]. The ordering of operators in *non-relativistic QCD (NRQCD)* is based on the small parameter $p/m_Q \sim v$, namely the heavy quark velocity in the quarkonium bound state. The binding energy in a colour-Coulombic picture, $m_Q\alpha_s^2 \sim m_Q v^2$, can be identified with the first radial splitting in quarkonium, $m_Q v^2 \approx 500$ MeV, so that the estimation $v^2 \approx 0.1$ holds for bottomonium and demonstrates the suitability of the non-relativistic treatment. Furthermore, it implies a separation of scales between the rest mass energy, the typical momentum transfer and the binding energy, $m_Q > m_Q v > m_Q v^2$. This suggests that to cutoff the theory at, or below, m_Q will provide a meaningful effective description where the rest mass scale plays no role.

The effective theory is defined by writing down an effective action with all possible operators up to a desired order in v which are consistent with the constraints of the symmetries to be imposed on the theory, such as gauge-invariance, rotational symmetry or discrete symmetries like parity and charge conjugation. This effective theory is non-renormalizable, that is the regularizer cannot be removed without the addition of ever higher-order improvement terms. The theory is therefore to be used to probe scales below the cutoff, which excludes the relativistic modes of the heavy quark. Matching of the effective theory onto QCD may be performed non-perturbatively, which has been achieved in rigorous but costly step-scaling studies, for instance in heavy-quark effective theory [50], or by matching lattice and experimental observables which reduces the predicitivity of the theory. . One may hope instead that as the cutoff scale is high, perturbative matching is adequate, however, convergence is only guaranteed asymptotically [51].

A Foldy-Wouthusyen-Tani (FWT) type transformation of the fields may be used to determine the operators to a given order in v and their tree-level coeffi-

cients [52]. Transformations of this type decouple the upper and lower components of the Dirac spinor, into two bi-spinor fields ψ, χ.

The contribution in v of the fields can be deduced as follows [48]. The quark number operator $\int \mathrm{d}^3x\, \psi^\dagger\psi$ ought to have expectation value unity in a heavy quarkonium state, thus $\psi \sim v^{3/2}$. Similarly, the expectation value of the kinetic energy operator is defined to be the kinetic energy, which gives the relation $\boldsymbol{D} \sim m_Q v$. The field equation (to lowest non-trivial order in v) for ψ is $(D_4 - \boldsymbol{D}^2/2m_Q)\psi = 0$, so that $D_4 \sim m_Q v^2$, and can also be used to trade time derivatives for spatial derivatives to simplify the integration provided only on-shell quantities are of interest. The order in v of the chromoelectric and chromomagnetic fields can be derived from the field equations for gauge potential, and give $g_0\boldsymbol{E} \sim m_Q^2 v^3$ and $g_0\boldsymbol{B} \sim m_Q^2 v^4$, respectively.

1.3.2 Improved non-relativistic action

The continuum NRQCD action for the heavy-quark field used in this work includes the following relativistic corrections and spin-dependent terms:

$$\mathcal{L}_0 = \psi^\dagger(x)\left[+D_\tau - \frac{\boldsymbol{D}^2}{2m_Q}\right. \tag{1.24}$$

$$- \frac{(\boldsymbol{D}^2)^2}{8m_Q^3} + \frac{ig_0}{8m_Q^2}(\boldsymbol{D}\cdot\boldsymbol{E} - \boldsymbol{E}\cdot\boldsymbol{D}) \tag{1.25}$$

$$\left. - \frac{g_0}{8m_Q^2}\boldsymbol{\sigma}\cdot(\boldsymbol{D}\times\boldsymbol{E} - \boldsymbol{E}\times\boldsymbol{D}) - \frac{g_0}{2m_Q}\boldsymbol{\sigma}\cdot\boldsymbol{B}\right]\psi(x). \tag{1.26}$$

The first line is the leading order term which gives the physics of the Schroedinger equation. The terms in second line give the relative v^2 corrections and include the leading correction to the kinetic energy, and the Darwin term, respectively. On the final line are the leading spin-dependent terms, and they are also suppressed by v^2 relative to the leading term. Experimentally, the hyperfine splittings, $\mathcal{O}(70\ \mathrm{MeV})$, are in accord with this suppression by v^2 relative to the radial splittings. To determine the hyperfine splittings to the 10% level one should include spin-dependent terms of the next order in v^2, which is not done here.

The coefficients in the action are the tree level values, and, rather than using the FWT transformation, can be determined by matching the leading order amplitude, for a quark scattering off a static chromoelectric field in Minkowski-space

QCD:

$$\begin{aligned}\mathcal{M}(\boldsymbol{p}_1,\boldsymbol{p}_2) = \bar{u}(\boldsymbol{p}_2)\gamma^0 g_0 A_\tau(\boldsymbol{p}_2-\boldsymbol{p}_1)u(\boldsymbol{p}_1) &\overset{p_1,p_2\ll m_Q}{\longrightarrow} \\ &\left[1-\frac{(\boldsymbol{p}_1-\boldsymbol{p}_2)^2}{8m_Q^2}\right]\psi^\dagger g_0 A_\tau(\boldsymbol{p}_2-\boldsymbol{p}_1)\psi \\ &+\frac{i}{4m_Q^2}\psi^\dagger\boldsymbol{\sigma}\cdot\boldsymbol{p}_2\times\boldsymbol{p}_1 g_0 A_\tau(\boldsymbol{p}_2-\boldsymbol{p}_1)\psi,\end{aligned} \tag{1.27}$$

to the (Minkowski-space) NRQCD action. The scalar part in the first line fixes the coupling of the Darwin term, while the vector part in the second line fixes the coupling of the spin-dependent chromoelectric term. The computation of the amplitude for a quark scattering off a static chromomagnetic field can be used to fix the coupling of the final term in a similar way.

1.3.3 Continuum spectral functions

The computation of the non-interacting Euclidean correlation functions in the pseudoscalar, vector, axial vector and scalar channels was performed in [53, 54] which is reviewed in this section. These will be compared with the high-temperature correlation functions on the lattice. That work demonstrated that the forward mixed-representation correlators of operators with point-splitting $\mathbf{x}$, satisfy a Schroedinger-like equation in the heavy-quark limit

$$\left(i\partial_t - 2m_Q - \frac{1}{m_Q}\frac{\partial^2}{\partial\mathbf{x}^2} + \ldots\right) D^>(t,\mathbf{0};\mathbf{x}) = 0, \tag{1.28}$$

where the ellipsis indicates the omission of terms at higher order in m_Q^{-1}. Upon removing the point-splitting, the mixed-representation Euclidean correlators in the vector and scalar channels are given explicitly

$$D_E^{\mathrm{S}}(\tau,\mathbf{q}) \propto \int \mathrm{d}^3\mathbf{p}\, e^{-(E(\mathbf{p})+E(\mathbf{p}+\mathbf{q}))\tau} \propto \frac{e^{-(2m_Q+\mathbf{q}^2/4m_Q)\tau}}{(m_Q\tau)^{3/2}}, \tag{1.29}$$

$$D_E^{\mathrm{P}}(\tau,\mathbf{q}) \propto \int \mathrm{d}^3\mathbf{p}\, \frac{\mathbf{p}^2}{m_Q^2} e^{-(E(\mathbf{p})+E(\mathbf{p}+\mathbf{q}))\tau} \propto \frac{e^{-(2m_Q+\mathbf{q}^2/4m_Q)\tau}}{(m_Q\tau)^{5/2}}, \tag{1.30}$$

where $E(\mathbf{p}) = m_Q + \mathbf{p}^2/2m_Q + \ldots$, from which the spectral functions, with $\mathbf{q} = 0$, can be calculated using eqn. (1.22) as

$$\rho(\omega) \propto \theta(\omega-2m_Q)m_Q^{2-\alpha}(\omega-2m_Q)^\alpha, \qquad \alpha = \begin{cases} 1/2 & \text{S wave} \\ 3/2 & \text{P wave} \end{cases} \tag{1.31}$$

Redefining the spectral function around the two-quark threshold, $\rho(\omega + 2m_Q) \to \rho(\omega)$, and dropping terms in the kernel, $K(\omega, \tau)$, which are exponentially suppressed in the heavy-quark limit, $m_Q \gg T$, the power-law decays of eqs. (1.29), (1.30) are obviously recovered

$$D_E(\tau) \propto \int_{-2m_Q}^{\infty} \mathrm{d}\omega\, e^{-\omega\tau} \rho(\omega) \propto \frac{1}{\tau^{\alpha+1}}, \tag{1.32}$$

However, it should be noted that such power-law decays only occurs when the threshold of the spectral function is at zero. Namely, if the threshold is shifted by redefining again $\rho(\omega) \to \rho(\omega + \omega_0)$, the decay is screened by an exponential term

$$D_E(\tau) \propto e^{-\omega_0\tau} \int_{-\omega_0}^{\infty} \mathrm{d}\omega\, e^{-\omega\tau} \rho(\omega) \propto \frac{e^{-\omega_0\tau}}{\tau^{\alpha+1}}. \tag{1.33}$$

This exponential decay will be relevant in the analysis of the correlation functions in chapter 3, due to the renormalization of the rest energy in NRQCD when interactions are turned on [55]. This analysis demonstrates that there must be a transition between exponential decay of the correlation functions in the vacuum where bound states exist to power-law decay at finite temperature. The computation of the free correlators is useful because the direct comparison of the Euclidean correlators obviates the need to perform any analytic continuation, which poses a significant challenge.

In addition to the tree-level result, the spectral functions were investigated in the resummed perturbative framework by identifying the potential, $V^{>}(t, |\mathbf{x}|)$, as the part scaling as m_Q^0 in the differential equation satisfied by the forward correlator. According to [56] this potential, derived in the static limit from the Wilson loop, contains a Debye-screened Coulomb part from the screening of colour-electric charges in the plasma. Furthermore, an imaginary part exists whose interpretation is due to the Landau damping of the binding gluons in the plasma, which leads to a decorrelation of the quarkonium state in the medium. The non-perturbative evaluation of this potential will be discussed in chapter 4.

1.3.4 Screening masses in NRQCD

In addition to the temporal correlations, spatial correlations can provide evidence for the in-medium modification of hadronic bound states [57]. For example, the mesonic screening mass for relativistic quarks is known to be $M_{\mathrm{scr}} = 2\sqrt{(\pi^2 T^2 + m_q^2)}$ [58], deduced from the spatial correlation which can be obtained

by

$$D_E(z) \propto \int_0^\infty \frac{\mathrm{d}\omega}{\omega} \int_{-\infty}^\infty \mathrm{d}p_z \, e^{ip_z z} \rho(\omega, (0,0,p_z)) \propto \frac{M_{\mathrm{scr}}}{\beta z} e^{-M_{\mathrm{scr}} z}. \tag{1.34}$$

In contrast, if a bound state exists at M with a corresponding peak in the spectral function $\rho(\omega) \propto \delta(\omega^2 - M^2)$, pure exponential decay will occur $D_E(z) \propto e^{-Mz}$. The appearance of the lowest Matsubara frequency, πT, is a consequence of the antiperiodic boundary conditions. If periodic boundary conditions in the temporal direction are imposed instead then the bound state screening mass is unchanged, however the screening mass in the free case is modified to be m_q. The divergence of the antiperiodic and periodic boundary condition screening mass correlators has been used as a diagnostic to indicate modification in the spectrum in charmonium [59].

In the heavy quark theory, the situation is different [60]. The dispersion relation for a non-relativistic hadronic bound-state is written $E_H(\mathbf{p}^2) = M_1 + \mathbf{p}^2/2M_2$, where the rest energy, M_1, and the kinetic mass, M_2, are distinct due to the possibility of transforming the rest mass in the quark dispersion relation arbitrarily. A bound state with corresponding spectral density $\delta(\omega - E_H(\mathbf{p}^2))$, has a mixed representation temporal correlator which decays as $e^{-E_H(\mathbf{p}^2)\tau}$. Substituting this mixed representation of the temporal correlator in the following definition of the screening correlator through the inverse transforms

$$D_E(z) = \int_0^\beta \mathrm{d}\tau \int_{-\infty}^\infty \frac{\mathrm{d}p_z}{2\pi} \, e^{ip_z z} G(\tau, (0,0,p_z)), \tag{1.35}$$

yields

$$D_E(z) \propto e^{-\sqrt{M_1 M_2} z} \left[3 - \mathrm{erf}\left(\sqrt{M_1 \beta} - \sqrt{\frac{M_2}{2\beta}} z \right) \right] \tag{1.36}$$

$$+ e^{\sqrt{M_1 M_2} z} \left[1 - \mathrm{erf}\left(\sqrt{M_1 \beta} + \sqrt{\frac{M_2}{2\beta}} z \right) \right] \tag{1.37}$$

In the infinite temporal extent limit, there is pure exponential decay with screening mass $\sqrt{M_1 M_2}$. In the non-interacting case, the correlators from eqn. (1.30)

are substituted into the expression eqn. (1.35) to arrive at

$$D_E^{\mathrm{S}}(z) = \int_0^\beta \mathrm{d}\tau \int_{-\infty}^{\infty} \frac{\mathrm{d}p_z}{2\pi} e^{ip_z z} \frac{e^{-E(\mathbf{p}^2)\tau}}{(m_Q\tau)^{3/2}} \tag{1.38}$$

$$\propto \int_0^\beta \mathrm{d}\tau \frac{e^{-m_Q z^2/\tau}}{m_Q\tau^2} \tag{1.39}$$

$$\propto \frac{e^{-m_Q z^2/\beta}}{(m_Q z)^2} \tag{1.40}$$

in the S wave channel, while the derivative coupling in the P wave channel modifies this to be

$$D_E^{\mathrm{P}}(z) = \int_0^\beta \mathrm{d}\tau \int_{-\infty}^{\infty} \frac{\mathrm{d}p_z}{2\pi} e^{ip_z z} \frac{e^{-E(\mathbf{p}^2)\tau}}{(m_Q\tau)^{5/2}} \tag{1.41}$$

$$\propto \int_0^\beta \mathrm{d}\tau \frac{e^{-m_Q z^2/\tau}}{m_Q^2\tau^3} \tag{1.42}$$

$$\propto \frac{e^{-m_Q z^2/\beta}}{(m_Q z)^4} \left(1 + \frac{m_Q z^2}{\beta}\right) \tag{1.43}$$

The infinite temporal extent limits of these non-interacting screening correlators are pure power-law decay, but at finite β, the large value of the prefactor in the exponent relevant to the parameters investigated in the lattice study will render the power law decay difficult to observe as it is screened by the exponential decay. In chapter 3 only the temporal correlations are investigated therefore and the continuum free correlation functions defined in the previous section and their lattice counterparts will be used to investigate the discretized version of NRQCD at finite temperature.

1.3.5 Analytical approaches

Heavy quarkonium has played a vital role in the understanding of the strong interaction much like the hydrogen atom in electrodynamics. Potential models are valuable tools to gain qualitative insights into the relevant physics at play and, given their success in describing the spectrum of quarkonium in the vacuum from early on [61], they have been used extensively to describe the temperature effects on the binding of heavy-quarks and the survival of heavy quarkonium in the deconfined phase [5]. Nevertheless, they require phenomenological modelling of the potential like the use of a screened Cornell potential, which has largely been disfavoured in preference for potentials derived from non-perturbative methods such as lattice QCD. The theoretical foundation for using popular thermodynamic potentials as model potentials at finite temperature is not clear and a variety of

approaches have been used which employed the colour-singlet free energy, internal energy or some combination thereof [62, 63]. Nevertheless, the use of potential models has been very instructive in elucidating the criteria for the unbinding of heavy quarks through the investigation of the in-medium quarkonium spectral functions by solving the Schroedinger equation with potentials [64, 65, 66].

Alternatively, effective field theory approaches have solid theoretical foundations at zero temperature [67]. These rely on integrating out either the hard scale, m_Q, resulting in NRQCD, see section 1.3.1, or the soft scale, $m_Q v$, called potential NRQCD. Long-distance effects can be incorporated by mapping onto potentials from non-critical strings [68]. The extension of these effective field theories to finite temperature has been an immensely successful programme [54, 53], which has allowed the determination of the quarkonium correlation function and spectral functions, see 1.3.3, in a weakly-coupled medium by employing the resummed perturbative potential [56]. The prediction of the imaginary part of the weak-coupling potential has been incorporated in potential models [69, 70, 71].

The complementary relationship between the heavy-quark potential and the quarkonium correlators through the effective field theory approach will be explored in the following chapters of this thesis. Ultimately comparing the effective field theory approach with non-perturbative data is valuable to understand the strongly-coupled nature of the deconfined medium. Although new methods on the market [72] may not suffer from the same issues in confronting real-time observables, the lattice is well-posed to contribute to this discussion. A compilation of the dissociation temperature for charmonium and bottomonium can be found in ref. [44] which demonstrates the competitive nature of predictions of binding in heavy quarkonium systems in the plasma from first principles of lattice QCD. In the following chapter the methodology for the non-perturbative evaluation of the quarkonium spectral functions from lattice QCD is outlined along with the strategies to extract the spectral function from Euclidean data and results for the zero-temperature spectral functions.

2 Lattice QCD

Lattice QCD is a powerful non-perturbative tool which remains the only systematically improvable and tractable non-perturbative regularization of the theory. The subject is now entering a high-precision era thanks both to Moore's law and algorithmic developments. Its success is not limited to the low-energy spectrum of QCD, but encompasses a wealth of static and real-time QCD phenomena and has elucidated important theoretical and phenomenological aspects of strongly-coupled field theories. Some basic facts of the lattice regularization are recalled in the first section following standard presentations [73] along with the discretized version of the effective theory used throughout this study at zero and finite temperature. The tuning of the heavy-quark mass and the study of the low-lying bottomonium spectrum at zero temperature is included, followed by a presentation of the strategies used to extract the spectral functions from the Euclidean lattice data which will be used in the final two chapters.

2.1 Light fermion and gauge action

Wilson's prescription [3] begins with the definition of the discrete lattice of finite extent $\Lambda = \{n = n_\mu \boldsymbol{e}_\mu \mid n_\mu = 1, \ldots, N_\mu\}$, where $\{\boldsymbol{e}_\mu\}_{\mu=1,\ldots,D}$ is the standard basis, and $|\Lambda| = \prod_{\mu=1,\ldots,D} N_\mu$. This replaces the D-dimensional spacetime of the Euclidean field theory on which the fields are defined. It is necessary to work with the Euclidean theory so that the Gibbs factor in the partition function is positive and can be interpreted as probability measure for the importance sampling for numerical Monte Carlo methods. In the simplest scenario where $N_\mu \equiv N$ the *aspect ratio* of Λ is unity. Then the first consequence of introducing the lattice formulation is the breaking of the group of isometries of Euclidean spacetime, $\mathrm{E}(D)$, to the cubic point group, $\mathrm{O_h}$.

QCD is an SU(3) gauge theory, with gauge fields which transform in the adjoint representation, and N_f fermions which transform in the fundamental rep-

resentation. The fermion field, $\hat{\psi}(n)$, with spinor and colour indices suppressed, and Hermitian gauge field $\hat{A}_\mu(n) = \hat{A}^a_\mu T^a$ are defined on Λ, where $\{T^a\}_{a=1,\ldots,8}$ are the generators of the algebra, with normalization $\mathrm{Tr}(T^a T^b) = \delta_{ab}/2$, defining the Killing form on the algebra. The discretization of the Dirac action follows immediately by replacing the fermion fields in the action with the dimensionless fields above, the spacetime integral with a finite sum and substituting the covariant derivative with a covariant finite difference operator:

$$\int \mathrm{d}^D x\, \bar{\psi}(x)(\not{D} + m_0)\psi(x) \quad \longrightarrow \quad \sum_{n\in\Lambda} \bar{\hat{\psi}}(n)(\hat{\not{D}} + \hat{m}_0)\hat{\psi}(n), \tag{2.1}$$

where $\not{x} = \gamma_\mu x_\mu$, and $\{\gamma_\mu\}$ satisfy $\{\gamma_\mu, \gamma_\nu\} = 2\delta_{\mu\nu}$. The Hermitian gauge-covariant finite-difference operator is defined through:

$$\hat{D}_\mu \hat{\psi}(n) = \frac{1}{2}\left(\hat{U}_\mu(n)\hat{\psi}(n + \boldsymbol{e}_\mu) - \hat{U}^\dagger_\mu(n - \boldsymbol{e}_\mu)\hat{\psi}(n - \boldsymbol{e}_\mu)\right), \tag{2.2}$$

where $\hat{U}_\mu(n) \equiv e^{ig_0 \hat{A}_\mu(n)}$ has the transformation $\hat{U}_\mu(n) \xrightarrow{g} g(n)\hat{U}_\mu g(n+\boldsymbol{e}_\mu)^\dagger$ under the action of the gauge group so that $\hat{D}_\mu\hat{\psi}(n) \xrightarrow{g} g(n)\hat{D}_\mu\hat{\psi}(n)$ is gauge covariant. This can be demonstrated using the corresponding continuum Wilson line, $U_\Gamma(n, n + \boldsymbol{e}_\mu) = \mathcal{P}e^{ig_0 \int_\Gamma dx_\mu \hat{A}_\mu(x)}$, where Γ is the shortest path connecting the neighbouring lattice sites. The group elements, $\{\hat{U}_\mu(n)\}$, are referred to as the *links* between neighbouring sites because of their relation to the parallel transporter of the continuum gauge connection. It also suggests that in the lattice formulation, the path integral measure over the gauge fields be replaced with that over the links.

According to the Feynman rules, the free momentum-space propagator can be written by inverting the quadratic part of the action

$$\frac{-i\hat{\not{k}} + \hat{m}_0}{\hat{k}^2 + \hat{m}_0^2}, \quad \hat{k}_\mu = \sin\hat{p}_\mu, \quad \hat{p}_\mu \in [-\pi, \pi). \tag{2.3}$$

For a discrete lattice the Brillouin zone is finite, and the lattice regularizes the field theory with a cutoff $\sim \pi$. Crucially, the high momentum modes with non-zero momentum components $\hat{p}_\mu = \pi$ contribute continuum-like fermionic excitations where $\hat{k} \to \hat{p}$, as well as the $\hat{p}^2 \approx 0$ mode. This spoils the interpretation of the action describing a single fermionic excitation. The Nielsen-Ninomiya no-go theorem [74] explains that it is impossible to construct a hermitian, local, massless Dirac operator, $\hat{D}$, with exact chiral symmetry $\{\hat{D}, \gamma_5\} = 0$, where $\gamma_5 = \prod_{\mu=1}^D \gamma_\mu$, without the presence of these extra excitations, or doublers. The simplest solution is to add a term to the action which explicitly breaks chiral

symmetry in the massless limit. Wilson proposed the action:

$$S_F = \sum_{n\in\Lambda} \hat{\bar{\psi}}(n)(\hat{\not{D}} + \hat{m}_0 - \frac{r}{2}\hat{\Box})\hat{\psi}(n) \tag{2.4}$$

$$\hat{\Box}\hat{\psi}(n) = \sum_{\mu=1}^{D}(\hat{U}_\mu(n)\hat{\psi}(n+\boldsymbol{e}_\mu) + \hat{U}_\mu^\dagger(n-\boldsymbol{e}_\mu)\hat{\psi}(n-\boldsymbol{e}_\mu) - 2\hat{\psi}(n)), \tag{2.5}$$

where $\hat{\Box}$ is the D-dimensional covariant lattice Laplacian and r is the Wilson parameter. The identification $\hat{U}_{\mu\nu}(n) \equiv \hat{U}_\mu(n)\hat{U}_\nu(n+\boldsymbol{e}_\mu)\hat{U}_\mu^\dagger(n+\boldsymbol{e}_\nu)\hat{U}_\nu^\dagger(n) \equiv e^{ig_0\hat{F}_{\mu\nu}(n)}$ is made, which is known as the elementary *plaquette* in the μ–ν plane based at n, and is related to the holonomy of the continuum gauge connection. The plaquette action of the discretized theory is arrived at by transcribing the continuum Euclidean gauge action using the plaquette fields:

$$\frac{1}{2}\int \mathrm{d}^D x\, \mathrm{Tr}(F_{\mu\nu}F_{\mu\nu}) \quad \longrightarrow \quad \frac{2}{g_0^2}\sum_{\substack{n\in\Lambda \\ \mu<\nu}}\left(3 - \frac{1}{2}\mathrm{Tr}(\hat{U}_{\mu\nu} + \hat{U}_{\mu\nu}^\dagger)\right). \tag{2.6}$$

By taking these steps the path integral is finite-dimensional and well defined. Periodic and anti-periodic boundary conditions are usually imposed for the gauge and fermion fields respectively, although results ought to be independent of this choice in the spatial directions for adequately large volumes. Open boundary conditions in the temporal direction allow the correct sampling of topological sectors at small lattice spacings which are traditionally difficult to explore with popular updating algorithms [75]. The quantum mechanical expectation value of an operator, some gauge-invariant monomials in the fields, denoted with angular brackets and defined through the path integral:

$$\langle \mathcal{O}[\hat{U}, \hat{\bar{\psi}}, \hat{\psi}]\rangle = Z^{-1}\int [\mathrm{d}\hat{U}\mathrm{d}\hat{\bar{\psi}}\mathrm{d}\hat{\psi}]\, \mathcal{O}[\hat{U}, \hat{\bar{\psi}}, \hat{\psi}]e^{-S_G - S_F}, \tag{2.7}$$

with Z such that $\langle 1\rangle = 1$. The path integral measure is the product of the Haar measure for each link and Grassmann measures for fermions

$$[\mathrm{d}\hat{U}\mathrm{d}\hat{\bar{\psi}}\mathrm{d}\hat{\psi}] = \prod_{n\in\Lambda}\prod_{\mu=1,\ldots,D}\mathrm{d}\hat{U}_\mu(n)\ \mathrm{d}\hat{\bar{\psi}}(n)\mathrm{d}\hat{\psi}(n). \tag{2.8}$$

The fermion action is quadratic in the fields, so the Grassmann integration can be evaluated by hand. Each flavour contributes a factor of $\det \hat{D}(\{\hat{U}\})$ to the path integral, which depends on the bare parameters for that flavour. Wick's theorem tells us to make all possible contractions of the fields, replacing them with the fermion propagators which depend on $\{\hat{U}\}$ e.g. $\hat{\psi}(n)\hat{\bar{\psi}}(m) \to \hat{D}^{-1}(n,m)$.

For meson correlation functions, the operator is a product of source and sink interpolators which are bilinears in the fields. As all of the spinor indices are contracted, it is always possible to rewrite the products of propagators resulting from the contractions as a product of traces over the Dirac indices. In flavour non-singlet channels, only one possible *connected* component where each edge in the graph corresponding to a contraction connects a field in the source and in the sink, whereas in flavour singlet channels edges of a graph may connect fields within the source and sink, corresponding to a *disconnected* graph.

The large dimension of the integral makes it impossible to make a direct numerical evaluation, even with a modest lattice size and coarse sampling of the integrand. Instead Markov Chain Monte Carlo methods are used to estimate the path integral stochastically. Given a Markov process which satisfies detailed balance and ergodicity, the sequence of gauge configurations generated $\{\{\hat{U}\}_i\}_{i=1,\ldots,N}$, asymptotically obeys the probability density $Z^{-1}(\det \hat{D})^{N_f} e^{-S_G}$ and expectation values can be estimated by the sample mean $\langle \mathcal{O} \rangle = \frac{1}{N} \sum_{i=1}^{N} \mathcal{O}[\{\hat{U}\}_i]$.

In particular, the Metropolis method satisfies that criteria exactly, and, for example, single-link updating can be used to propose a configuration $\{\hat{U}\} \to \{\hat{U}'\}$, which is accepted with probability $\min\{1, e^{-(S[\{\hat{U}'\}]-S[\{\hat{U}\}])}\}$. However, for non-local actions such as those for which the Grassmann fields have been integrated out, local updating schemes are inefficient. A modern approach to efficiently move through the field space is the hybrid Monte Carlo (HMC): consisting a hybrid molecular dynamics step and a final Metropolis acceptance step to make the algorithm exact. A set of Gaussian-distributed canonical momenta conjugate to the field coordinates are introduced, effectively bringing the fields in contact with a heat bath. Then the Hamiltonian evolution of the coordinates is performed, which is the microcanonical molecular dynamics trajectory. Finally a Metropolis step is performed so that detailed balance is preserved. This way the good ergodicity properties of the momenta updating can be combined with the efficient motion through configuration space of the molecular dynamics algorithm.

The fermionic determinants may be omitted altogether for convenience or cost resulting in a quenched, or partially quenched theory, which is not unitary. This is equivalent to neglecting vacuum polarization effects.

2.1.1 The continuum limit

The formulation of lattice field theory presented so far has been in terms of dimensionless variables. Observables measured from a lattice simulation are dimensionless numbers. By replacing the standard basis with a dimensionful coordinate system, $\boldsymbol{e}_\mu \to a_\mu \boldsymbol{e}_\mu$, without summation, a scale is reintroduced, the

lattice spacing a_μ, for now $a_\mu = a$. However, the lattice spacing does not appear explicitly in the dimensionless formulation, it is controlled by all of the couplings in the theory $\{g_0, \hat{m}_0, \ldots\}$. For a pure gauge theory there is only one coupling, the bare gauge coupling, g_0. The lattice spacing can only be measured by comparing a lattice observable, such as a hadronic mass, the Sommer parameter r_0, or the Wilson flow scale t_0, with an experimental value, or value determined from another lattice simulation.

Any dimensionful quantities may be expressed as

$$\mathcal{O}(a, g_0, \hat{m}_0, \ldots) = a^{-d}\hat{\mathcal{O}}(g_0, \hat{m}_0, \ldots), \tag{2.9}$$

where d is the observable's canonical mass dimension. In particular, the dimensionless mass $\hat{M}$ must vanish in the continuum limit for the value in physical units to be finite. The vacuum to vacuum amplitude, Z, is closely related to the partition function for a statistical mechanics system via the path integral representation. The dimensionless correlation length $\hat{\xi}$, in such a system, must diverge as the critical point is approached in the space of couplings, which leads to universality of critical phenomena, or independence from the physics on the ultraviolet scale [76]. The correlation length is inversely related to the mass of the lowest mass in the spectrum, namely the pions in a theory with fermions, or the lightest glueball in a pure gauge theory. This suggests that the continuum limit of the lattice field theory is realized at the critical point, where correlation lengths become large relative to the lattice spacing. However, due to the finite extent of the lattice, which provides an infrared cutoff, these correlation lengths ought not to exceed the extent of the lattice. Lüscher's argument [77] for exponential finite volume corrections leads to the criterion $M_\pi \times aN \gtrsim 4$ as satisfactory suppression of finite volume effects. These criteria give rise to the scaling window, where a balance between a fine, small lattice and large, coarse lattice is sought.

The dependence of the lattice spacing on the bare couplings of the theory is described by the renormalization group beta function $\beta = -\partial g_0/\partial(\ln a)$. The first coefficients in the expansion of the β function are independent of the renormalization scheme, so the β function is universal in the perturbative regime and can be integrated to give

$$a = \Lambda_L^{-1}(\beta_0 g_0^2)^{-\beta_1/2\beta_0^2} e^{-1/2\beta_0 g_0^2}, \tag{2.10}$$

which demonstrates that the critical coupling is $g_0^\star = 0$ and defines the requisite scaling behaviour for any lattice observable $\hat{\mathcal{O}} \propto a^d$ which must be observed for the correct continuum limit to be approached. The vanishing of the critical

coupling is due to asymptotic freedom, as the bare coupling, which is relevant to the cutoff scale, becomes small as the cutoff is removed. The appearance of a dimensionful scale in a theory with only dimensionless parameters is called dimensional transmutation, like in the static limit of QCD due to the anomalous conformal symmetry.

2.1.2 Symanzik improvement

Although the scaling criterion enables a well-defined continuum limit to be taken, due to critical slowing [78] of simulation algorithms as the critical point is approached it may not be practically possible to reach the regime of adequately small lattice spacings. Therefore, one would like to reduce the discretization and cutoff errors at finite a so that reliable continuum physics can be extracted at larger lattice spacings. Symanzik's procedure [79] is to define a continuum local effective action which includes all irrelevant operators with the required symmetries of the lattice theory:

$$S_{\text{eff}} = \int \mathrm{d}^D x \, \left(\mathcal{L}_0 + a\mathcal{L}_1 + a^2 \mathcal{L}_2 + \ldots \right), \quad \text{with} \quad \mathcal{L}_k = \sum_{\{\mathcal{O}\}} c_{\mathcal{O}}^{[k]} \mathcal{O}^{[k]}. \tag{2.11}$$

The inclusion of these irrelevant operators, which do not alter the critical behaviour of theory, can be used to drive it to a critical surface, or renormalized trajectory, which is free of discretization effects even for finite a. However, in practice the mass dimension of the operators is used to truncate the series at a finite order. $\mathrm{O}(a^k)$ improvement of the hadronic spectrum can be achieved through the discretization of this action by including operators with mass dimension up to $D + k$ [80]with appropriately chosen improvement coefficients. The improvement of on-shell matrix elements further requires the addition of higher-order local counterterms and the tuning of their coefficients. The matching of the couplings in the effective theory to QCD is often performed perturbatively, which is valid for small enough lattice spacings due to asymptotic freedom. The non-renormalizability of the improved theory is not pathological in the continuum limit because the improvement condition requires that the higher dimensional operators vanish in that limit. This is in contrast to the situation in a non-renormalizable effective field theory, where ever higher dimensional operators must be included as the cutoff is removed.

The plaquette gauge action is already $\mathrm{O}(a)$-improved because no five dimensional operators with the relevant symmetries exist. The next operators occur at dimension six, corresponding to the six-link Wilson loops, and can be included to make the action $\mathrm{O}(a^2)$ improved. An important observation is that fermion

actions whose Dirac operators obey the Ginsparg-Wilson relation $\{\hat{D}, \gamma_5\} \propto a$, are automatically O($a$)-improved. The Wilson fermion action is not chirally invariant and improvement is necessary to eliminate O(a) cutoff effects. There is only one non-redundant five dimensional operator required, the *clover* term, $\frac{c_{\rm SW}}{2} \sum_{\mu<\nu} \bar{\hat{\psi}} \sigma_{\mu\nu} \hat{F}_{\mu\nu} \hat{\psi}$, where $\sigma_{\mu\nu} = -i\gamma_{[\mu}\gamma_{\nu]}$ and the usual choice of the field strength tensor is the clover-leaf definition:

$$\hat{F}_{\mu\nu} = \frac{1}{4i}\hat{Q}_{[\mu\nu]}, \quad \text{where} \quad \hat{Q}_{\mu\nu} = \hat{U}_{\mu\nu} + \hat{U}_{\nu,-\mu} + \hat{U}_{-\mu,-\nu} + \hat{U}_{-\nu,\mu}, \tag{2.12}$$

where all plaquettes are based at the same site, and define the corresponding fields at that site.

Finally, tadpole improvement [81] is often implemented to improve the convergence of lattice perturbation theory and reduce large renormalizations resulting from the ultraviolet properties of certain tadpole diagrams. These effects are empirically known to be as large as the tree-level contributions [82]. Practically, it can be achieved by replacing links with $\hat{U}_\mu \to \hat{U}_\mu / u_0$ where u_0 is a suitable gauge-invariant definition of the average link. Since u_0 is a global factor, the couplings may be redefined to implement this improvement, for example in the hopping-parameter form of the action:

$$u_0 = \left(\frac{1}{3}\langle \mathrm{Tr}\hat{U}_{\mu\nu}\rangle\right)^{1/4}, \quad \kappa \to \frac{\kappa'}{u_0}, \quad c_{\rm SW} \to \frac{c'_{\rm SW}}{u_0^3}, \quad g_0^2 \to \hat{g}_0^2 u_0^4. \tag{2.13}$$

One can imagine tadpole improvement as the factorization of contributions from contracted gauge fields in a loop integral which suppresses factors of the lattice spacing in the expansion of the link, $U_\mu = u_0(1 + a g_0 \hat{A}_\mu^{\rm IR} + \ldots)$, thereby leaving only the relevant degrees of freedom.

2.1.3 Anisotropic lattices

Certain applications in lattice QCD require a fine resolution in the temporal direction, while perhaps also requiring that finite-size effects are minimized by having a large physical spatial volume. In order to satisfy these requirements simultaneously it may be advantageous to use a lattice action with different discretizations in the time and space directions, resulting in anisotropic lattice spacings [83], $a_i \equiv a_s$ and $a_4 \equiv a_\tau$, with the renormalized anisotropy $\xi = a_s/a_\tau$, usually greater than unity. These anisotropic lattices can be used to reduce the cost of simulations where finite-a_s errors are believed to be under control.

For example, a fine resolution of the temporal correlators is necessary to extract the excited-state spectra of hadrons [84], where the signal degenerates

rapidly in time. Heavy states, such as in the heavy quarkonium spectra suffer from the same problem [85]. Anisotropic fermion discretizations have been formulated which have leading cutoff effects at $\mathcal{O}(m_Q a_\tau)$ which take advantage of a finer temporal lattice spacing [86]. The glueball spectrum has also been investigated [87] using anisotropic lattices, due to the notoriously poor signal of the pure gauge operators used in that calculation. Anisotropic lattices are also useful in the study of finite-temperature lattice gauge theory where the physical temporal extent must be varied, either by a fixed-scale or fixed-N_τ approach. The evaluation of lattice spectral functions desperately requires precise and high-resolution temporal correlator data, which for small physical temporal extents really requires a highly anisotropic lattice.

The ensembles used in the following studies were generated with an anisotropic Symanzik-improved gauge action and an anisotropic clover Wilson action, including tadpole improvement. The improvement coefficients are the tree-level values. The gauge action is:

$$S_G^\xi[\hat{U}] = \frac{2}{g_0^2}\sum_{n\in\Lambda}\left[\sum_{\substack{\mu\neq\nu\\ i,j}}\Re\mathrm{Tr}(1-\hat{U}_{\mu\nu})\left(\frac{5}{6u_s^4\xi_g^0}\delta_{\mu i}\delta_{\nu j}+\frac{4\xi_g^0}{9u_s^2u_\tau^2}\delta_{\mu i}\delta_{\nu 4}\right)\right. \tag{2.14}$$

$$\left.-\sum_{\substack{\mu\neq\nu\\ i,j}}\Re\mathrm{Tr}(1-\hat{R}_{\mu\nu})\left(\frac{1}{12u_s^6\xi_g^0}\delta_{\mu i}\delta_{\nu j}+\frac{\xi_g^0}{36u_s^4u_\tau^2}\delta_{\mu i}\delta_{\nu 4}\right)\right], \tag{2.15}$$

where $\hat{R}_{\mu\nu}$ is the 2×1 Wilson loop in the μ–ν plane, and ξ_g^0 is the bare gauge anisotropy. This action has $\mathcal{O}(a_s^4, a_t^2, g_0^2 a_s^2)$ discretization errors. The 2×1 rectangle in the 4–i plane is not included because it violates reflection positivity needed to construct a positive definite transfer matrix. The fermion action is:

$$S_F^\xi[\hat{U},\bar{\hat{\psi}},\hat{\psi}] = \sum_{n\in\Lambda}\bar{\hat{\psi}}(n)\frac{1}{u_\tau}\left[u_\tau\hat{m}_0+\hat{W}_4+\frac{1}{\xi_f^0}\sum_i\hat{W}_i+\frac{1}{2}\sum_{\substack{\mu>\nu\\ i}}\sigma_{\mu\nu}\hat{F}_{\mu\nu}\left(c_s\delta_{\mu i}+\frac{c_\tau}{3}\delta_{\mu 4}\right)\right]\hat{\psi}(n), \tag{2.16}$$

where $\hat{W}_\mu$ is the Wilson fermion matrix constructed above, and ξ_f^0 is the bare

	N_f	a_s (fm)	a_τ^{-1} (GeV)	ξ	M_π/M_ρ	$a_s m_Q$	$\mathcal{E}$ (MeV)
First gen.	2	0.162	7.35	6	0.54	4.5	8570
Second gen.	$2+1$	0.1227(8)	5.63(4)	3.5	0.45	2.92	8252(9)

Table 2.1: Comparison between lattice parameters used in earlier work [91, 92, 93, 94, 95, 96] (first generation) and this work (second generation). $\mathcal{E}$ is the difference between the experimental and NRQCD Υ used to remove the energy shift of the spectrum.

fermion anisotropy. The tree-level, tadpole-improved clover coefficients are:

$$c_s = \frac{1}{\xi_f^0 u_s^3}, \quad c_\tau = \frac{1}{2u_\tau u_s^2}\left(\frac{\xi_g^0}{\xi_f^0} + \frac{1}{\xi}\right), \tag{2.17}$$

and ξ is the renormalized anisotropy. Finally, this action also includes three-dimensional stout smearing of the links [88]. Smearing of the gauge fields in the action reduces the coupling to the high-momentum modes and suppresses lattice artifacts. Stout smearing's analytic projection back into the gauge group means it is suitable for use in HMC algorithms in the calculation of the force in the molecular dynamics routine. The mean links for tadpole improvement are thus defined from the stout, rather than thin, links in the fermion action. The ensemble was generated with $N_f = 2 + 1$ using the Rational HMC, which is suitable for odd numbers of flavours [89], which uses a rational approximation to the fermion determinant. The fermionic determinant is usually implemented via the pseudofermion method which is only suitable for even numbers of degenerate quarks.

The inequality of the spatial and temporal lattice spacings ought to be irrelevant in the continuum limit, which is independent of the details of the discretization. Intuitively, as much of the symmetry of the continuum theory shoud be restored as possible at finite lattice spacing, so that the correct continuum theory is approached as the cutoff is removed. For an anisotropic action, this amounts to tuning the bare anisotropies in each sector (gauge, light quark, heavy quark, etc.) so that the renormalized anisotropies are consistent, in the hope that the Lorentz symmetry of the continuum theory is being restored. The tuning of the gauge anisotropy in the ensembles used in these works was performed using Klassen's method [90], or the sideways potential. The fermion anisotropy is tuned through the pseudoscalar meson dispersion relation, $E^2(\boldsymbol{P}^2) = M_{\mathrm{PS}}^2 + \boldsymbol{P}^2/\xi_f^2$. The parameters of the zero-temperature and finite-temperature ensembles used in this work are listed in table 2.1.

2.1.4 Lattice NRQCD

Due to the discretization effects entering relativistic actions generically as $a_s m_Q$ it is not possible to simulate quarks with masses approaching the lattice cutoff without introducing significant lattice artifacts. Naturally, an ultraviolet cutoff on the order of the desired heavy quark mass suggests the use an effective field theory approach motivated in the introduction. Remarkably, this ancient strategy [97, 55] is still relevant today and used to simulate heavy quarks on the lattice in state-of-the-art dynamical simulations of quarkonium and other b-physics observables [98, 99], and has consequently been tested stringently.

The transcription of continuum NRQCD into the lattice theory [48] is straightforward by substitution of continuum spatial covariant derivatives with the symmetric covariant finite differences, $\boldsymbol{\nabla}^{\pm}$, and the temporal covariant derivative with a non-symmetric temporal covariant finite difference, ∇_τ^+. With this formulation the quark propagator can be integrated with an explicit integration scheme. The clover definition of the field strength tensor is used to define the lattice chromoelectric and chromomagnetic fields as usual. Due to the decoupling of the heavy quark and antiquark and the first order nature of the equations of motion the quark action is written suggestively in terms of the leading order Hamilton and its corrections which are the corrections outlined in section 1.3.2:

$$S_\psi = a_s^3 a_\tau \sum_{n\in\Lambda} \psi^\dagger(n) \left[\nabla_\tau^+ + H_0 + \delta H\right] \psi(n) \tag{2.18}$$

$$\equiv a_s^3 \sum_{n\in\Lambda} \psi^\dagger(n) \left[\psi(n) - K_\tau \psi(n - a_\tau \boldsymbol{e}_\tau)\right] \tag{2.19}$$

which is recast in terms of the integration kernel defined through:

$$K_{\tau+1} = \left(1 - \frac{a_\tau H_0}{2k}\right)^k U_\tau^\dagger(n) \left(1 - \frac{a_\tau H_0}{2k}\right)^k (1 - a_\tau \delta H)\,, \tag{2.20}$$

$$\delta H \to \delta H + \frac{a_s^2 \Delta^{(4)}}{24 m_Q} - \frac{a_\tau (\Delta^{(2)})^2}{16 k m_Q^2}, \qquad \text{where,} \qquad \Delta^{(2n)} = \sum_i (\nabla_i^+ \nabla_i^-)^n. \tag{2.21}$$

The $2n^{\text{th}}$-order derivatives are defined in terms of the components of the symmetric second order one. In addition to the relativistic corrections, the lattice improvement terms in the final line eliminate the next-to-leading order corrections in a_s^2 and the next-to-leading order corrections in a_τ in the evolution equation from the leading order Hamiltonian. The anisotropic action is obtained by keeping track of the temporal lattice spacing in the dimensionless action as usual.

The quark propagator is obtained from the equations of motion, which are simply read off from eq. 2.19. It is the solution of an initial value problem, which, in the discrete formulation is integrated exactly as follows:

$$G(\boldsymbol{n}, n_\tau) = K_\tau G(\boldsymbol{n}, n_\tau - a_\tau \boldsymbol{e}_\tau), \tag{2.22}$$

The antiquark propagator is obtained by using the charge conjugation symmetry, which results in it being simply related to the quark propagator through complex conjugation. Lepage's parameter, k, is introduced to stabilize the integration so that $|1 - a_\tau H_0/2k| < 2$. This instability can be ascertained from the free quark propagator for the simplest NRQCD action with only the H_0 term, and leads to the condition $\hat{m}_Q \gtrsim 3/\xi k$ [100]. In this study, the choice $k = 1, \ldots, 3$ have been investigated and $k = 1$ is satisfactory as demonstrated in the investigation of the spectrum presented in the following section. Tadpole improvement is implemented by dividing the links by the mean link as usual.

2.2 Bottomonium spectroscopy

In this section, an unsophisticated study of the low-lying bottomonium spectrum is presented, principally to tune the heavy-quark mass, $a_s m_Q$, and to verify the adequacy of the lattice set-up in obtaining the gross features of the bottomonium spectrum. Furthermore, it provides a test-bed for the reconstruction of the spectral functions, whose structure in the vacuum is known unambiguously from the spectrum. The HPQCD collaboration [98, 99] has investigated the bottomonium spectrum including higher-lying orbital and radial excitations than are included here. They have accounted for discretization effects, computed radiative corrections to the matching coefficients and estimated the omission of higher-order relativistic corrections and have demonstrated excellent agreement with the experimental spectrum of gold-plated bottomonium states [101].

2.2.1 Operators and correlation functions

The extra continuum symmetries of the lowest order effective action suggests the states be labelled by the unitary representations of spin, orbital and total angular momentum, and likewise the well-defined interpolating operators which overlap with them. While total spin remains a good quantum number for the continuum theory, orbital and spin angular momentum are just approximate categorizations of the states as these operators do not commute with the full Hamiltonian. For instance, S wave and D wave states in the vector channel may indeed mix, although

J	Λ
0	A_1
1	T_1
2	$T_2 \oplus E$
3	$A_2 \oplus T_1 \oplus T_2$

Table 2.2: Subduction of the continuum irreducible representations of the rotation group with dimension $\dim_J = 2J + 1$ into the irreducible representations of the cubic point group, with dimesions $\dim_{A_1,A_2} = 1$, $\dim_E = 2$ and $\dim_{T_1,T_2} = 3$.

J^{PC}	$^{2S+1}L_J$	Λ^{PC}	$\Gamma(\mathbf{x}, \mathbf{x}')$	
0^{-+}	$^1S_1$	A_1^{-+}	$\mathbb{I}$	
1^{--}	$^3S_1$	T_1^{--}	σ_i	
1^{-+}	$^1P_1$	T_2^{-+}	Δ_i	
0^{++}	$^3P_0$	A_1^{++}	$\sum_j \Delta_j \sigma_j$	
1^{++}	$^3P_1$	T_1^{++}	$\Delta_{[j}\sigma_{k]}$	$i \neq j \neq k$
2^{++}	$^3P_2$	E^{++}	$\Delta_j\sigma_j - \Delta_k\sigma_k$	$i \neq j \neq k$
		T_2^{++}	$\Delta_{\{j}\sigma_{k\}}$	$i \neq j \neq k$
2^{--}	$^3D_2$	E^{--}	$\Delta_i\Delta_{[j}\sigma_{k]}$	$i \neq j \neq k$

Table 2.3: The selection of (non-exotic) channels investigated in this work. There is no ambiguity in identifying the spin of the ground state in any of these channels. The multiplets of the $L \neq 0$ states use the symmetric finite difference operator $\Delta_i(\mathbf{x}', \mathbf{x}) \propto \delta_{\mathbf{x}',\mathbf{x}+\hat{\imath}} - \delta_{\mathbf{x}',\mathbf{x}-\hat{\imath}}$. The average is always taken over components of the same spin. Local sources, $\phi(|\mathbf{x}|) = \delta_{\mathbf{x},\mathbf{0}}$, and Gaussian smeared sources with $\phi(|\mathbf{x}|) = \exp(-\mathbf{x}^2/2\rho^2)$ were used.

the identification of the lowest lying state poses no ambiguity.

However, continuous spacetime symmetries are reduced upon discretization on a finite lattice. The subduction of the continuum irreducible representations to the lattice ones results in ambiguities in the identification of the continuum spin, J, of the spectrum. Table 2.2 records the correspondence of the continuum and lattice representations. The quark model or Regge trajectories suggest the identification of the lowest energy states in each channel with the state with lowest continuum spin appearing in that channel. In principle, examining the degeneracies between the lattice irreducible representations in the continuum limit offers a solution, but practically it is impossible for higher excited states when the signal becomes poor and where physical degeneracies also exist. Alternatively, construction of operators which are subduced from operators with a definite continuum spin have been shown to indicate the spin of excited states on the lattice through the relative magnitude of the overlaps, as long as one is close enough to the continuum [102]. In this work, only states with spins up to $J = 2$ are

investigated so no such difficulty arises. For bottomonium, states with spins up to $J = 4$ have been investigated in ref. [103], however, the highly divergent correlation functions are strongly afflicted by lattice artifacts.

The NRQCD interpolating operators are bilinears in the two-component Pauli fields, which generally have some spatial structure due to the derivative couplings necessary to project onto a state with non-zero orbital angular momentum

$$\mathcal{O}(\tau, \mathbf{x}) = \psi^\dagger(\tau, \mathbf{x}) \sum_{\mathbf{y}} \Gamma(\mathbf{x}, \mathbf{y}) \psi(\tau, \mathbf{y}), \tag{2.23}$$

where spin and colour indices are suppressed. The spatial derivatives and spin structure used to construct the operators are listed in table 2.3. The non-covariant spatial structure requires the gauge to be fixed. Recently, covariantly-smeared operators have been investigated and reported to provide good signals [104].

The overlap of these *local* operators with the ground state in a given channel may be improved upon by introducing a physical *smearing*, which is a convolution of one of the fields in the interpolating operator with a radially symmetric wavefunction, $\psi(\tau, \mathbf{x}) \to \sum_{\mathbf{y}} \phi(|\mathbf{x} - \mathbf{y}|)\psi(\tau, \mathbf{y})$ motivated by physical intuition. The smearing function has support at a single Euclidean time and in the following illustration is introduced both for the source and sink operator in the hadronic correlation function. Hydrogenic wavefunctions have been used [97], but only local sources and Gaussian wavefunctions are employed in this work. Due to the augmented spatial structure when smearing is performed, the fields in the interpolating operator are contracted with the following coupling

$$\tilde{\Gamma}(\mathbf{x}, \mathbf{y}) = \sum_{\mathbf{x}'} \Gamma(\mathbf{x}, \mathbf{x}') \phi(|\mathbf{x}' - \mathbf{y}|). \tag{2.24}$$

Due to translation invariance, the mixed representation Euclidean correlation function may be written

$$G_E(\tau, \mathbf{p}) = \left\langle \sum_{\mathbf{x}} e^{-i\mathbf{p}\cdot\mathbf{x}} \mathcal{O}^\dagger(\tau, \mathbf{x}) \mathcal{O}(0, \mathbf{0}) \right\rangle \tag{2.25}$$

$$\propto \left\langle \sum_{\mathbf{x},\mathbf{y}} e^{-i\mathbf{p}\cdot(\mathbf{x}-\mathbf{y})} \mathcal{O}^\dagger(\tau, \mathbf{x}) \mathcal{O}(0, \mathbf{y}) \right\rangle. \tag{2.26}$$

Applying Wick's theorem to the path integral, the contracted quark fields are replaced by the inverse fermion matrix, $D^{-1}_{\mathbf{xy}}(\sigma; \tau)$, so the translationally-invariant

Euclidean hadronic correlation function becomes

$$G_E(\tau, \mathbf{p}) \propto \left\langle \mathrm{Tr} \sum_{\mathbf{x},\mathbf{y}} e^{-i\mathbf{p}\cdot(\mathbf{x}-\mathbf{y})} \sum_{\mathbf{x}',\mathbf{y}'} \tilde{\Gamma}(\mathbf{y},\mathbf{y}') D^{-1\dagger}_{\mathbf{y}'\mathbf{x}'}(\tau;0) \tilde{\Gamma}(\mathbf{x},\mathbf{x}') D^{-1}_{\mathbf{x}\mathbf{y}}(\tau;0) \right\rangle , \tag{2.27}$$

where the trace is performed over the product of matrices by contracting the suppressed colour and spin indices in the obvious way. The decoupling of the heavy quarks and antiquarks in the effective action mean there is no disconnected contribution, as the quark and antiquark fields can be labelled as different flavours.

Given the solution vector, $G^{\sigma}_{\mathbf{y}}(\tau)$, to the inversion of the fermion matrix on a stochastic source with zero mean and finite variance, $\eta_{\mathbf{x}}$,

$$D_{\mathbf{x}\mathbf{y}}(\sigma+\tau;\sigma) G^{\sigma}_{\mathbf{y}}(\tau) = \eta_{\mathbf{x}} e^{i\mathbf{p}\cdot\mathbf{x}} \delta_{\tau,0}, \tag{2.28}$$

$$D_{\mathbf{x}\mathbf{y}}(\sigma+\tau;\sigma) \tilde{G}^{\sigma}_{\mathbf{y}}(\tau) = \sum_{\mathbf{x}'} \eta_{\mathbf{x}'} \tilde{\Gamma}(\mathbf{x},\mathbf{x}') \delta_{\tau,0}, \tag{2.29}$$

it is straightforward to verify that the estimator

$$\mathrm{Tr} \sum_{\mathbf{x}} e^{-i\mathbf{p}\cdot\mathbf{x}} \sum_{\mathbf{x}',\sigma} \tilde{\Gamma}(\mathbf{x}',\mathbf{x}) G^{\dagger,\sigma}_{\mathbf{x}'}(\tau) G^{\sigma}_{\mathbf{x}}(\tau), \tag{2.30}$$

has the expected value of the correlation function in eqn. (2.27) using the uncorrelated noise property $\mathbb{E}_{\eta}[\eta_{\mathbf{x}}\eta_{\mathbf{y}}] = \delta_{\mathbf{x}\mathbf{y}}$, where $\mathbb{E}_{\eta}[\cdot]$ denotes the expectation value over the random fields η. This scheme amounts to dilution in the time, spin and colour indices with a random wall source. Random wall sources have been investigated in detail in ref. [105] where they were found to be beneficial to obtain good signals especially for finite momentum states. The advantage of using random wall sources is to obtain an estimator with reduced variance by utilising translation variance. For each Monte Carlo sample of the gauge fields the inversion is performed on a single pseudo-random unitary source, $\eta_{\mathbf{x}} \in \mathrm{U}(1)$, generated by Lüscher's `RANLUX` generator [106], and the contraction is performed according to eqn. (2.30). Rather than an explicit inversion, due to the decoupling of the heavy quark and antiquark fields, the solution vectors are determined according to the evolution equation, eqn. (2.22). In this way, the correlation functions are calculated for each of the states listed in table 2.3.

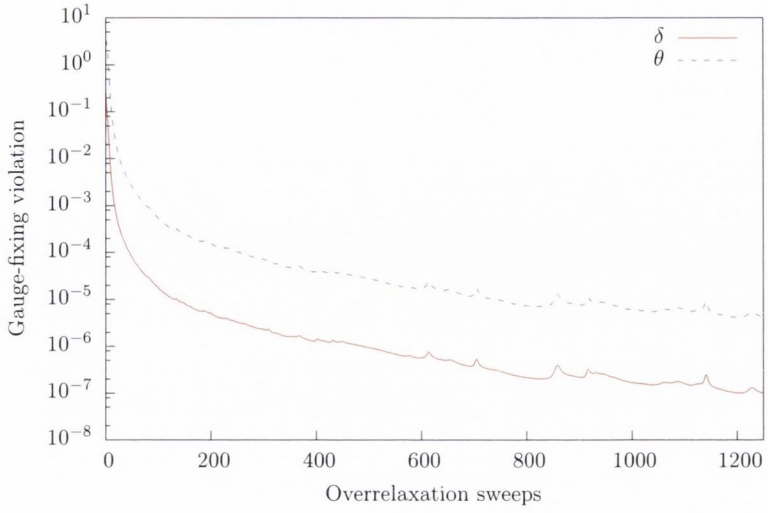

Figure 2.1: Example of the typical behaviour of the gauge fixing violation with number of overrelation iterations from a thermalized configuration on a $V = 24^3 \times 16$ volume.

2.2.2 Gauge fixing

The necessity to fix a gauge is obvious from the non-covariant nature of the sources. The fixing to Coulomb gauge on the lattice was performed by the optimization of the usual transcription of the continuum gauge-fixing functional, $\mathrm{Tr} \int \mathrm{d}^4x \, A_\mu^2(x)$, over gauge transformations $g(x)$ [107]:

$$F_g[U] = \frac{1}{DVN_c} \mathrm{Tr} \sum_{\substack{x \in \Lambda \\ \mu \in \{1,2,3\}}} g(x)(U + U^\dagger) g(x + \hat{\mu})^{-1}, \tag{2.31}$$

where D is the spacetime dimension. The functional was optimized by sweeps of local Cabbibo-Marinari over-relaxation hits on the SU(2) subgroups of each link. The stopping criterion was the difference of the functional between successive sweeps, $\delta = F' - F$, which vanishes asymptotically with the number of sweeps because the algorithm decreases the functional monotonically. The gauge violation is the positive definite measure, θ,

$$\theta = \frac{1}{VN_c} \mathrm{Tr} \sum_{x \in \Lambda} \Delta(x) \Delta^\dagger(x), \tag{2.32}$$

$$\Delta(x) = \sum_{i=1}^{3} \hat{A}_i(x) - \hat{A}_i(x - \hat{\imath}), \tag{2.33}$$

which is a proxy for the derivative of the functional along the optimization trajectory and the correlation between θ and δ is visible from figure 2.1. A tolerance of $\delta < 10^{-7}$, or around machine precision for floats, is reached within about one thousand sweeps.

2.2.3 Fitting and statistics

Fits of the correlation functions to single exponentials motivated by the spectral decomposition of the correlation function, the zero-temperature analogue of eqn. (1.13), were performed using the maximum likelihood method [74]. This model assumes the data, $G = (G_i)_{i=1,\ldots,N}$, estimated by the *sample mean*,

$$G = \frac{1}{|M|} \sum_{G^m \in M} G^m, \tag{2.34}$$

over the set of observations, $M = \{G^{m_1}, G^{m_2}, \ldots\}$, along the Markov chain, to be drawn from a normal distribution. The solution of the non-linear least squares problem is obtained by minimizing the quadratic likelihood over the parameters, $x = (x_p)_{p=1,\ldots,P}$, given the hypothesis, $f(x) = (f_i(x))_{i=1,\ldots,N}$, and the data,

$$x^* = \operatorname*{argmin}_x L(x), \tag{2.35}$$

$$L(x) = (G - f(x))C^{-1}(G - f(x)), \tag{2.36}$$

where the covariance matrix, C, is estimated by Bayes's unbiased sample covariance

$$C = \frac{1}{|M|} \frac{1}{|M| - 1} \sum_{G^m \in M} (G^m - G) \otimes (G^m - G). \tag{2.37}$$

Assuming that the global minimum of the likelihood has been successfully determined, the goodness of fit for the optimum parameters is determined by the standard test of the χ^2-*statistic*, $\chi^2(x^*) = L(x^*)$: if $\chi^2 \gg N - P$ the maximum likelihood interpretation suggests that the data were unlikely to be drawn from the hypothesis whereas if $\chi^2 \ll N - P$ then the parameters are highly sensitive to fluctuations in the data and the resulting parameters may not be trusted. Heuristically, when $\chi^2 \approx N - P$ the expected variations from the normal distribution of the data are sufficient to explain the observed residuals. Alternatively, the *Q-factor*, $Q(\chi^2(x^*), N - P) = p(\chi^2 > \chi^2(x^*), N - P)$, related to the cumulative distribution function of the χ^2-distribution, gives the probability of finding the optimum χ^2 or larger given the normal distribution of the data.

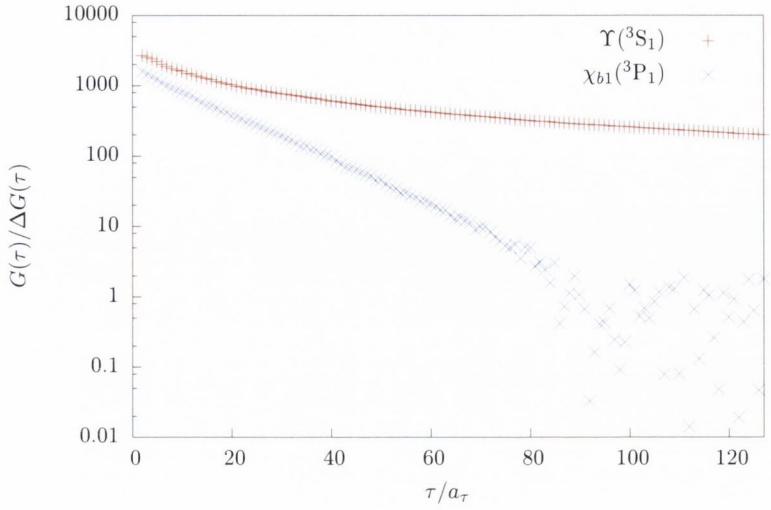

Figure 2.2: Signal-to-noise ratio of the hadronic correlation functions in the S wave and P wave channels demonstrating the exponential decay in the P wave channel with exponent commensurate with the fine splitting, in contrast to the relatively slow decay in the S wave channel.

In order to obtain a confidence interval, or an estimate of the standard error for the parameters, *resampling* of the observations is employed. Resampling is a technique based on the observation that any subset of the measurements, $S_b \subseteq M$, drawn from the original sampling distribution is also a sampling distribution of the given observable. If repetition is allowed and the samples are drawn randomly from M with $|S_b| = |M|$ then the procedure is known as a *bootstrap*. The calculation of any estimators derived from the original distribution, such as the best fit parameters, can be repeated on a number of resamplings $\{S_b\}_{b=1,\ldots,B}$. In the case of the fit this requires the bootstrap sample means

$$\bar{G}^b = \frac{1}{|S_b|} \sum_{G^m \in S_b} G^m, \tag{2.38}$$

to be used in the fit which results in a set of parameters $\{x^{*,b}\}_{b=1,\ldots,B}$, from which the standard error, σ, can be estimated from the diagonal elements of

$$\sigma^2 = \frac{1}{B(B-1)} \sum_{b=1}^{B} (x^* - x^{*,b}) \otimes (x^* - x^{*,b}). \tag{2.39}$$

The distribution of the resampling means is guaranteed to be normal in the limit of a large number of observations by the central limit theorem. This method is used to fit a single-exponential, parameterized by $x = (A, m)$, the amplitude and

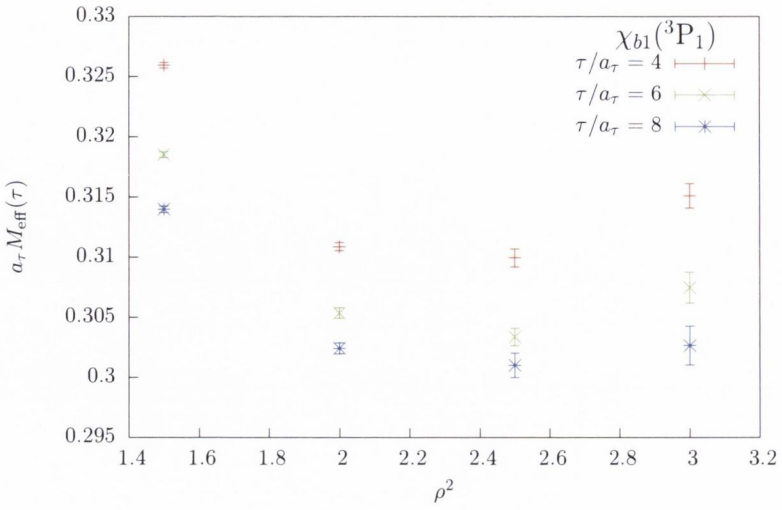

Figure 2.3: An illustration of the determination of the optimum width parameter in the Gaussian smearing. The effective mass at a selection of small Euclidean times is substantially reduced with a finite smearing, maximally reduced at the optimum overlap with the state, between $\rho^2 = 2$ and $\rho^2 = 2.5$.

mass, as $f_i(x) = A\exp(-mi)$ and estimate the standard error on the parameters. The *Levenberg-Marquardt* strategy [108] is a standard heuristic used in in the minimization of non-linear least-squares methods which suggests an increment, $\delta x = x' - x$, defined implicitly by

$$(H + \lambda \mathrm{diag} H)\delta x = -\frac{\partial \chi^2}{\partial x}, \tag{2.40}$$

$$H = \frac{\partial^2 \chi^2}{\partial x \partial x}. \tag{2.41}$$

The choice of damping, λ, adapts the step between gradient descent steps when the damping is large or an approximation to quadratic convergence in the region of a minimum. If a step strictly reduces the χ^2 objective function then it is taken and the damping is reduced assuming the minimum is being approached, otherwise it is rejected and the damping is increased in order for the next step to be closer to the gradient descent move. The minimum is saved, $x^* \leftarrow x'$, when both a tolerance of $\chi^2(x') - \chi^2(x) < 10^{-3}$ and $\lambda < 10^{-5}$ are reached, the second criterion ensuring that a small reduction in the objective function is not due to a tiny step. The single-exponential fits to the correlation functions were performed using this algorithm.

In order to make predictions for the spectrum with accurate estimates for the uncertainties based on the correlators computed in NRQCD, various systematic

effects need to be accounted for. The principal concern in the fitting of the hypothesis to the correlator regards the choice of temporal range of correlator data and the applicability of the model over the temporal domain. On account of both lattice artifacts and excited-state contamination, the short-Euclidean distance part of the correlator is not expected to conform to the hypothesis. Alternatives which account for the overlap of interpolating operators with excited states range from using more complicated fit functions as in multi-exponential fits to eliminating the contamination by construction of a suitable basis of operators. At large distances, due to the deteriorating signal-to-noise ratio, see figures 2.2 and 3.7, the data may not constrain the parameters any further and may only contribute to the uncertainty in their determination. The deterioration of the signal which is evident from the correlators suggests an upper window of $N_\tau/2$ in the axial vector channel, while the largest Euclidean time could be used in the vector channel.

The effective mass plateaus are the typical representation of the correlator data which illustrates the region of applicability of a single-exponential fit. Note that the errors on the observable are obtained by estimating the observable on each bootstrap sample. Smearing the quark source in the interpolating operator reduces the coupling to excited states illustrated in figure 2.3. The smearing parameter which governs the width of the Gaussian wavefunction applied to the source of $\rho^2 = 2.5$ was deemed to minimize the effective mass at various early times, an unsophisticated proxy for the coupling to excited states, without substantially increasing the variance of the observable. This extent is not unreasonable based on the expected size of the quarkonium wavefunction. Figure 2.4 shows the effective mass plateaus in the vector and axial vector channels and the best fit from the fit to the shaded region. Note that correlated fits are essential to performing the fit and obtaining reliable estimates for the statistical error.

The stability of the fit window is judged by examining the τ_{min} plots of figure 2.5 which depict the stability of the best fit parameters as the minimum Euclidean time used in the fit is reduced. The smearing greatly reduces the possible τ_{min} as expected. Reducing the largest Euclidean time used in the fit has a negligible effect on the best fit parameters. In the axial vector channel, the fit for the unsmeared operator is not stable as there is a clear trend in the data as τ_{min} is reduced so smearing is essential to obtain a plateau before the signal degrades completely. In the vector channel, both the smeared and unsmeared operators exhibit large regions of stability of the fit with the central values in good agreement within the statistical uncertainties.

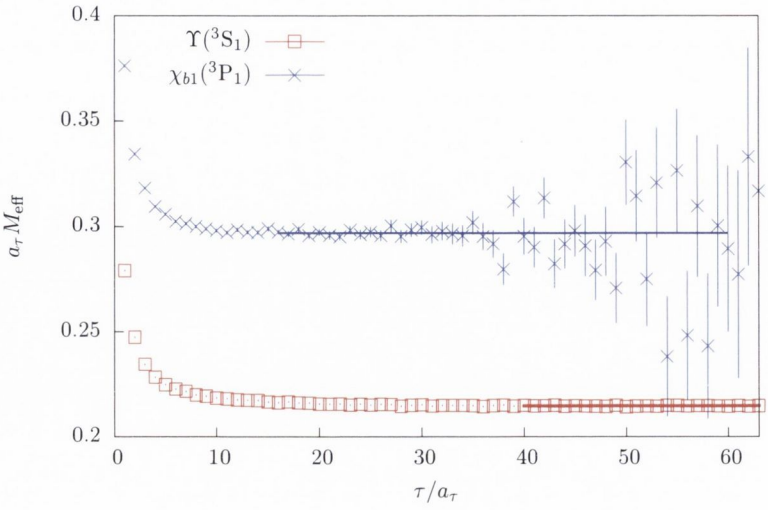

Figure 2.4: The effective mass plateaus in the S wave (red) and P wave (blue) channels with the best fit parameters determined from the single-exponential fits shown in solid lines over the fit range. Error intervals are smaller than the linewidths.

2.2.4 Heavy-quark mass tuning

The heavy quark action contains three free parameters, $a_s m_0$, $a_s m_Q$ and ξ, which are required to be fixed before predictions relating to the physical theory can be made. Both perturbative and non-perturbative prescriptions are commonly used to fix the bare couplings. Non-perturbative tuning requires physical observables such as meson masses, decay constants or dispersion relations to be reproduced in the continuum limit of the lattice calculation, which may or may not be practicable. As the continuum limit is not available to the non-renormalizable effective theory, the tuning is performed at finite lattice spacing, therefore lattice artifacts will result in a minor mistuning of the heavy-quark parameters. The leading heavy quark mass term, $a_s m_0$, is redundant as this coupling can be removed through a redefinition of the fields familiar in any non-relativistic field theory. Consequently it has no effect on the dynamics other than to redefine the absolute energy of the spectrum and may be set to zero. The anisotropy is set to the renormalized value. In principle, it could be measured and tuned along with the heavy quark mass, but the cost of performing a simultaneous tuning would be prohibitive owing to the relative expense of tuning the heavy-quark mass.

The tuning of the heavy quark mass in the lattice action proceeds through the matching of a hadronic kinetic mass, M_2, defined implicitly through the

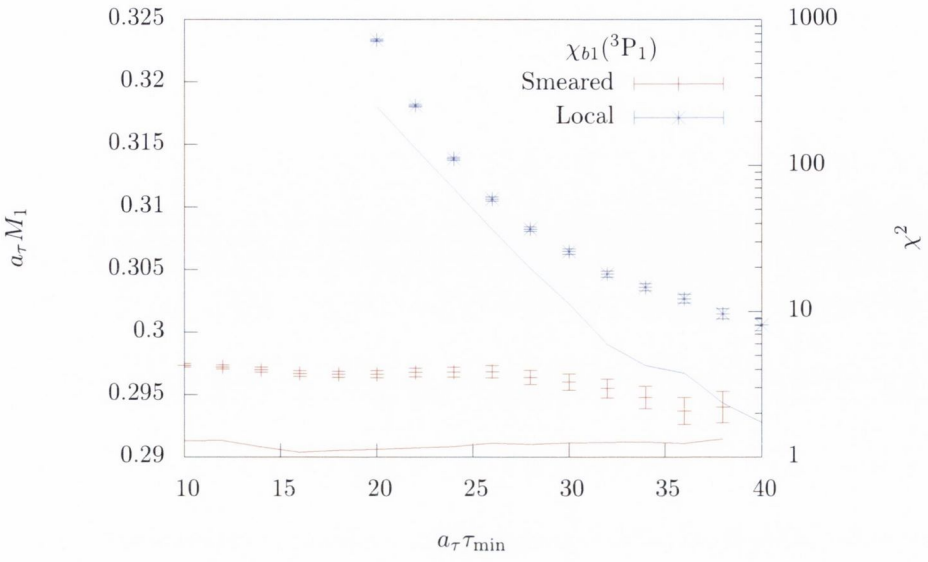

Figure 2.5: Sliding-window plot in the P wave $\chi_{b1}(^3\mathrm{P}_1)$ channel, which demonstrates the stability of the best-fit effective mass parameter (points) and reduced χ^2-statistic (solid lines) as the lower edge of the range of fit window, $\tau_{\min}$, is reduced. This clearly demonstrates the necessity of smearing in this channel.

dispersion relation,

$$a_\tau E(\hat{P}^2) = a_\tau M_1 + \frac{a_s^2 \hat{P}^2}{2\xi^2 a_\tau M_2} + \ldots, \tag{2.42}$$

$$a_s^2 \hat{P}^2 = 4 \sum_{i=1}^{3} \sin^2 \left(\frac{\pi n_i}{N_s} \right), \qquad n_i = 0, \ldots, N_s - 1. \tag{2.43}$$

with the corresponding experimental level. The velocity expansion of the energy for a free two-particle state in a moving frame [109] demonstrates that resolving the kinetic mass to leading order requires the single-particle energy to be resolved to next-to-leading order in v^2. Therefore, only the gross structure of the kinetic mass spectrum can be reproduced as the hyperfine structure encoded in the spin-dependent terms only appears at next-to-leading order. In fact the ordering of the pseudoscalar and vector kinetic masses is inverted with respect to the physical one, as was observed in ref. [109]. The S wave channel, being the lightest and least noisy channel was used for the tuning of the heavy-quark mass. The spin-averaged 1S mass, $M(\overline{1\mathrm{S}}) = (3M(^3\mathrm{S}_1) + M(^1\mathrm{S}_1))/4$, is used to reduce the associated systematic error in matching the kinetic mass because it is independent of hyperfine structure.

The spin-averaged kinetic mass was calculated for a range of values of the

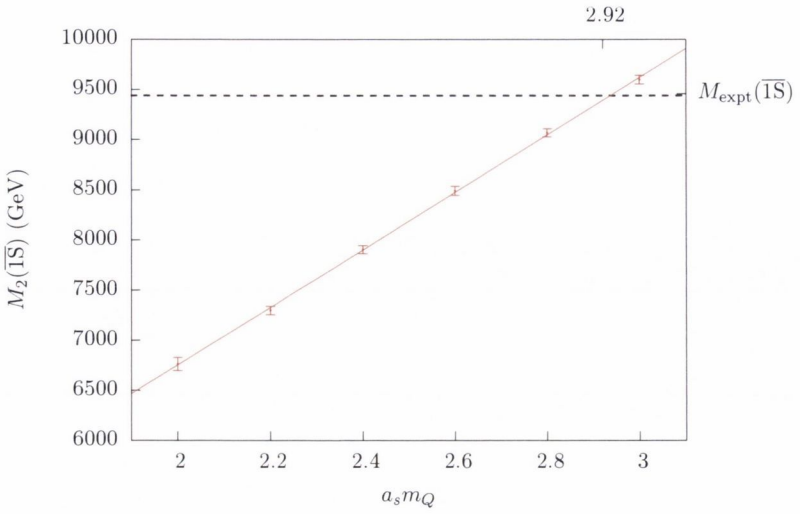

Figure 2.6: The linear interpolation used to determine the lattice heavy quark mass, $a_s m_Q$, by matching with the experimental spin-averaged S wave.

heavy quark mass on a reduced set of statistics of only 30 independent configurations. A remarkably linear relationship between the lattice quark mass and the kinetic hadronic mass can be observed in figure 2.6. This invited a linear fit, and an interpolated value of $a_s m_Q = 2.92$ for the tuned heavy quark mass.

On the full ensemble the dispersion relations were calculated in the pseudoscalar, $\eta_b(^1\mathrm{S}_1)$, and vector, $\Upsilon(^3\mathrm{S}_1)$, channels at this tuned value of the heavy quark mass, depicted in figure 2.7. Linear and quadratic fits in $a_s^2\hat{P}^2$ were performed whose 1σ confidence intervals are shown with dark and light bands respectively, motivated by the possibility of observing relativistic corrections to the dispersion relation. By the goodness of fit, the linear model can be used to fit the data with $\boldsymbol{n}^2 < 4$, while the quadratic fit did not significantly improve the quality of the fit beyond $\boldsymbol{n}^2 > 5$. A conservative estimate for the kinetic mass for the $\eta_b(^1\mathrm{S}_1)$ and $\Upsilon(^3\mathrm{S}_1)$ was made from the linear fit with $\boldsymbol{n}^2 < 4$ with the statistical error obtained from a bootstrap analysis of $|B| = 500$ on $N_c = 300$ measurements. A systematic error is quoted as the difference between the central values of the kinetic masses determined from the linear fit and a quadratic fit using data with $\boldsymbol{n}^2 < 5$. The central value for the coefficient of quadratic term was either not statistically significant, or the inferred value of the kinetic mass by matching with the next order in the relativistic expansion did not generally agree with the mass determined from the term linear in $a_s^2\hat{P}^2$. Further improvement of the action would be required to correctly resolve the coefficient of the quadratic term. This results in a spin-averaged kinetic mass, $M_2(\overline{1\mathrm{S}}) = 9613(84)_{\mathrm{sys}}(40)_{\mathrm{stat}}$

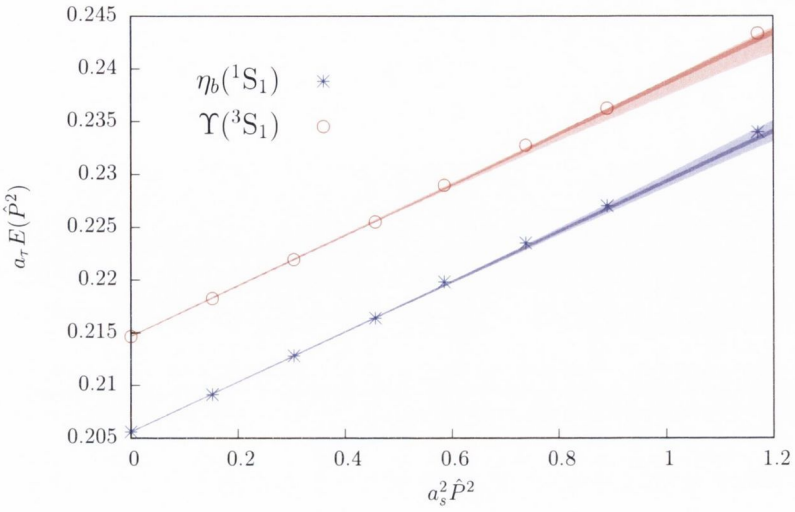

Figure 2.7: The dispersion relations in the S wave spin singlet and triplet channels, with best linear and quadratic fits depicted with dark and light bands, respectively.

MeV, which, while not in exact agreement with the experimental spin-averaged number $M_{\text{expt}}(\overline{1S}) = 9440$ MeV, ought to be sufficient for the investigation of the spectrum at finite temperature where a mistuning of the order of 1% can be tolerated.

Multi-exponential fits were used in the S wave channels to extract the first excited state energies. These were performed using the Bayesian fitting package [111] for which the likelihood function is updated with Gaussian prior. Bayesian methods are explained in further detail in the following section. These multi-exponential fits allow the entire temporal domain of the correlation function to be included in the fit. Priors of $a_\tau M_1 = 0.2(2)$ and $a_\tau \Delta E = 0.1(1)$ were chosen, with distributions which are suitably wide such that no strong bias is introduced in the estimation of the best fit parameters. In order to assess the stability of the fits, the number of exponentials was varied and convergence is seen after five or six exponentials are included from figure 2.8. The standard error on the second excited state fit parameter is not constrained by the data so no reliable signal for higher excited states can be extracted from these fits.

The final spectrum obtained from the correlators computed with the tuned value of the heavy-quark mass on the full ensemble using the fitting strategies outline above is shown in figure 2.9. The energies are shifted, $a_\tau M = \mathcal{E} + a_\tau M_1$, so that the mass of the $\Upsilon(^3S_1)$ state is fixed to its experimental value, that is $E_0 = M_{\text{expt}}(\Upsilon(^3S_1)) - M_1(\Upsilon(^3S_1))$. This extra fixing criterion is equivalent to the omitted tuning of leading heavy-quark mass term, $a_s m_0$.

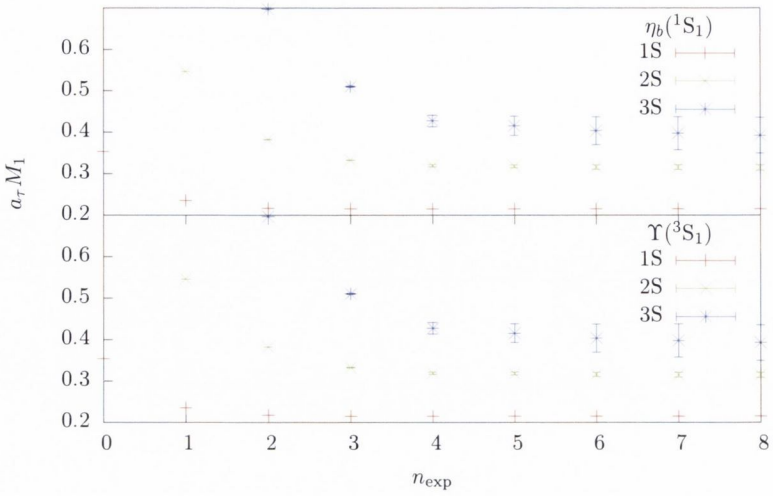

Figure 2.8: Multi-exponential fits with Gaussian priors to the S wave correlation functions stabilize after four or five exponentials are included. The ground state is commensurate with the single exponential fits using including only larger Euclidean times whereas multi-exponential fits can utilize all correlator data.

Good qualitative agreement is seen with the experimental energies, but the splittings are not in agreement within the quoted statistical error. Lattice artifacts and the omission of higher-order improvements to the action may account for the discrepancies, although estimating the systematic uncertainties due to these omissions is a challenging task. The splitting between the two lattice irreducible representations which are subduced from the continuum tensor representation gives an estimate of the systematic error from the finite lattice spacing. The error on the mean value quoted for the tensor representation combines this systematic error in quadrature with the statistical error, which is subdominant. The S wave hyperfine splitting is sensitive to the coefficient of chromomagnetic interaction in the heavy quark action [98]. The effect of tuning this away from its tree-level value is demonstrated by the spectrum in green crosses, in which only this splitting is significantly affected. Therefore, the lack of radiative corrections to the improved action, or the matching of the heavy-quark action at one-loop, is another systematic error. Finally, the analysis of the spectrum was repeated for other values of Lepage's parameter, but no discernible effects could be made out on the spectrum. While this study of the spectrum is relatively unsophisticated it demonstrates the adequacy of the set-up in capturing the relevant physics for the subsequent finite-temperature study.

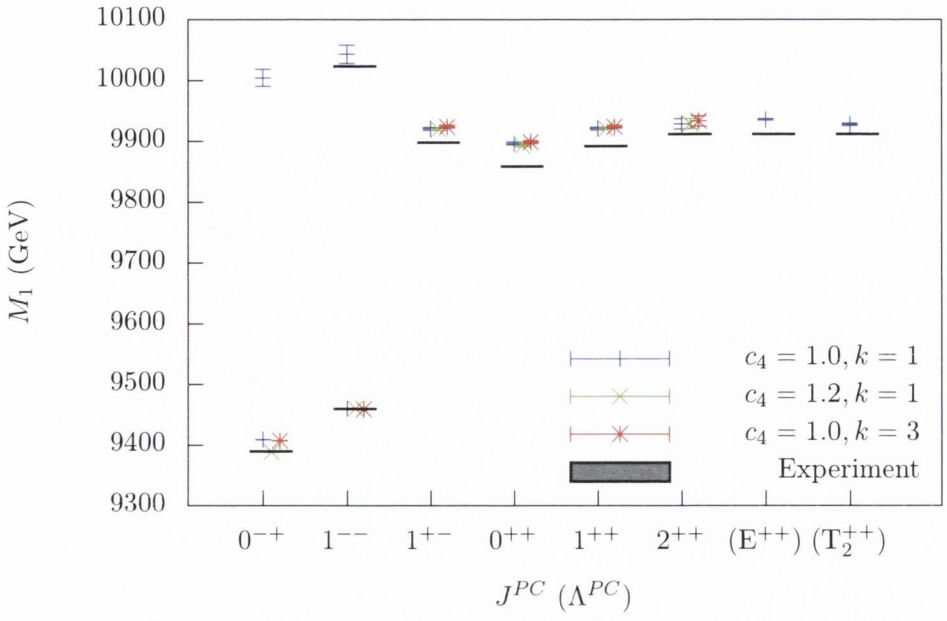

Figure 2.9: Final spectrum with continuum spins identified (blue crosses). The effect of increasing the matching coefficients ad hoc is to change only the hyperfine structure, as expected (green exes). Increasing the stability parameter in the action, n, has a negligible effect on the spectrum (red asterisks). The splitting between the lattice irreducible representations is a lattice artifact, and consequently, a systematic error is added in quadrature with the statistical error for the mean which is the value quoted for the continuum irreducible representation. The data are available in table A.3. The experimental levels are taken from the PDG [110].

2.3 Extracting spectral functions from lattice data

As outlined in the introduction, the spectral function is a valuable object which facilitates the connection between real and imaginary-time correlation functions and also provides a straightforward interpretation of the temperature effects in terms of the in-medium modification of the hadronic spectrum or transport properties in a given channel. Spectral representations of propagators of non-asymptotic states of QCD [112] are also of interest as they encode the important analytic structure of the propagators, for example, positivity violations in the gluon spectral function signal the absence of these states from the physical Hilbert space.

The relationship between the hadronic correlation functions or (quasi-)particle propagators and their associated spectral function is often through an integral transform, usually a Fredholm integral of the first kind. In order to access the

spectral function from the measured data, i.e. correlation function from the lattice, a linear inverse problem, $Kx = y$, must be solved where x and y are elements of some normed spaces X and Y. Recall that in the lattice study, the inverse problem is the extraction of the spectral function from the Euclidean correlation function,

$$D_E(\tau, \mathbf{p}) = \int_{-\infty}^{\infty} \mathrm{d}\omega \, K(\omega, \tau)\rho(\omega, \mathbf{p}), \qquad K(\omega, \tau) = e^{-\omega\tau}, \tag{2.44}$$

where the kernel has been replaced by expanding around m_Q and dropping terms suppressed in the large m_Q/T-limit.

The existence, uniqueness and stability –or well-posedness– of inverse problems such as these are well understood in cases like those encountered in integral transforms where K is always a compact linear operator between Banach e.g. $C[a, b]$, or Hilbert spaces, e.g. $L^2(\mathbb{R})$. They are ill-posed, failing because the stability of the inversion is poor given some deformed data, y^δ, satisfying $\|y^\delta - y\|_Y < \delta$, because the inverse operator is generally unbounded and hence not continuous. Therefore, it can be difficult to make robust conclusions about the spectral function in the case of noisy estimators for the data as in the case of lattice data. In the following section, some basic facts about ill-posed problems are summarized following the presentation of ref. [113].

2.3.1 General regularization strategies

Many approaches have been developed to tackle these instabilities taking inspiration from regularization theory or Bayesian inference. A connection between standard regularizations and Bayesian inference can be demonstrated and can lend an intuitive understanding to the Bayesian approach while adding rigour to the statistical underpinnings of the regularization theory.

Fitting ansaetze with the maximum likelihood method counts among the simplest regularizations of the problem in cases where the number of fit parameters is small relative to the number of available data. Such an overdetermined problem is solved by minimizing the likelihood, in this notation $L = \|Kx - y\|_Y^2$, which gives rise to the usual least-squares fit with the appropriate norm on Y. This is in itself ill-posed as can be seen by recasting the minimization as the solution of the normal equation, $K^*Kx = K^*y$ where $K^* : Y \to X$ is the operator adjoint to K. These approaches are useful when phenomenology strongly constrains or guides spectral features known to exist in the solution. For example, ansatzes for the spectral functions have typically been investigated in the light vector meson channel by fitting with the maximum likelihood method [114]. However,

this model-dependent approach is not adequate where the spectral features may change dramatically as a function of temperature. In this case, establishing the existence of resonances is highly sensitive to the biases introduced by particular models for the spectral function, which we wish to avoid.

Tikhonov regularization is an example of a less prescriptive regularization scheme which has been used to extract gluon spectral functions from propagators estimated in lattice QCD [112]. Loosely, resolving the spectral function in a relatively model-independent way means estimating a large number of parameters, since it is continuous on the positive real axis, and having only a few correlator or propagator data renders the problem highly degenerate. The inverse problem is necessarily ill-conditioned given the low rank of the kernel in this case. The scheme can be seen to be an improvement to the unstable least-squares fitting in the following way.

The idea is to augment the functional to include a penalty term so that the *regularization strategy*, $R_\alpha : Y \to X$, which satisfies $\lim_{\alpha\to 0} R_\alpha K x = x$, amounts to the minimization of $\|Kx - y\|_Y^2 + \alpha\|x\|_X^2$. With perfect data, knowledge of the exact y, the solution obtained converges *pointwise* to the exact one when regularization parameter, α, is removed. However, R_α does not necessarily converge to the identity and there even its operator norm, $\|R_\alpha\|$, diverges as the regulator is removed, as expected due to the ill-posedness of the problem. On the other hand, the approximation error $\|(R_\alpha - K^{-1})x\| \to 0$ as $\alpha \to 0$, so the application of the triangle inequality in Y,

$$\|x_\delta^\alpha - x\| \leq \delta\|R_\alpha\| + \|(R_\alpha - K^{-1})x\|, \tag{2.45}$$

suggests that an optimal non-zero choice for α exists given the asymptotic behaviour of both terms in order to minimize the error in the presence of imperfect data. The scheme to estimate such an optimal choice can be made a priori if some knowledge of the solution is available, for instance bounds on its smoothness, or as in the case used with the gluon spectral functions, can be chosen such that the constraint $\|Kx_\alpha^\delta - y^\delta\| = \delta$ is fulfilled, known as the Morozov discrepancy principle.

The *singular value decomposition (SVD)* of the kernel, K, is the generalization of finite-dimensional matrix decomposition $K = U\Xi V^T$, where the singular values, $\{\mu_j\}_j$, are the elements of the positive semi-definite diagonal matrix Ξ, and $\{x_j\}_j$ and $\{y_j\}_j$ are the columns and rows of the orthogonal matrices U and V^T, called the left and right-singular vectors respectively. It is easy to see that the Tikhonov regularization is simply a screening of the singular values, analogous to the eigenvalues of a symmetric operator, some of which are necessarily

small in the case of the ill-conditioned inverse problem. Writing the solution to the normal equation for the minimization, $\alpha x_\alpha + K^*Kx_\alpha = K^*y$, as

$$(\alpha\mathbb{I} + K^*K)^{-1}K^*y = \sum_{j=0}^{\infty} \frac{\mu_j}{\alpha + \mu_j^2}(y, y_j)x_j \tag{2.46}$$

the regularization parameter is seen to trade between the singular problem and one which has a finite approximation error.

The maximum likelihood interpretation is naturally extended to give a probabilistic origin for the regularized least-squares problem from a Bayesian perspective. Rewriting the identities obtained from marginalizing the joint probability $p(EH)$ over the evidence, E, and the hypothesis, H, leads to an expression for the posterior probability, Bayes's theorem $p(H|E) \propto p(E|H)p(H)$, in terms of the likelihood $p(E|H)$ and the prior $p(H)$. Then the *maximum a posteriori* estimate for the inverse problem is easily related to the regularized least-squares problem when the data are normally distributed and the prior probability is chosen to be a quadratic form:

$$p(E|H) \propto \exp(-\|y - Kx\|_Y^2) \tag{2.47}$$

$$p(H) \propto \exp(-\|x\|_X^2) \tag{2.48}$$

if the regularization parameter is chosen such that the appropriate norms are used. The covariance of the data, being a symmetric bilinear form on Y, can be absorbed into the definition of the norm, $\|\cdot\|_Y$. Since the exponential is monotone, optimizing the posterior probability is equivalent to minimizing the regularized least-squares problem.

2.3.2 Bayesian methods and MEM

The Bayesian interpretation of the regularized inverse problem invites further examination of Bayesian inference to determine the spectral function. Here, the presentation follows that of Asakawa, Hatsuda and Nakahara [115], who pioneered the application to lattice data. The maximum entropy method has also been applied to recover spectral functions obtained from the Dyson-Schwinger equations [116]. For clarity in the following, the replacements $E \to G$ and $H \to \rho$ are made to make contact with the notation used in the inverse problem encountered for the spectral function. Furthermore, the probabilities are conditioned over additional *prior knowledge* known about the solution –such as positivity– information later encoded in the *default model*, m.

The introduction of the quadratic prior in the Tikhonov regularization can

be understood by assuming a Gaussian process underlies the distribution on the space of solutions. However, this term favours solutions which balance the noise with the norm of the solution, or the distance from the default model. Weaker regularizations are possible which can be constructed axiomatically as is demonstrated for the Shannon-Jaynes entropy. This functional should provide a measure on the solutions which favour the default model in the absence of data. The entropy functional can be derived from the Poisson distribution with the application of Stirling's formula. However, it is more useful to derive the functional from the following axioms, which completely determine it, as they better illustrate the underlying assumptions on the prior functional.

1. The penalty should depend only locally on the hypothesis, $\rho(\omega)$, not on its global structure. Therefore, the functional cannot contain derivatives of ρ and must be and integral of the form:

$$S[\rho] = \int \mathrm{d}\mu(\omega)\, s(\rho, \omega) \tag{2.49}$$

2. The functional should not depend on the coordinates chosen on the domain of the hypothesis, known as *reparameterization invariance*. The hypothesis ρ is a density, its area is invariant under reparameterizations $\omega \to \nu(\omega)$ so that it tranforms as $\rho/\rho' = \partial\omega/\partial\nu$. Since the measure $\mathrm{d}\mu(\omega) \equiv \mathrm{d}\omega\, m(\omega)$, is likewise invariant, the quotient ρ/m is scalar under coordinate transformations. In order that the functional be scalar under coordinate transformations it is therefore constrained to be:

$$S[\rho] = \int \mathrm{d}\mu(\omega)\, s(\rho/m) \tag{2.50}$$

3. Should the hypothesis factorize $\rho(\omega_1, \omega_2) = \rho_1(\omega_1)\rho_2(\omega_2)$ for independent variables ω_1 and ω_2, then the stationary point should be the one which optimizes the entropy independently for each factor, which is satisfied if the first variation is additive:

$$\frac{\delta S}{\delta \rho(\omega_1, \omega_2)} = R_1(\omega_1) + R_2(\omega_2) \tag{2.51}$$

This property is obviously reminiscent of the additivity of entropy and is the origin of the familiar *Shannon-Jaynes information entropy* functional

form up to a constant:

$$S[\rho] = \int \mathrm{d}\mu(\omega) \left[\frac{\rho}{m} \log\left(\frac{\rho}{m}\right) - \frac{\rho}{m}\right] \tag{2.52}$$

It is clear that the properties of the logarithm fulfil the requirements of the additivity. Furthermore, the functional is strictly convex, ensuring that the minimum at $\rho = m$ is unique, whence the terminology default model. Without any further constraints, such as those imposed by the evidence, the optimization of the prior leads to this model which encodes all prior knowledge such as the domain and positivity of the spectral function.

The *maximum entropy method (MEM)* is then the inference of the spectral function, ρ_α, obtained by the minimization of the posterior probability with the evidence that is the measured hadronic correlation function, G

$$\underset{\rho_\alpha}{\operatorname{argmax}}\, p(\rho|G\alpha), \tag{2.53}$$

$$\log p(\rho|G\alpha) = L - \alpha S, \tag{2.54}$$

where L is the likelihood function and S is the Shannon-Jaynes information entropy. The inverse problem between finite-dimensional spaces follows from the discretizations of the correlation function, $G = (G_i)_{i=1,\ldots,N_\tau}$, and the candidate spectral function $(\rho_r)_{r=1,\ldots,N_\omega}$

$$G_i \equiv G(a_\tau i) \qquad i \in 0, \ldots, N_\tau - 1, \tag{2.55}$$

$$\rho_r \equiv \rho(r\Delta - \omega_1) \qquad r \in 0, \ldots, N_\omega - 1, \tag{2.56}$$

with integral N_τ and $N_\omega = \Delta^{-1}(\omega_2 - \omega_1)$. The inverse problem of eqn. (2.44) is written in matrix notation as $G = K\rho$, with the kernel, $K = (K_{ir})_{i=1,\ldots,N_\tau, r=1,\ldots,N_\omega}$, of the form $K_{ir} = e^{-(i\Delta)(ra_\tau)}$. The likelihood function for data correlated in Euclidean time is written with the unbiased estimator for the covariance matrix, C, as

$$L = \frac{1}{2}\left(G - K\rho\right) C^{-1} \left(G - K\rho\right), \tag{2.57}$$

$$C = \frac{1}{N\left(N-1\right)} \sum_{m=1}^{N} (G^m - G) \otimes (G^m - G), \tag{2.58}$$

where N is the number of independent measurements used in the estimator $G =$

$1/N \sum_1^N G^m$ for the central data. Using the same notation for the discretization of the default model as the spectral function the entropy is written

$$S = \Delta \sum_{r=0}^{N_\omega - 1} \rho_r - m_r - \rho_r \log(\rho_r / m_r). \tag{2.59}$$

The properly normalized measure on the prior probability can be obtained by comparing with the Poisson distribution which gives $\int [\mathrm{d}\rho] = \prod_{r=0}^{N_\omega - 1} \left(\int \mathrm{d}\sqrt{\rho}_r \sqrt{\alpha} \right)$. Finally, a prescription for the hyperparameter must be chosen, and one alternative is to marginalize over it

$$\rho(\omega) = \int \mathrm{d}\alpha \, \rho_\alpha(\omega) p(\alpha|G). \tag{2.60}$$

Then upon marginalizing over the hypothesis and invoking Bayes's theorem once more, the following approximation is obtained by evaluating the multidimesional integral using the method of steepest descent, not forgetting the factor of $\sqrt{\alpha}$ in the measure

$$p(\alpha|G) \propto \int [\mathrm{d}\rho] \; p(G|\rho\alpha) p(\rho|\alpha) p(\alpha) \tag{2.61}$$

$$\propto p(\alpha) \int [\mathrm{d}\rho] \; p(\rho|\alpha) \tag{2.62}$$

$$\propto p(\alpha) \left(\frac{\alpha^{-N_\omega/2}}{\sqrt{\det Q''}} e^{-Q} \right)_{\rho = \rho_\alpha}. \tag{2.63}$$

The final spectral function is obtained by numerically averaging over the spectral functions with the probability, $p(\alpha|G)$, and Laplace's rule, $p(\alpha) = \text{const}$. The explicit representation used for the determinant is given below with the Hessian, Q'', at the extremum

$$\alpha^{N_\omega} \det Q'' = \exp \mathrm{Tr}(\log Q'' - \log \alpha \mathbb{I}), \tag{2.64}$$

$$Q''(\rho_\alpha) = \left. \frac{\delta^2 Q}{\delta\sqrt{\rho}_r \delta\sqrt{\rho}_s} \right|_{\rho = \rho_\alpha} \tag{2.65}$$

$$\propto \left(\sqrt{\rho}_r \sqrt{\rho}_s \frac{\delta^2 L}{\delta\rho_r \delta\rho_s} - \alpha \sqrt{\rho}_r \sqrt{\rho}_s \frac{\delta^2 S}{\delta\rho_r \delta\rho_s} \right)_{\rho = \rho_\alpha} \tag{2.66}$$

$$\propto \left(\sqrt{\rho}_r \sqrt{\rho}_s \frac{\delta^2 L}{\delta\rho_r \delta\rho_s} - \alpha \Delta \delta_{rs} \right)_{\rho = \rho_\alpha}. \tag{2.67}$$

2.3.3 Implementation of the optimization with Bryan's algorithm

The preceding prescription defines a suitable regularization of the inverse problem derived from a set of reasonable principles which are ideally suited to analyses of spectral densities. However, the construction of the prior probability is not infallible and its deficiencies will be discussed in the following section. The method requires a search for the global extremum of Q in the N_ω-dimensional solution space, which, given that desired resolution from a domain of a few GeV with a resolution of at least tens of MeV is high-dimensional problem. With the exponential parameterization of the spectral function, $\rho_r = m_r e^{\hat{\rho}_r}$, the extrema are the solutions of the following non-linear equation

$$\frac{\delta Q}{\delta \rho_r} = \left(K^T \frac{\delta L}{\delta K \rho} \right)_r - \alpha \Delta \log \frac{\rho_r}{m_r} \stackrel{!}{=} 0, \tag{2.68}$$

from which the following condition on the solution is realized for the new parameterization of the spectral function

$$\alpha \Delta \hat{\boldsymbol{\rho}} = K^T \frac{\delta L}{\delta K \boldsymbol{\rho}} \equiv R. \tag{2.69}$$

From the SVD of the kernel-transpose, $K^T \equiv U \Sigma V^T$, where $U : \mathbb{R}^{N_\omega} \to \mathbb{R}^{N_\tau}$, this representation of solution is an element of the column space of U, which is only of dimension N_τ, the maximum rank of the kernel. The searching of this N_τ-dimensional space is computationally much less demanding than exploring the entire N_ω-dimensional space of spectral functions and is due to Bryan [117]. The Newton algorithm is used to find the roots of the equation in the usual way by determining the increment between successive guesses:

$$\hat{\rho}' - \hat{\rho} = \left(\alpha \Delta + \mu + \frac{\delta R}{\delta \hat{\rho}} \right)^{-1} [\alpha \Delta \hat{\rho} + R] \tag{2.70}$$

where μ is the Levenberg-Marquardt parameter, and the matrix inverse is computed by going to a diagonal basis. The Levenberg-Marquardt parameter is increased tenfold if the increment is deemed too large for the Newton approximation to hold. Once the stopping criterion is reached by convergence of the norm of $R + \alpha \Delta \hat{\rho}$, the spectral function given the hyperparameter α is saved and the probability $p(\alpha|G)$ is evaluated according to eqn.(2.63). In summary, the method proceeds according to the following scheme:

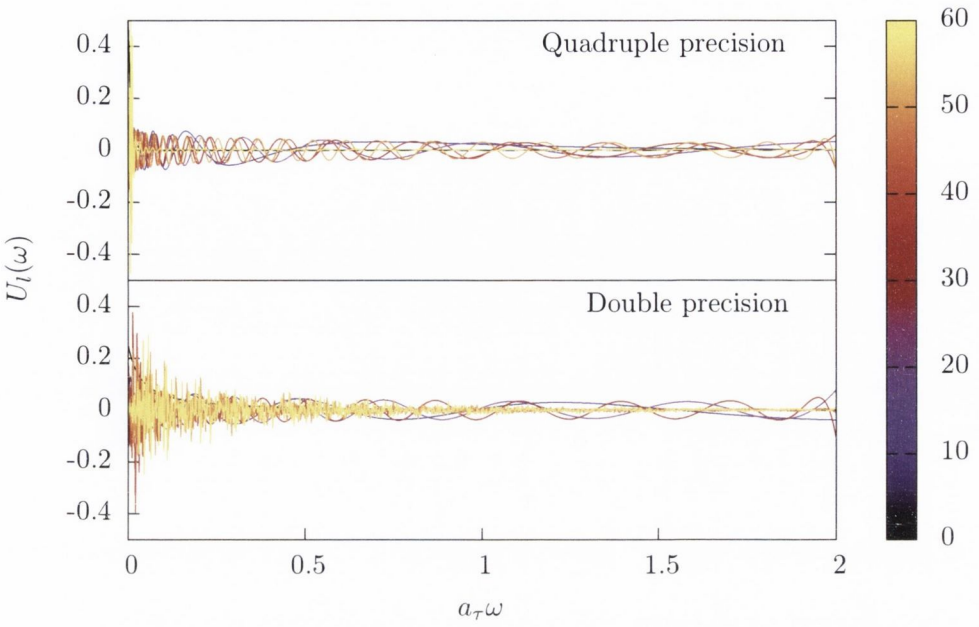

Figure 2.10: A comparison between the SVD basis functions, which are the columns of the matrix U in the SVD, using quadruple precision (top) and double precision (bottom). Note the high precision needed to correctly perform the singular value decomposition of the kernel which is exponentially damped.

1. The singular value decomposition of the kernel is performed, depending only on the number of correlator data.
2. Given a default model the Newton method is used to solve the normal equations for the minimization problem over the singular space for each value of the hyperparameter in a test interval.
3. If the descent step is too large, then increase the Levenberg-Marquardt parameter and try again.
4. When convergence of the norm of the system of equations is reached the probability, $p(\alpha|G)$, is evaluated.
5. The solutions are integrated over the hyperparameter over the domain defined through $p(\alpha|G) \geq 0.1 \times p(\alpha^*|G)$.

Due to the exponential damping of the kernel, $K = e^{-\omega\tau}$, an implementation

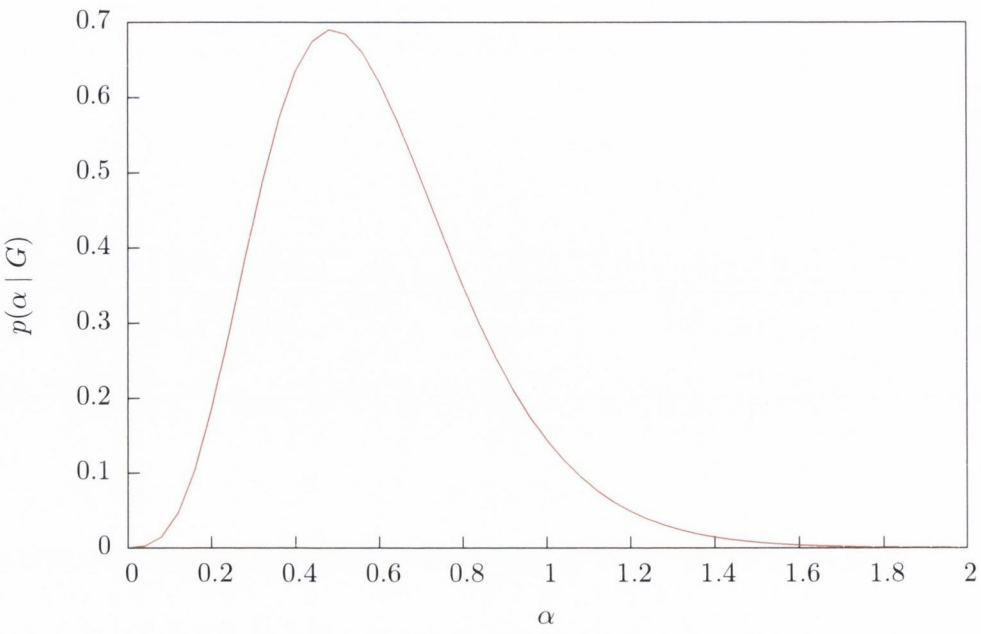

Figure 2.11: Example of the probability distribution, $p(\alpha|G)$, from the reconstruction of the spectral function in a P wave channel with $N_\tau = 16$, sharply peaked around $\alpha^* = 0.5$ in this case.

with quadruple precision is required. Figures 2.10 depict examples of the basis over which the solution is reconstructed. For these correlators at low temperatures with $N_\tau = 128$, the convergence is slow given the relatively high dimension of the reduced problem, visible in figure 2.13. The probability distribution, $p(\alpha|G)$, is very peaked, an example is shown in figure 2.11, and the variation of the solution over the range of α investigated was observed to be small.

2.3.4 Spectral functions from MEM

The implementation of MEM by the authors of ref. [118] was applied to the zero temperature bottomonium correlation functions computed in NRQCD. Figure 2.12 shows the resulting spectral functions in the S wave (left) and P wave (right). In order to cast the frequency domain in physical units, the same shift in the energies, $\mathcal{E}$, is applied to the frequency axis as for the spectrum obtained in the previous section.

In the S wave channel good agreement is observed between the lowest peaks and the corresponding ground and first excited-state energies extracted from multi-exponential fits directly to the correlators. Recall that energies for higher excitations could not be reliably extracted from the multi-exponential fits to the

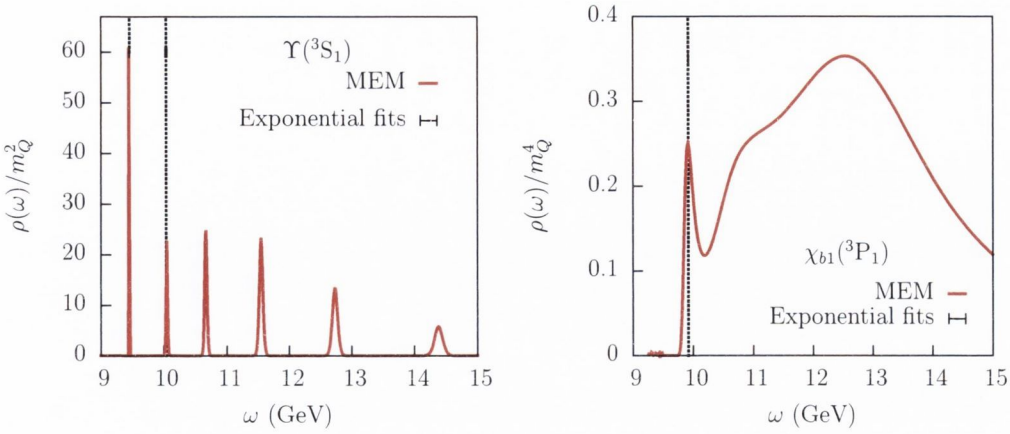

Figure 2.12: Reconstructed spectral functions in the S wave (left) and P wave (right) channels using the maximum entropy method. While as many as six peaks can be located in the S wave channel, just the first two are commensurate with the experimental energies. The energies also agree with those extracted directly from the correlation functions with multi-exponential fits. In the P wave channel, the ground state peak is resolved nicely, while lattice artifacts presumably contribute to the background structure at higher energies.

correlator. Furthermore, it is obvious that lattice artifacts will contaminate the spectral function at energies of a few GeV above the threshold.

The ground state peak and corresponding energy from the fits the correlator is in good agreement in the P wave channel. However, above the ground-state peak a large continuum is observed in this channel. Due to the derivative coupling in the P wave channel, the divergences in the non-renormalized channel are worse than in the S wave channel. The lower statistical precision in this channel reduce the number of informative correlator data which can be used in the reconstruction. The challenge of reliably reconstructing the P wave channel spectral function is already evident from these low temperature reconstructions.

The S wave channel spectral function was also calculated with the publicly available `ExtMEM` package [119]. Instead of performing the optimization of the regularized functional by solving the system of normal equations, the direct optimization of the functional is performed using a quasi-Newton algorithm [108]. This is one where an approximation of the Hessian is used to propose an trial solution and can be more efficient for optimization in high-dimensional spaces. Good agreement is seen between the positions of the first two peaks, however, discrepancies between the peaks at higher energies. The displacement of higher peaks could be attributed to the degeneracy along similar directions in the SVD basis space for which it is plausible that different frequencies could compete with

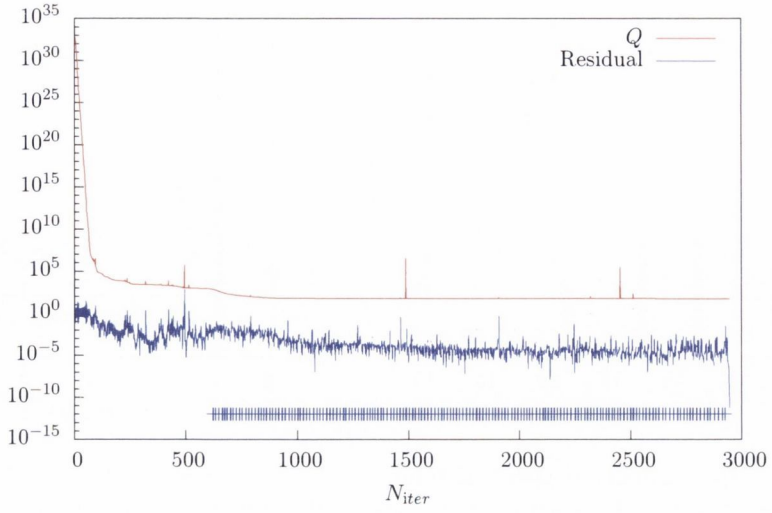

Figure 2.13: The optimization of the objective function, Q, with the LBFGS algorithm in the implementation of `ExtMEM`. The residual, $Q - Q'$, vanishes frequently, marked by the blue crosses beneath the residual line, possibly due to flat directions in the search space.

one and another.

The convergence in the objective Q functional versus the number of iterations is shown in the figure 2.13. Note that zeroes in the residual $Q' - Q$, depicted with crosses below the lines, can arise when long flat valleys are traversed in the functional space and are evidence of many local extrema which are characteristic of the optimization problem in such a high-dimensional space. The generic behaviour is illustrated by this figure in which the variance of Q is large before rapid convergence to the optimum.

2.3.5 Criticisms of Bryan's algorithm

It has been asserted that the global minimum of Q is not in fact contained within the singular space [119]. This claim is supported by two observations. Firstly, by simply shifting the lower boundary of the frequency interval to more negative values, it appears as though the basis functions do not have adequate support over the entire frequency interval to sufficiently reconstruct peaked features at large frequencies. Secondly, it has been observed that by extending the basis used in the minimization to include basis vectors from a kernel with a larger $N_\tau + N_{\text{ext}}$-dimensional singular space, a better optimum of Q can be found. This is posited as a direct counterclaim to Bryan's argument.

Both of these observations are based on numerical mock analyses and have

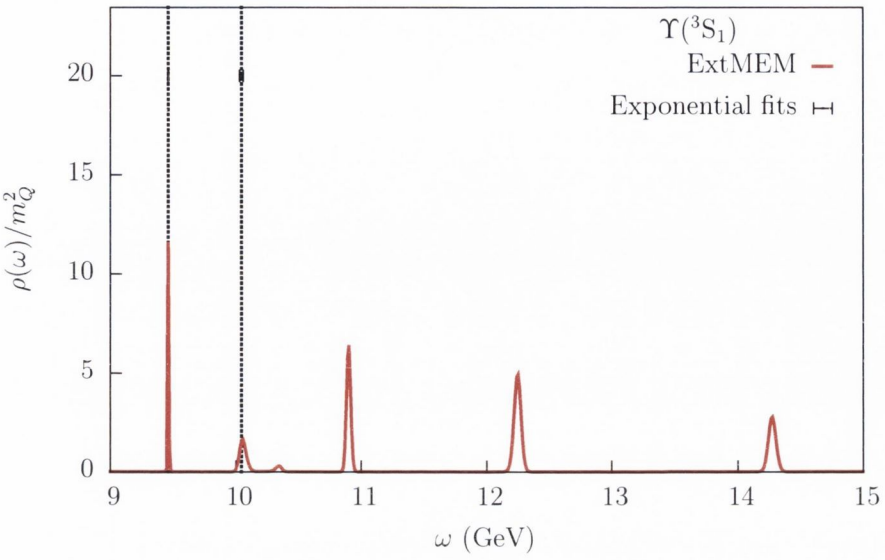

Figure 2.14: Reconstructed spectral function in the S wave channel using the `ExtMEM` package [119] utilizing a direct quasi-Newton optimization of the regularization functional. The ground state peak and first excited state peak agree with energies extracted from multi-exponential fits, The features are comparable with the MEM presented in figure 2.12, but notably the positions of the higher peaks are not in agreement suggesting they are artifacts of the reconstruction. While the relative heights of the first peaks are similar, also the absolute heights deviate significantly.

not been formally realised. Large cancellations can indeed occur as shown in the reconstruction of mock spectral function in figure 2.15 in order to reproduce peaks where it may seem unlikely at first glance of the SVD basis. However, it is undeniable that the reconstruction fails to capture the width of the peak adequately if the left-hand edge of the frequency interval is shifted to negative-enough values. As the minimum frequency is reduced while the frequency and temporal discretizations are left unchanged the problem becomes more ill-conditioned as the difference between N_ω and N_τ grows. To improve the conditioning of the inverse problem as much as possible the frequency domain ought to resemble the support of the unknown spectral function as closely as possible, so that from a practical perspective the minimum frequency should not be reduced arbitrarily. Furthermore, given the temporal discretization of the correlator, one should not expect to resolve the moments of the spectral function at arbitrarily high frequencies above the lower edge of the frequency domain. This is simply the nature of the cutoff scale provided by the temporal discretization and the inverse Laplace transform. Consequently, reducing the lower edge of the frequency window with-

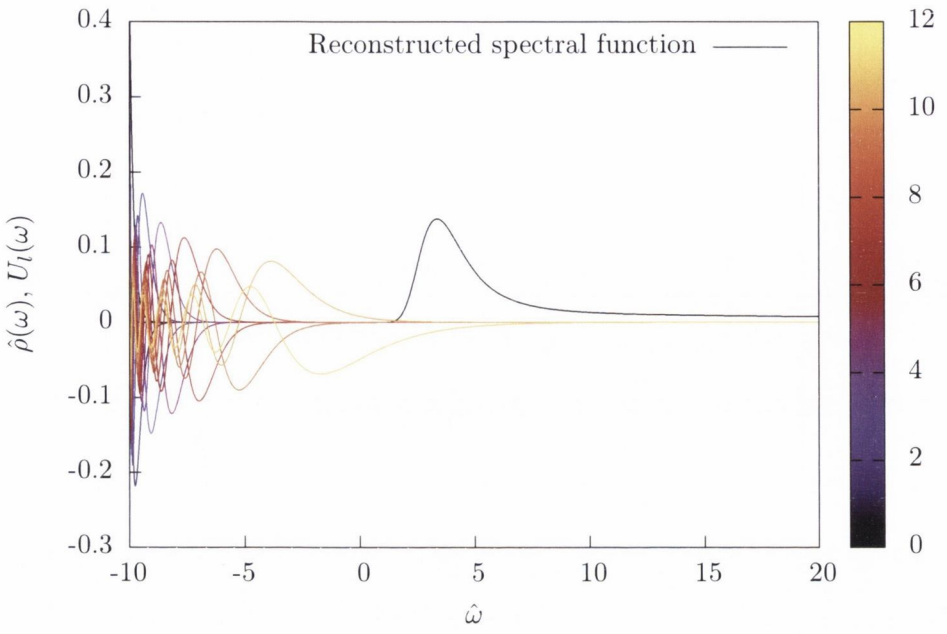

Figure 2.15: Reconstruction of a mock spectral function over a large frequency domain illustrating the strong cancellations in the basis functions in the low-frequency part of the spectral functions and the difficulty in extracting accurate widths if the frequency domain is not chosen with care.

out redefining the threshold of the spectral function appropriately should not be too concerning if the frequency interval is chosen judiciously.

More worrying is the observation that lower minima of Q are encountered when exploring the extended SVD space of dimension $N_\tau + N_{\text{ext}}$ compared with those achieved by exploring only Bryan's subspace. This certainly reflects the inherent difficulty in optimizing the functional even when restricted to Bryan's subspace. However, it may be that the final solution returns to Bryan's subspace at the extremum, and that searching orthogonal directions may provide a trick to tunnel out of local minima in Bryan's subspace in the search for the global extremum.

Naturally, these points raise valid concerns with Bryan's algorithm and motivate solutions which ameliorate the difficult optimization problem. In the following chapter, the variation of N_τ in the fixed-scale approach to changing the temperature also invites us to seek methods whose systematics are minimally dependent on N_τ. Obviously, the conclusions of the N_τ-dependence of the reconstruction should be due to the physical temperature effects and not from the different dimension of the basis for reconstructions. Nevertheless, the conceptual difficulties associated with Bryan's algorithm and the dependence of the opti-

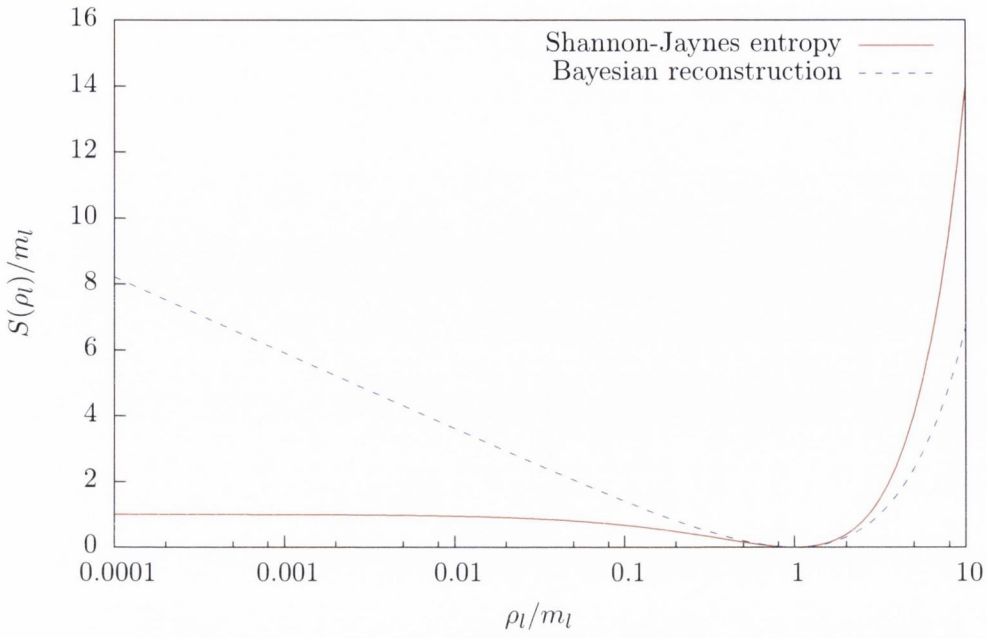

Figure 2.16: Comparison between the integrand of the regularization functional for the maximum entropy method (solid line) and the Bayesian reconstruction method (dashed line). The flat directions in the Shannon-Jaynes entropy at small $\rho_l m_l$ are absent in the Bayesian reconstruction. Furthermore, at large ρ_l, m_l the Bayesian reconstruction poses a weaker regularization, allowing peaked structures to persist where they are encoded in the data through the likelihood.

mization on N_τ reinforces the difficulty in extracting reliable results from fewer and fewer correlator data, the perennial issue encountered in lattice studies at high temperature. To reiterate, the only guarantee that Bryan's method makes, if the global extremum is successfully found, is that this extremum corresponds to the unique spectral function which reproduces the available data with the constraints imposed by the regularization. Ultimately, there is no substitute for good quality data.

2.3.6 Bayesian reconstruction method

In order to decouple the solution of the inverse problem from the dependence on the singular space a refinement of the regularization for the particular problem encountered in the lattice data was proposed by Rothkopf and Burnier [120], referred to as the *Bayesian reconstruction (BR)* in the following. The principal idea is to replace the regularization functional with one well-motivated by the inherent issues of lattice QCD spectra which solves the probelm of the almost-flat directions in the entropy functional which are visible in figure 2.16. Then,

the full solution space can be efficiently explored by standard methods.

The derivation of a new regularization proceeds as before by building the functional axiomatically as follows. These criteria must be scrutinized closely in case that the regularization puts undue constraints on the solution to the optimization.

1. The first criteria is the locality of the functional, identical to that posed in for the entropy, so the functional takes the form of an integral as before.

$$S[\rho] = \int \mathrm{d}\mu(\omega)\, s(\rho) \tag{2.71}$$

2. Scaling of the spectral density. The integrand should not depend on the choice of units for the spectral function, leaving only quotients, ρ_r/m_r, available as dimensionless arguments for the integrand. This axiom already deviates from the entropy's claim for the scaling of the spectral density like a distribution. Cited as counterexample is the spectral functions' perturbative behaviour which is polynomial. This brings the complication of a dimensional hyperparameter, $\tilde{\alpha}$, to ensure the functional itself remains dimensionless.

$$S[\rho] = \tilde{\alpha} \int \mathrm{d}\omega\, s(\rho/m) \tag{2.72}$$

3. The functional form is really introduced by this axiom which demands the curvature of the integrand to be $s''(r) = -1/r^2$ and results in the logarithm. The integration of this differential equation yields

$$s(\rho/m) = \log\left(\frac{\rho}{m}\right) - \frac{\rho}{m} + \text{const} \tag{2.73}$$

From a regularization perspective this can be viewed as a penalty on relative scaling the spectral function parametrically with the default model. Therefore, if, say at adjacent frequencies the spectral function changes by a relative amount $(1 + \varepsilon)$ then there is guaranteed to be a fixed increase in the penalty functional in that region. This damps large relative variations in the spectral function, caused by peaks. Recall that this ought not to affect peaks encoded in the data which are strongly favoured by the likelihood function, only those which appear in the absence of data. Note that penalizing absolute changes in the spectral function would result in a quadratic regularization. This criterion suppresses large variations in the

spectral density in the absence of data which particularly afflict the spectral analysis of lattice correlators where false peaks, which are also observed in mock analyses, can complicate the interpretation of the data.

4. The final functional form is fixed by requiring the relevant critical behaviour at the minimum prescribed by the adherence to the default model.

$$s(\rho/m) = \log\left(\frac{\rho}{m}\right) - \frac{\rho}{m} + 1 \tag{2.74}$$

As can be seen in figure 2.16, the new functional form behaves noticeably differently at small values of the reduced spectral function, where the asymptotically flat directions are removed. Furthermore, at large values of the reduced spectral function, the functional form imposes a weaker regularization than that of the MEM. This penalty serves to inflate the spectral function in regions where the density is not constrained by the data, in essence washing out regions of low spectral density.

The search of the full N_ω-dimensional solution space is possible with the new regularization of the likelihood using a quasi-Newton algorithm. The optimization used in the implementation of the BR method developed by A. Rothkopf and Y. Burnier, the authors of ref. [120], uses the `ALGLIB` [121] implementation of the LBFGS algorithm. Note that the optimization problem is no longer recast as the solution of the multidimensional system of equations because the SVD of the kernel no longer plays a prominent role.

The LBFGS algorithm proceeds just as for the Newton method search for the iterate, $\boldsymbol{\delta x}_k$, by solving the normal equation $H_k \boldsymbol{\delta x}_k = \boldsymbol{\nabla} Q(\boldsymbol{x}_{k+1}) - \boldsymbol{\nabla} Q(\boldsymbol{x}_k)$. Instead, an approximation for H_{k+1}^{-1} is made in terms of tensor products of $\boldsymbol{\delta x_k}$, $H_k^{-1}(\boldsymbol{\nabla} Q(\boldsymbol{x}_{k+1}) - \boldsymbol{\nabla} Q(\boldsymbol{x}_k))$ which is much more cost effective than performing the matrix inversion, especially in a high-dimensional space. Alternatively, the implementation can use the quasi-Newton method as a preconditioner for ordinary Levenberg-Marquardt optimization which utilize the exact inverse of the Hessian.

2.3.7 Spectral functions from Bayesian reconstruction

The implementation of BR method by Rothkopf and Burnier was used to obtain the spectral functions presented in this section. The results are shown in figure 2.17 in the S wave (left) and P wave (right) channels. The S wave spectral functions displays some notable features to be contrasted with the result

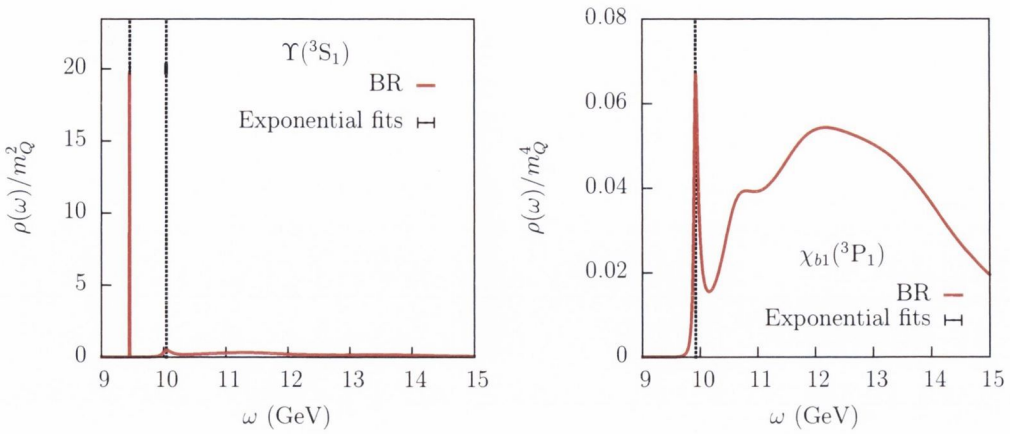

Figure 2.17: Resulting spectra in the S wave (left) and P wave (right) channels. Similar to MEM, the ground and first excited state peak positions agree with the energies extracted from exponential fits to the correlation functions in the S wave channel. However, the discrepancy between the peak heights is much larger, and no more than two peaks are discernible, presumably due to the effect of the new regularization suppressing artificial peaks in the data. The spectral function in the P wave channel is remarkably similar to MEM, dominated by lattice artifacts above the ground state peak.

from the MEM. The position of the ground state and first excited state peaks are in agreement with those from the MEM, however, the BR method does not find narrow peaks in the high-frequency part of the spectral function. This is in accordance with the understanding of the new regularization which washes out artificial peaks which are not encoded in the data, by favouring the default model. The features of the P wave reconstruction are remarkably similar to the MEM with a ground-peak coincident with the single-exponential fit and a large continuum feature at higher frequencies.

Similar conclusions can be drawn from both the MEM and the BR method for this low-temperature data which agree with the energies which were extracted directly from the correlation functions. However, the new BR method performs better in the sense that it does not produce false positives in the form of peaked structures where none exist in the data which is a valuable attribute for interpretation of lattice data.

Further discussion of the systematic dependence of the reconstruction on the frequency and temporal domain is postponed until the next chapter, although figure 2.18 demonstrates the stability of the lowest peaks in the S wave (left) and P wave (right) channels under variations of the lower frequency domain and under variations of the upper and lower window of the correlator. The variation of the

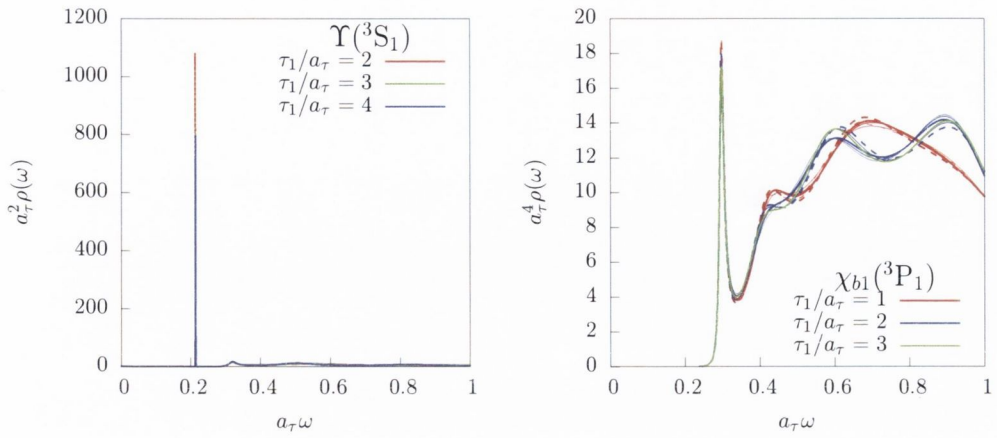

Figure 2.18: Systematic dependence of the reconstruction on the bottom correlator window, τ_1, in the S wave (left) and P wave (right) panels. Different linewidths denote the variation of the upper window, τ_2, which are not visibly different. Dashed lines denote a lower frequency interval $\omega_1 = -0.4$ while solid lines denote $\omega_1 = -0.2$.

spectral function within the statistical error bands in the noisier P wave channel, shown figure 2.19, does not suggest that the statistical error is the dominant uncertainty.

Finally, the momentum-dependence of the S wave spectral function is included in figure 2.20 which demonstrates the agreement of the peak position at finite momentum with the dispersion relation of the S wave state extracted from exponential fits depicted with the solid lines at the top edge of the figure. No significant dependence of the peak width on the momentum is visible. Small discrepancies in the peak heights at different momenta may arise from the different degeneracies of lattice momenta which alter the variance of the estimators at different momenta. The possibility to extract the in-medium dispersion relation is another advantage of the reconstruction of the spectral function which would otherwise be a difficult observable to reconstruct directly from the Euclidean correlation functions when the peaks attain a finite width.

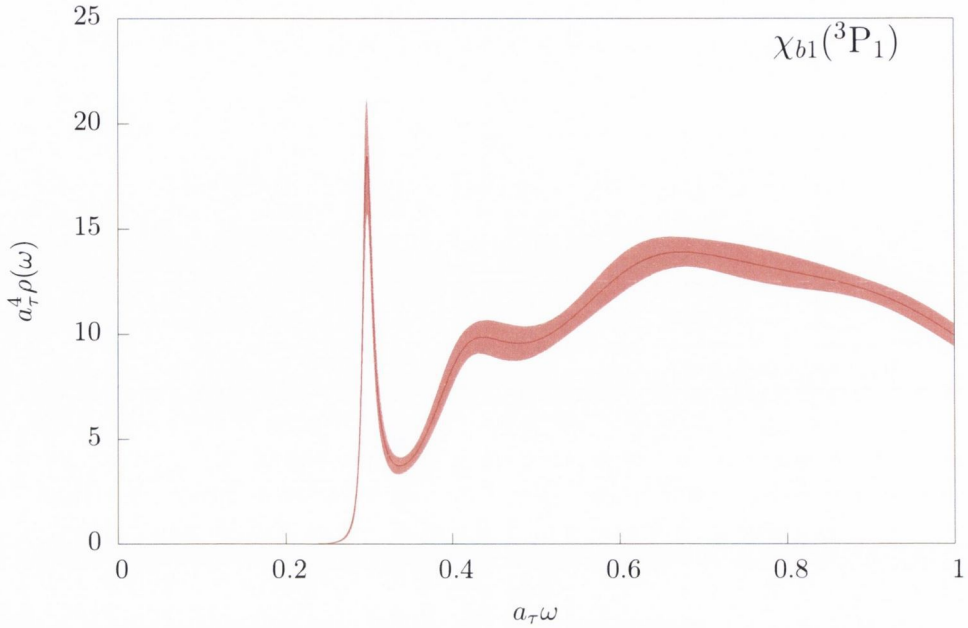

Figure 2.19: The statistical error bands on the reconstructed spectral function in the P wave channel estimated using 50 jackknife blocks.

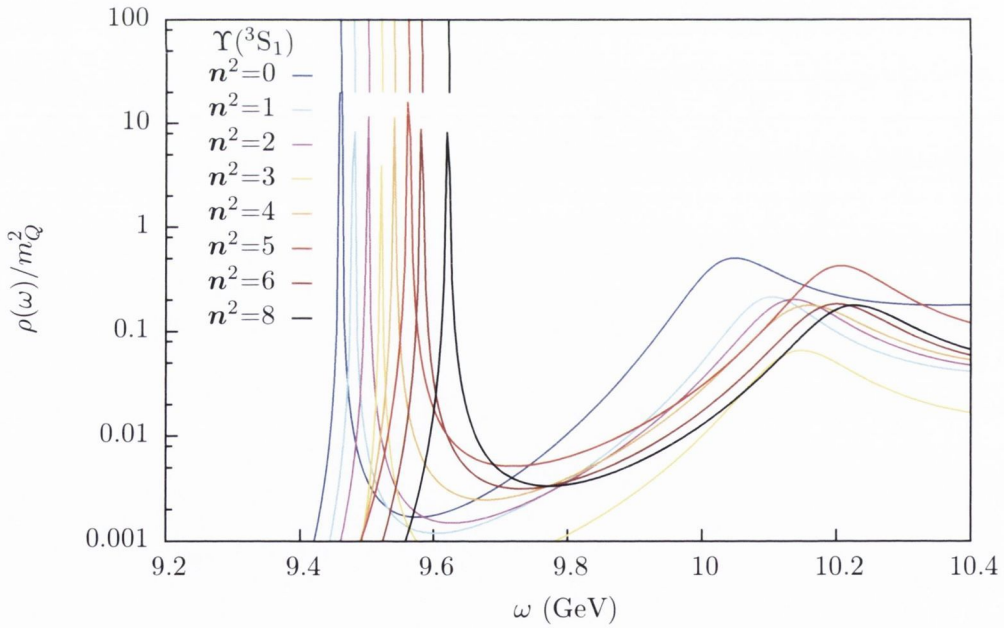

Figure 2.20: Momentum-dependence of the spectral function in the S wave channel with peak positions in agreement with the dispersion relation extracted from fits to the correlation functions, denoted by the coloured lines at the figure's top edge.

3 Bottomonium at finite temperature

In this chapter the modification of the bottomonium spectrum at finite temperature is presented. The results indicate significant differences between the qualitative behaviour in the S wave and P wave channels in bottomonium above the deconfinement crossover temperature. The comparison of the behaviour of the correlation functions to those of non-interacting quarks in NRQCD suggests the unbinding of the quarks in the P wave channel. Further interpretation is provided by the reconstructed spectral functions. The reconstructed spectral functions are presented from the maximum entropy method and the Bayesian reconstruction method. The qualitative features of the spectral function in the S wave channel are the same in both methods but substantial differences are observed in the P wave channel. The systematic dependence of the reconstruction on the available correlator data is discussed. First, a brief exposition of lattice QCD at finite temperature is made.

3.1 Finite temperature lattice QCD

As outlined in the introduction, the Matsubara formalism enables the QCD partition to be evaluated as a path integral in Euclidean space with finite temporal extent corresponding to the inverse temperature, β, and appropriate temporal boundary conditions for the dynamical fields [122, 46]. Therefore, it is straightforward to estimate thermal correlation functions in lattice QCD as the Euclidean formulation is the one used in numerical simulations. Only the physical temporal extent is required to be adjusted in order to change the temperature.

There are two ways to vary the temperature commonly employed by practitioners which are the *fixed-scale* and *fixed-N_τ* approaches, namely when the number of sites in the temporal direction or the lattice spacing are changed, respectively. Shifted boundary conditions have been recently proposed through which the temperature in a fixed-scale simulation can be varied more finely by in-

voking the Poincaré symmetry of the partition sum [123]. The fixed-N_τ approach is perhaps more common in lattice calculations of the equation of state or the deconfinement transition temperature due to the fine control of the temperature afforded by the continuous adjustment of the lattice spacing [25, 124]. In principle, however, the fixed-N_τ approach requires auxiliary zero-temperature calculations at each temperature in order to non-perturbatively tune the parameters of the action, such as quark masses and renormalization constants. In practice this may not be necessary if it is possible to interpolate between simulations at a reduced set of lattice spacings. The accompanying small lattice-spacing zero-temperature simulations which must be performed soon become unfeasible due to the large spatial volumes required. Furthermore, the cost of these simulations increases greatly as the temperature is increased due to the critical slowing of the HMC with the lattice spacing [78]. This greatly restricts the accessible temperatures in dynamical simulations. Additionally, discretization effects become manifestly temperature-dependent and can complicate the physical temperature-dependence of observables.

The ensembles used in this work were generated in the fixed-scale approach by the FASTSUM collaboration using European PRACE and British DiRAC resources [125, 126]. The same parameters were used as those in the zero-temperature ensembles from the Hadron Spectrum Collaboration [127], see table 2.1. The principal advantage is that the cost of the simulations do not increase with increasing temperature. Only a single zero-temperature ensemble is required for tuning so only one simulation is required for each temperature investigated. In order to achieve adequately high temperatures without losing sufficient temporal resolution of correlation functions the benefit of using anisotropic lattices at finite temperature is obvious. As described in chapter 2, this introduces two additional couplings which complicates the tuning of the lattice parameters at zero-temperature. However this task needs to be performed only once.

In the simulations employed in this work the number of sites in the temporal direction at the highest temperature available is comparable to that in a fixed-N_τ approach. Therefore long Markov chains can be accessed without the cost of a study performed with a fixed-N_τ scheme [128]. Additionally, in the fixed-scale approach the spatial volume is unchanging with temperature so that finite-volume effects are not temperature-dependent. However, in this work just a single volume was used so finite volume effects cannot be quantified. For the quantities of interest these effects ought not to be very troubling due to the large box size, $L/a = 24$, compared with the small physical size of the bottomonium ground state, $r_\Upsilon/a \sim 1/(am_b v) \approx 3$. Finite-volume effects in the free spectral

N_s	16	24	24	24	24	24	24	24
N_τ	128	40	36	32	28	24	20	16
T/T_c	~ 0	0.76	0.84	0.95	1.09	1.27	1.52	1.90
T (MeV)	~ 0	141	156	176	201	235	281	352
N_{cfg}	499	502	503	998	1001	1002	1000	1042

Table 3.1: Summary of the ensembles used in this work. The crossover temperature is determined from the renormalized Polyakov loop [126]. The zero temperature tuning of the lattice parameters was completed by the Hadron Spectrum Collaboration [127].

function are further discussed in section 3.2. With the advent of relatively cheap observables to tune the gauge anisotropy, such as the energy density in the Wilson flow [129], it may be advantageous to work with variable temporal couplings only, in order to combine the advantages of both approaches. The simulations proceed exactly as for the zero-temperature ones described in chapter 2. The available temperatures and number of independent configurations are shown in table 3.1.

In order to make contact with QCD with physical quark masses it is most instructive to cast the temperature in terms of the deconfinement crossover temperature, T_c, which naturally depends on the flavour content and quark masses of the theory. Note that the interaction measure depends strongly on the number of active flavours and while the quark masses are unphysically large with $M_\pi/M_\rho \approx 0.45$, this is expected to be a less significant systematic effect at temperatures above the deconfinement crossover temperature.

A renormalization scheme for the Polyakov loop was chosen by normalizing it to unity at a temperature corresponding to an inverse temperature $\beta_0 = 16a_\tau$,

$$L_{\text{ren}}(\beta) \equiv \frac{L_0(\beta)}{L_0(\beta_0)}, \quad \text{with} \quad L_0(\beta) = \langle \text{Tr} P(\boldsymbol{x}) \rangle. \tag{3.1}$$

This scheme amounts to fixing the static-quark free energy of eqn. 1.3 to vanish at the given temperature. The peak of the derivative of the renormalized Polyakov loop, shown in figure 3.1, was used to determine the crossover temperature of $T_c \approx 187(4)$ MeV [126]. The spread of T_c under variation of the scheme defined by β_0 gives the systematic error, while the statistical error is negligible. The non-vanishing of the Polyakov loop illustrates the lack of a true order parameter in the presence of moderate quark masses which explicitly break the centre symmetry even at zero temperature.

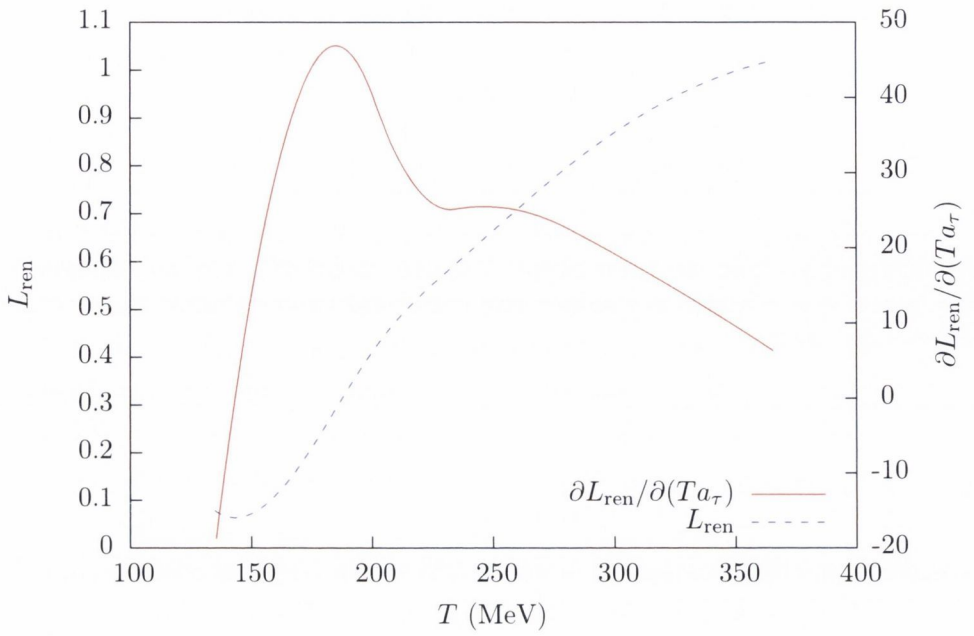

Figure 3.1: A cubic spline interpolation of the renormalized Polyakov loop, $L_{\rm ren}$, (dashed line) and its derivative (solid line) which is used to determine the transition temperature, $T_c \approx 187$ MeV, determined by the FASTSUM collaboration.

3.1.1 QCD spectrum at finite temperature on the lattice

Numerical studies have significant value for the experimental heavy-ion physics community and great investment has been expended in producing reliable simulations suitable for the study of QCD at high temperatures. It is worth noting the work by both the Wuppertal-Budapest collaboration [25] and the HotQCD collaboration [124] in the calculation of the equation of state. These groups have also achieved agreement on the transition temperature at the physical point, $T_c \approx 154$(MeV), after a long-standing discrepancy [130, 4]. Alongside these static observables there have been advances made in providing lattice input for non-perturbative quantities such as the jet-quenching parameter [27] and transport coefficients [125, 131]. The provision of accurate predictions especially for the heavy-ion physics community is a great motivation and challenge for the lattice community in the era of high-precision numerical simulations.

A variety of lattice studies of the spectrum of QCD at finite temperature have been performed which have probed both the deconfinement and chiral crossover transitions. The light meson screening masses are sensitive to the restoration of chiral symmetry through the degeneracy of the vector and axial vector chiral partners. While the $U_{\rm A}(1)$ axial symmetry is always anomalous at the operator

level, the degeneracy of the pseudoscalar and scalar isovector meson masses may signal the *effective* restoration of anomalous axial symmetry [132, 14], defined by the equivalence of correlation functions related by the symmetry. Examining such degeneracies of the spectrum is complemented by analysis of the generalized susceptibilities and, in the case of the axial anomaly, the low-lying modes of a chiral Dirac operator [11]. Some contention still remains regarding the fate of the axial anomaly between calculations using chiral regularizations [133]. Studies of the light meson spectrum also enable the investigation of transport coefficients such as the conductivity of the plasma [125]. Furthermore, the fluctuations of the conserved charges have been used to probe the deconfinement of strangeness and charm where it was observed that charm may become deconfined already above the chiral crossover from cumulants of net-charm or baryon charge even though charmonium states may survive above the deconfinement crossover temperature [29, 134]. Incidentally, discrepancies between the hadron resonance gas and the partial pressures in these studies have provided evidence for highly excited states in the charm sectors predicted by relativistic quark models or lattice QCD which have not yet been experimentally observed [102].

Various studies have probed the deconfined medium using quarkonium, mostly for charmonium, or bottomonium on quenched ensembles, using relativistic quark actions [135, 136, 137, 138]. Most recently, the Bielefeld group has conducted extensive studies of charmonium on quenched ensembles with a systematic discussion of the lattice artifacts, in order to estimate the charm diffusion coefficient and investigate the survival of these states above the crossover temperature [139]. While they observed thermal modifications to the correlators in the deconfined phase, distinguishing the effects due to the change in the spectrum is complicated due to the presence of a zero mode in the associated spectral function. Their analysis of the spectral function using MEM leads them to conclude that no bound states persist above $1.5T_c$. As the method for reconstruction of the spectral function cannot resolve the widths of arbitrarily narrow peaks, they emphasise the criteria for dissociation must be a temperature-dependence of the peak position and relative broadening of the peak. Furthermore, Ohno et al. [140] have also specifically investigated the heavy-quark mass dependence of the quarkonium correlation functions on quenched ensembles above the deconfinement crossover with a relativistic action. Quark masses ranging from charm to bottom were examined and they noted that there is significant mass dependence of the thermal alterations in all but the pseudoscalar channel.

The FASTSUM collaboration have used MEM on dynamical ensembles to investigate the survival and momentum-dependence of the spectral functions for char-

monium [138]. No significant momentum-dependence was observed [95]. The Budapest-Wuppertal collaboration have computed charmonium spectral functions from MEM on fine lattices with $N_f = 2 + 1$ in the Wilson formulation, where no temperature dependence in the pseudoscalar channel at temperatures below approximately $1.3T_c$ was discerned [141]. The modification in the vector channel above the crossover temperature was consistent with the temperature-dependence of the zero-mode and no change in the bound states. These studies have demonstrated how detailed investigations of the spectrum of QCD can provide insights into the phases and symmetry of QCD.

3.1.2 Bottomonium in lattice studies

Early pioneering analyses of heavy quarkonium [142] used a non-relativistic formulation for the heavy-quark on quenched ensembles. The quenching of quarks in the Euclidean theory breaks reflection positivity, and unitarity of the analytic continuation of that theory is lost. Nevertheless, quenched lattice calculations have been used extensively in zero-temperature and finite-temperature studies despite the uncontrolled approximation it introduces. The interpretation of the quenching at finite temperature is the omission of the relevant fermionic degrees of freedom from the thermal heat bath. At the temperatures relevant to lattice studies around the deconfinement crossover, the light fermionic degrees of freedom are thermally active and play an important role in the nature of the transition itself.

The quenching of the charm and bottom quark, however, is justified in the thermal context as there is a reasonable scale separation between the temperature and the heavy-quark mass. In particular, the heavy quark is not in thermal equilibrium with the medium of light degrees of freedom at the accessible temperatures. Essentially, then, what is included in the simulation is the thermal dynamics of the medium which affects the binding of the heavy quarks, whose own dynamics are not thermalized. Furthermore, it may be worth reiterating that essentially the modification of the heavy-quarkonium spectrum in a bath of thermal light gluons and quarks is being investigated. This set-up provides the correct equilibrium input for modelling the non-thermalized heavy quark in a deconfined plasma [143]. The fact that the heavy quark is not thermalized in fact is advantageous both in the interpretation of the modification of the hadronic correlation functions at finite temperature and in the inversion of the spectral function representation of the hadronic correlation function.

Previous studies of the spectrum using this set-up have been employed by the FASTSUM collaboration with $N_f = 2$ flavours of light dynamical quark [95,

93, 96, 144]. However, it is desirable to include the strange quark dynamically at temperatures of the order of the deconfinement temperature to make contact with physical QCD. Furthermore, these exploratory studies were completed on rather coarse lattices without an improved fermion discretization in the temporal direction. Although these comprise significant changes to the physics and implementation, the analysis of the correlation functions does not indicate any significant changes in the interpretation from the earlier studies due to the inclusion of extra light degrees of freedom.

The analysis of the quarkonium correlation functions in the $N_f = 2$ study suggested the survival of the S wave ground-state above the crossover temperature up to the highest accessible temperature of $\sim 2T_c$, as little temperature dependence was observed [145]. However, significant modification of the correlation function directly above the crossover temperature was observed in the P-wave channel and the behaviour of the effective mass and exponent, defined in eqn. (3.9), were consistent with the signature of unbound quarks. The subsequent computation of the spectral functions in both channels with MEM gave further evidence for the survival of the S wave in the deconfined phase and for the dissolution of the P wave states almost directly above T_c [94, 96]. More recently studies have also been initiated with $N_f = 2 + 1$ flavours of dynamical HISQ fermions and a comparable set-up for the heavy quark action [128]. A systematic comparison of the results will be useful to ascertain the discretization effects which is the leading source of unquantified systematic uncertainty present in these calculations owing to the lack of any continuum extrapolation.

3.2 Free quarks on the lattice

Once the binding of the heavy quarks is effectively screened by the medium, there is no possibility of the survival of the bound state regardless of the appropriateness of the effective description. The goal of lattice studies is to uncover evidence for free behaviour should it exist. In order to compare the correlation functions with the case of free heavy quarks, the spectral functions, which were given for the continuum case in chapter 1, are presented here for a discrete lattice.

Obviously, lattice artifacts play a significant role in the short-distance part of the correlator, or high-energy part of the spectral function, and must be taken into account when comparing interacting and non-interacting spectral functions and correlation functions. Free lattice spectral functions have been investigated for relativistic quark actions extensively [146, 147]. The free lattice correlation function can be computed either by constructing the free lattice spectral function

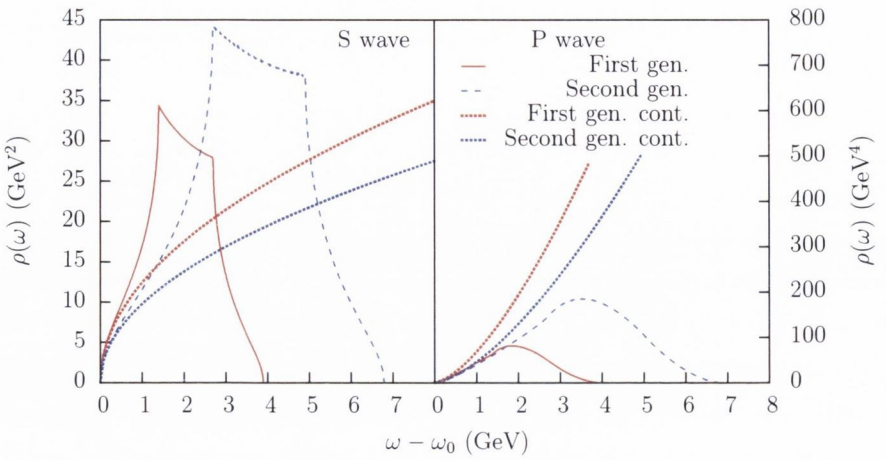

Figure 3.2: Free lattice spectral functions in the S wave (left) and P wave (right) channels computed using equation eqn. (3.3). The spectral functions are computed with the relevant parameters for the $N_f = 2$ (red) and $N_f = 2 + 1$ study, which demonstrates the effect of the reduction of the lattice spacing in increasing the support of the spectral function.

explicitly as outlined below, and composing with the kernel, eqn.(2.44), or can be calculated directly using the same evolution equation used in the interacting case and simply omitting the interaction terms. The free lattice spectral function is calculated according to the following sum over all allowed lattice momenta which are in the first Brillouin zone (1BZ) [147]:

$$a_s^2 \rho_{\mathrm{S}}(\omega) = \frac{4\pi N_c}{\xi N_s^3} \sum_{\mathbf{n}\in 1\mathrm{BZ}} \delta(a_\tau \omega - 2a_\tau E(\mathbf{n})), \tag{3.2}$$

$$a_s^4 \rho_{\mathrm{P}}(\omega) = \frac{4\pi N_c}{\xi N_s^3} \sum_{\mathbf{n}\in 1\mathrm{BZ}} \hat{k}^2 \delta(a_\tau \omega - 2a_\tau E(\mathbf{n})). \tag{3.3}$$

where the lattice dispersion relation corresponding to the improved NRQCD action is given by

$$\begin{aligned} a_\tau E(\mathbf{n}) = &-2\log\left(1 - \frac{1}{2}\frac{\hat{p}^2}{2\xi a_s m_Q}\right) \\ &- \log\left(1 - \frac{\hat{p}^4}{24 a_s m_Q \xi} + \left(1 + \frac{a_s m_Q}{2\xi}\right)\frac{(\hat{p}^2)^2}{8\xi (a_s m_Q)^3}\right) \end{aligned} \tag{3.4}$$

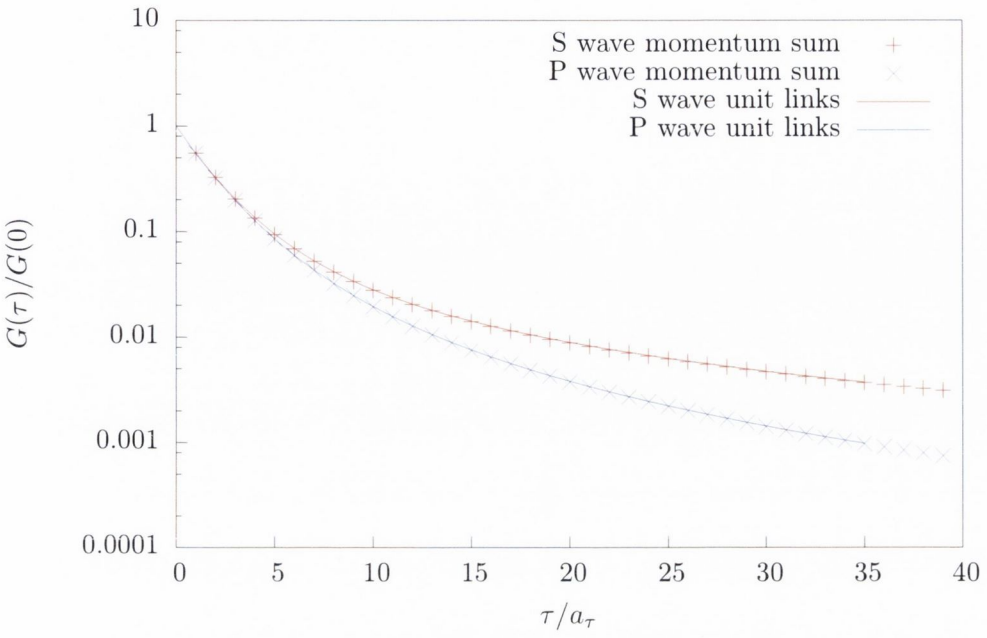

Figure 3.3: Comparison between free lattice correlator in the S wave (red) and P wave (blue) channels, computed using the momentum sum (solid lines), eqn. 3.3, and the NRQCD evolution equation (points) with interactions omitted by omitting the gauge fields.

and the lattice momenta are defined by

$$\hat{p}^2 = 4\sum_{i=3}^{3} \sin^2\left(\frac{\pi n_i}{N_s}\right), \quad \hat{p}^4 = 16\sum_{i=3}^{3} \sin^4\left(\frac{\pi n_i}{N_s}\right), \tag{3.5}$$

$$\hat{k}^2 = \sum_{i=1}^{3} \sin^2\left(\frac{2\pi n_i}{N_s}\right), \quad n_i = -\frac{N_s}{2}, \ldots, \frac{N_s}{2} - 1 \tag{3.6}$$

Note that the momentum insertion in the P wave channel spectral function, due to the derivative coupling in the associated operator, is chosen to correspond to the symmetric derivative used in the lattice operator, see table 2.3.

The free lattice spectral function is shown in figure 3.2 in the S wave (left) and P wave (right) channels in the large volume limit, together with the free continuum spectral functions which are ignorant of the cutoff. In the limit of large spatial volume the sum of Dirac distributions converges to a piecewise smooth function with compact support on the frequency domain. The cutoff provided by the lattice spacing determines this finite interval according to the free lattice dispersion relation of eqn. 3.4. Deviations between the lattice and continuum free spectral functions must occur at least at energies corresponding to momenta at

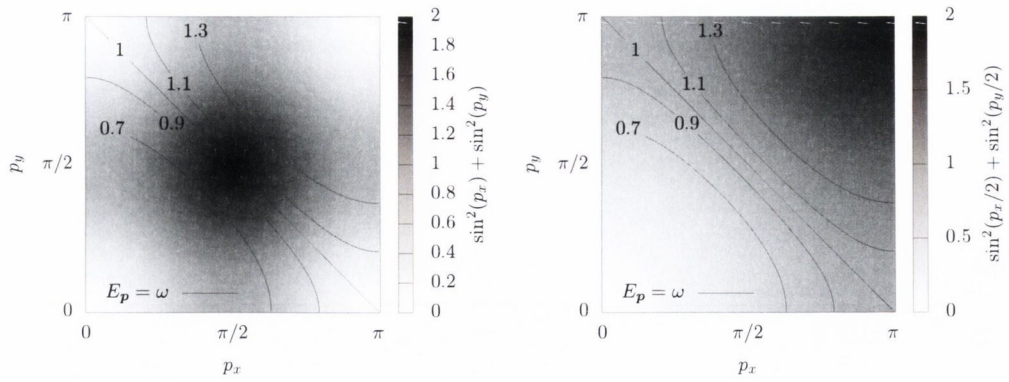

Figure 3.4: Illustration of the value of $\hat{k}^2$ (left) and $\hat{p}^2$ (right) over the reduced Brillouin zone denoted by the shading. The contours depict the level sets of $E(\mathbf{p})$ whose volume changes discontinuously around the value $E(\mathbf{p}) = 1$ and gives rise to the cusps in figure 3.2 in the S wave channel. In the P wave channel, derivative coupling in the lattice operator corresponds to the weight $\hat{k}^2$ (left) which suppresses these cusps. If the operator instead coupled with the ordinary lattice momentum, $\hat{p}^2$ (right), these cusps would not be suppressed.

the corners of the finite Brillouin zone. The cusps in the S wave spectral function are a consequence of the geometry of the Brillouin zone as the volume of the level surface, $\omega = E(\mathbf{n})$, changes discontinuously around energies corresponding to momenta at the corners of the Brillouin zone. Figure 3.4 illustrates a two-dimensional model which can explain the puzzling absence of cusps in the P wave channel as follows. The contours in figure 3.4 correspond to level surfaces of the energy,

$$\omega = E(\mathbf{p}) = \sin^2(p_x/2) + \sin^2(p_y/2), \quad \text{with} \quad p_i \in [0, \pi) \tag{3.7}$$

which is analogous to the leading term quadratic in the lattice momentum in the lattice dispersion relation. The spectral function is the volume of this level surface, with constant weight in the S wave channel or with weight $\sin^2 p_x + \sin^2 p_y$ in the P wave channel. The smoothing effect of the P wave momentum insertion of $\hat{k}^2$ in the sum can be understood from the left-hand panel of figure 3.4 which illustrates the weight of the momentum over the Brillouin zone with shading. The weight in the P wave channel suppresses the contribution to the volume of the level surface from the corners of the Brillouin zone in the light regions of figure 3.4 (left). If the momentum insertion in the P wave channel spectral function is replaced with the usual definition of the lattice momentum, $\hat{p}^2$, figure 3.4 (right), sharp cusps would also be observed in that channel.

Examining the large volume limit of the free lattice spectral function is satis-

factory for the purposes of comparing with the reconstructed spectra. The finite lattice spacing is more pertinent to constrain the gross features of the spectral function such as its support on the frequency domain. In any case, the regularizations favour smooth reconstructions of the envelope of the free lattice spectral function. The correlation functions obtained by taking the integral, eqn. 2.44, of the free lattice spectral functions given in eqn. (3.3), are depicted in figure 3.3, along with the correlation functions obtained from the free evolution equation by omitting the gauge fields. Both correlation functions agree even though the evolution equation is computed using a comparatively small volume of the usual lattice size to the momentum sum which is calculated with $N_s = 2000$.

Some difficulty is introduced by the energy shift in the simulated interacting theory which appears after the renormalization of the rest energy in NRQCD. The NRQCD energy then contains a contribution from the heavy-quark self-energy. This was removed in the zero-temperature study by comparing with the experimental $\Upsilon(^3\mathrm{S}_1)$ energy. This a priori unknown shift hinders the comparison between the interacting correlation functions at finite temperature and the free lattice correlation functions whose threshold corresponds to the two-quark threshold.

Ideally, this effect of this energy shift would be removed exactly by shifting the interacting spectral function accordingly, or correspondingly multiplying the correlation function by the exponential factor of eqn. (1.33). This energy shift may be studied perturbatively due to the high scale of the lattice cutoff. The relevant perturbative calculation of the heavy-quark self-energy for leading-order NRQCD was performed in ref. [55]. An estimate for the additive shift can be obtained from these results for the unimproved NRQCD action which gives $a_\tau \omega_0 \approx 0.16$ using the closest available parameters to those used in this study of an anisotropy of $\xi = 4$ and bare quark mass of $a_s m_Q = 2.5$. In principle, the self-energy contribution could also be estimated for the improved action used in this work using the tools of automated perturbation theory ref. [148].

3.3 Thermal modification of the correlation functions

Results from the $\Upsilon(^3\mathrm{S}_1)$ and $\chi_{b1}(^3\mathrm{P}_1)$ channels at finite temperature are presented in this section. These channels are representative of the qualitative behaviour of the other S wave and P wave channels due to the fact that the gross structure is characterized by the multiplets of orbital angular momentum. The hyperfine structure, being suppressed in the effective theory, does not alter the most significant qualitative behaviour, so reference is made only to the S wave and P wave

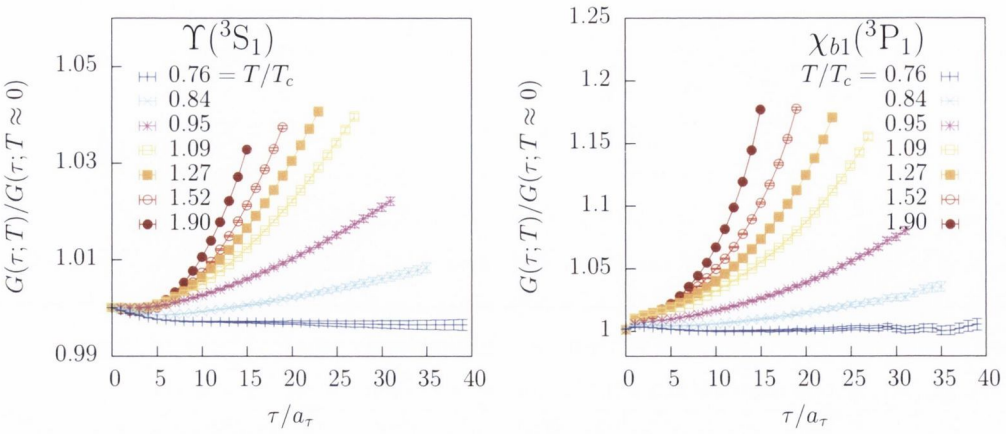

Figure 3.5: Ratio of correlation functions at finite temperature to those at zero temperature in the S wave (left) and P wave (right) channels at temperatures ranging from $0.76T_c$ to $1.90T_c$.

channels in the following.

In this part of the study only local unsmeared operators are used. Care must be taken not to use operators which have stronger overlap with thermal states than their counterparts in the vacuum. This could introduce an enhancement of the spectral weight with increasing temperature and confuse the interpretation of the thermal modification of the spectrum. The variational method has been applied to operators used in the analysis of the spectral functions, but the foundation for applying the method at finite temperature is not well understood [149]. It is not clear at which temperature the optimization of the operators should be performed. Furthermore, the relation between the dilepton production rate and the spectral function in the vector channel, eqn. (1.5), holds only for a local operator.

Figure 3.5 shows the ratio of the correlation functions at finite temperature to those at zero temperature in the S wave (left) and P wave (right) channels. The hadronic correlation functions in NRQCD receive no contributions from zero mode spectral features which would give rise to a τ-independent contribution to the correlation function [150]. These features which pertain to transport coefficients through the Kubo formulae are obviously absent from the effective theory around the two-quark threshold. Furthermore, because the b-quark is not in equilibrium with the medium, all temperature modifications of the correlation functions are related to the temperature-dependence of the spectral function because the integral kernel in eqn. (2.44) is temperature-independent.

An enhancement is clearly observed in both channels at comparable Euclidean

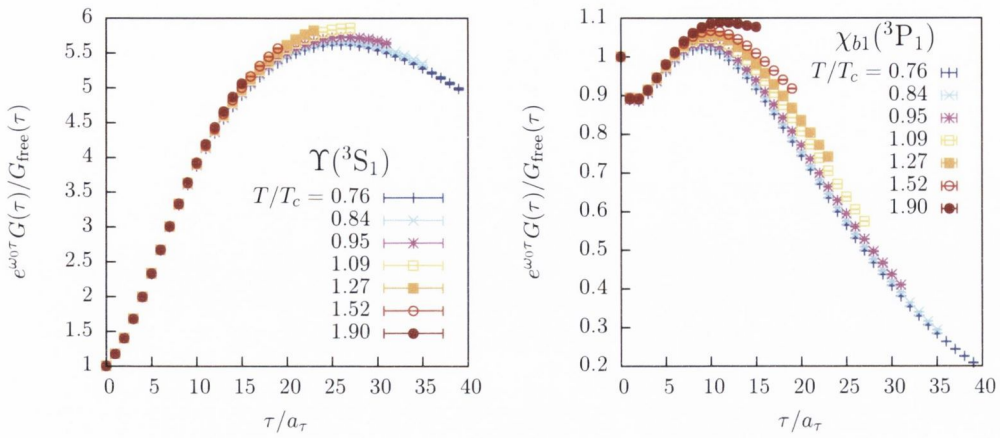

Figure 3.6: Ratio of correlation functions at finite temperature to free lattice correlation functions in the S wave (left) and P wave (right) channels at temperatures ranging from $0.76T_c$ to $1.90T_c$.

temporal separations as the temperature is increased. Note that the relevant comparison is between the ratios at the same Euclidean distance in physical units rather than, say, scaled by the temperature because of the temperature-independence of the kernel. The correlation functions at the highest temperature are enhanced by a few percent relative to the zero temperature ones in the S wave channel and on the order of ten per cent in the P wave channel. This already suggests a qualitative difference between the two cases. In terms of the redistribution of the spectral weight at finite temperature, an enhancement could be effected by a broadening of the ground state peak or a reduction in the threshold of the spectral function in the absence of bound states. Similar enhancements were observed in the $N_f = 2$ study of the FASTSUM collaboration [93] and in relativistic charmonium studies [138].

The comparison of the correlation functions with the free lattice correlation functions including the shift $a_\tau\omega_0 \approx 0.16$ is shown in figure 3.6 in the S wave (left) and P wave (right) channels. In the S wave channel, large deviations from the free correlator are observed at all temperatures. While some slight temperature dependence at intermediate temperatures, the dependence is not as significant as in the P wave channel. The correlator in the P wave channel displays a trend towards the free lattice correlator as the temperature is increased, just overshooting it at the highest accessible temperature, indicating quasi-free behaviour.

However, it must be noted that the resulting dependence on the energy shift of the ratios between the interacting and free lattice correlation functions is not mild and the results must be considered suggestive at best. This systematic issue

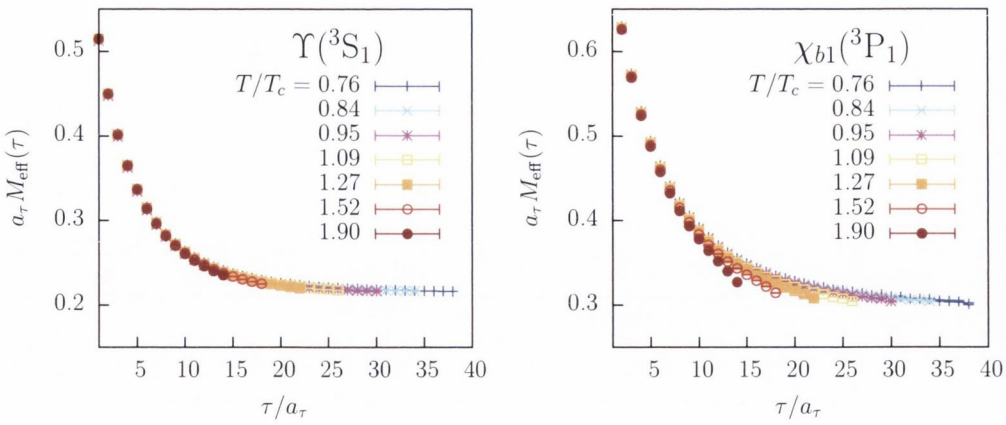

Figure 3.7: Temperature-dependence of the effective mass, $m_{\rm eff}$, in the S wave (left) and P wave (right) channels from $0.76T_c$ to $1.90T_c$.

highlights the problematic nature of accounting for the threshold in the comparison between interacting and free observables and motivates the investigation of the spectral function as the observable of choice to interpret the medium modification.

It is useful to examine two other observables in order to probe the temperature dependence. Given the free continuum form of the hadronic correlation function of eqn. (1.32) the effective mass no longer displays a plateau in the absence of a threshold but instead decays with a power-law at asymptotically large Euclidean distance. The presence of a finite threshold, eqn. (1.33), modifies this behaviour to a power-law decay to a finite constant value,

$$m_{\rm eff}(\tau) = -\frac{1}{G(\tau)}\frac{\mathrm{d}G(\tau)}{\mathrm{d}\tau} \overset{G=G_{\rm free}}{=} \omega_0 + \frac{\alpha+1}{\tau}. \tag{3.8}$$

Nevertheless, the transition from a plateau in the presence of a bound state to a power-law decay to a lower plateau at the energy shift may still be visible if the free behaviour begins to set in within the temperatures investigated and the energy shift is sufficiently separated from the bound state energy. In figure 3.7 the qualitative difference between the S wave (left) and P wave (right) channels is again illustrated by the effective mass. Little temperature dependence is visible in S wave channel which approaches a plateau at all temperatures while the P wave channel shows some deviation from the low-temperature behaviour.

Based on the algebraic decay of the hadronic correlation function for free quarks in the continuum, eqn. (1.33), it is useful to introduce a new observable,

the effective exponent

$$\gamma_{\text{eff}} = -\frac{\tau}{G(\tau)}\frac{\mathrm{d}G(\tau)}{\mathrm{d}\tau} \overset{G=G_{\text{free}}}{=} \omega_0\tau + \alpha + 1. \tag{3.9}$$

In the absence of interactions this observable is equal to the exponent of the algebraic decay of the correlation function, $\alpha + 1$, if the threshold vanishes. If the threshold is removed from zero then it also contains a linear piece with slope equal to the threshold, while if there is no algebraic part then the constant piece vanishes and its intercept is at zero.

The temperature-dependence of the effective exponent is shown in figure 3.8 in the S wave (left) and P wave (right) channels with the perturbative estimate for the contribution from the energy shift subtracted away. At low temperatures the effective exponent at large Euclidean time is linear with a small intercept and positive slope which encodes the bound state energies in each channel. Little temperature-dependence is observed in the S wave channel as expected from the correlator and effective mass, and the observable does not coincide with the free effective exponent except at the earliest temporal separations. In the P wave channel at the highest accessible temperatures there is some clear deviation from the low-temperature behaviour and there is a tendency toward the free lattice effective exponent as the temperature is increased. If the threshold effect is not removed then this linear rise persists at all temperatures and it is difficult to compare with the free lattice effective exponent. A similar behaviour was observed in the P wave channel in the $N_f = 2$ study [93] without subtracting the threshold, due to the smaller value of the energy shift. The different renormalization pattern results from the different discretization in the earlier study.

The quality of fits to the free continuum form of the correlator, eqn. (1.33), are poor even at high temperatures in the P wave channel when the qualitative

T/T_c	τ_1/a_τ	τ_2/a_τ	α	ω_0	χ^2/d.o.f.
0.76	26	38	0.030(55)	0.2806(19)	1.2
0.84	25	34	0.317(57)	0.2694(21)	0.4
0.95	20	30	0.354(23)	0.2648(10)	1.2
1.09	18	26	0.540(17)	0.2517(09)	0.6
1.27	16	22	0.703(14)	0.2384(08)	2.7
1.52	13	18	0.850(09)	0.2221(07)	19
1.90	10	14	0.909(05)	0.2071(05)	158

Table 3.2: Best fit parameters for the linear fit to the effective exponent, γ_{eff}, in the P wave channel. The quality of the fit is poor at high temperatures where the asymptotic linear form only begins to set in.

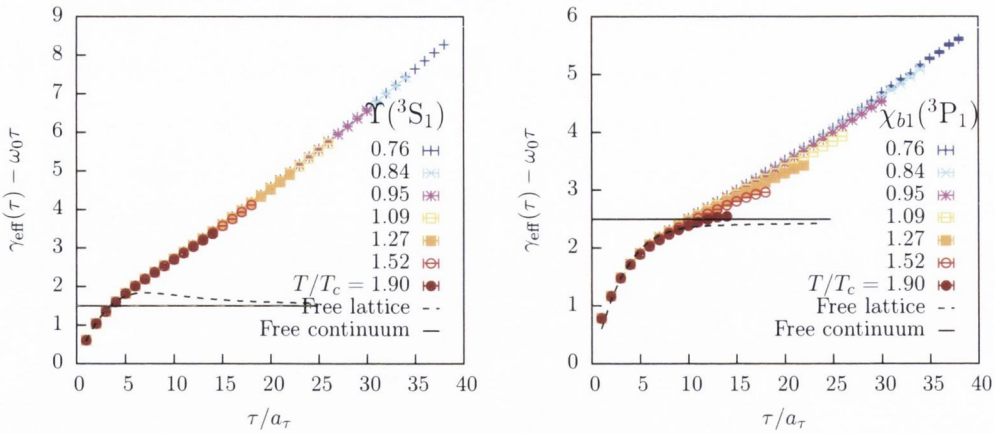

Figure 3.8: Temperature-dependence of the effective exponent, $\gamma_{\rm eff}$, in the S wave (left) and P wave (right) channels from $0.76T_c$ to $1.90T_c$.

change in the effective mass and exponent suggests that quasi-free behaviour may set in. This could be due to the difficulty of performing such a delicate non-linear fit with the mixed exponential and power-law decay, as well as the inadequacy of the continuum form to model the correlator.

Instead, linear fits directly to the effective exponent were attempted. In the P wave channel the fits were stable under variations of the bottom window of the temporal range, τ_1/a_τ, within a few units, at all but the two highest temperatures. At these high temperatures the asymptotic linear form of the exponent only just sets in at the latest accessible times. The best fit parameters in the P wave channel, shown in table 3.2, indicate that the effective exponent increases with temperature towards the free continuum value, $\alpha = 1.5$ but does not attain it within the temperatures investigated. Also, the slope corresponding to the threshold decreases toward the perturbative estimate of the energy shift, $a_\tau\omega_0 \approx 0.16$, with increasing temperature. The higher statistical precision of the effective exponent in the S wave channel spoils the goodness of fit and suggests that the continuum algebraic form is not an adequate model at any temperature.

The tentative conclusion from the analysis of the correlation functions and derived observables is the greater temperature-dependence in the P wave channel with qualitative behaviour which is consistent with quasi-free heavy quarks above the crossover temperature. This establishes qualitative agreement of the modification of the spectrum with earlier $N_f = 2$ studies [93, 94]. However, for consistency, the effect of a larger energy shift in this study must be taken into account. Although the spatial lattice spacing is reduced in this study compared with the $N_f = 2$ study, the temporal lattice spacing is larger and the change in the

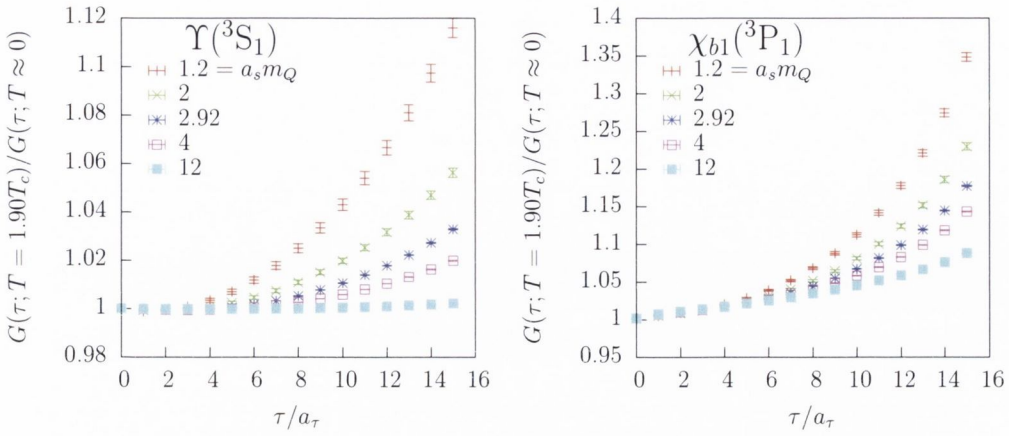

Figure 3.9: Mass-dependence of the ratio of the correlation functions in the S wave (left) and P wave (right) channels at the highest temperature, $1.90T_c$, to zero-temperature. The quark masses range from above the charm quark mass through the bottom quark mass to superheavy.

renormalization of the energy shift is not easily understood. As analytic expressions are not available for the free lattice observables, and as comparisons with the interacting lattice quantities suffers from the ambiguity in the energy shift, the direct evaluation of the spectral functions at finite temperature is desirable.

3.3.1 Mass dependence

There is obviously no technical restriction on deforming the theory under investigation away from QCD. On the lattice for example, quark masses may be tuned away from their values corresponding to the physical quark masses. It is useful to compare the mass-dependence of the quarkonium spectrum above the deconfinement transition to make contact with the expected thermal modification of the spectrum from a simple potential model picture, as has been performed in quenched studies [140]. The binding radius is related to the typical inverse momentum transfer, $r_H \sim (m_Q v)^{-1}$, and effective colour Debye screening occurs when the screening length, r_D, is comparable with or smaller than the binding radius, $r_D \lesssim r_H$. At a given temperature, therefore, such a mechanism is expected to become less effective for heavier, more tightly bound states.

Figure 3.9 shows the modification of correlators for various lattice heavy-quark masses ranging from above the charm quark mass through the bottom quark mass to superheavy quarks in the S wave (left) and P wave (right) channels at the highest temperature $1.90T_c$. Correlators in the P wave channel exhibit greater thermal modification than in the S wave channel at each of the lattice heavy-quark

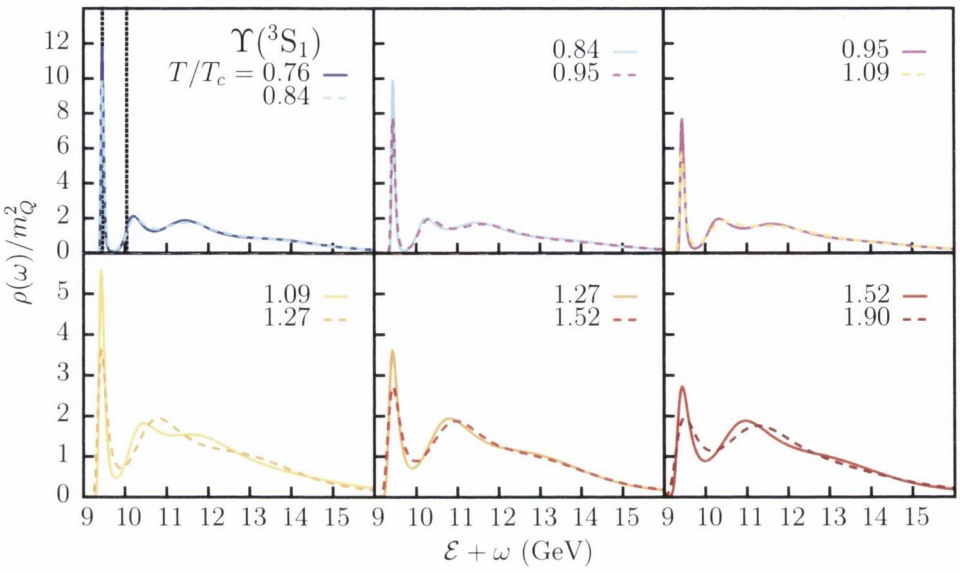

Figure 3.10: Temperature-dependence of the reconstructed spectral function in the S wave channel. The dashed black lines in the first panel indicate the ground state and first excited state energies determined from multi-exponential fits at zero temperature. Note the different ordinate scale between the upper and lower panels.

masses investigated. At smaller values of the heavy-quark mass, approaching the charm-quark mass, on the edge of the validity of the effective theory, a large enhancement is seen even in the S wave channel correlation function, while for large values of the heavy-quark mass some enhancements are still seen in the P wave channel. The mass-dependence has also been investigated in the $N_f = 2$ case [151] where analogous dependence on the heavy-quark mass parameter was observed.

3.4 Spectral functions from MEM

As motivated in the previous section, the spectral functions provide a straightforward interpretation of the modification of the spectrum at finite temperature. In this section, the spectral functions from MEM are presented using the methodology outlined in the previous chapter. Systematic effects are discussed in the following subsection, of which the stability of the reconstruction with the variation of the time domain of the correlator data used is the most important.

Figures 3.10 and 3.11 depict the spectral functions in the S wave and P wave

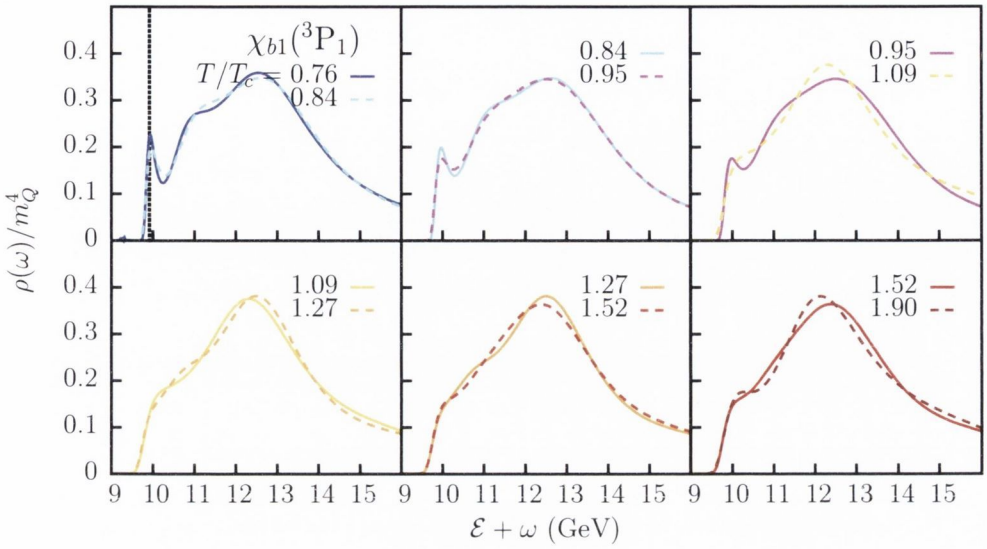

Figure 3.11: Temperature-dependence of the reconstructed spectral function in the P wave channel with the zero temperature ground state energy shown in the first panel with a dashed black line. Recall that no excited states were able to be extracted in the P wave channel using multi-exponential fits.

channels respectively at temperatures from $0.76T_c$ up to $1.90T_c$. For clarity each panel displays just two neighbouring temperatures. In the S wave channel the ground state peak is clearly visible and coincides with the energy extracted from the exponential fit to the correlation function at zero temperature, see figure 2.12. The ground state peak persists at all accessible temperatures demonstrating the survival of the ground state to at least $1.90T_c$. The ground state peak is observed to broaden and decrease in height above the crossover temperature. Below the deconfinement transition the second peak may be identified with the first excited state. Its interpretation above T_c is less clear, which may be due to dissociation in the plasma as well as the possible dominance of lattice artifacts in the high frequency part of the spectral function.

In the P wave channel, shown in figure 3.11, the ground state peak can be discerned at temperatures below T_c and agrees with the energy from the exponential fit at zero temperature. It is noted that below the crossover temperature the ground-state peak is relatively suppressed to the continuum feature at higher frequencies, which suggests the difficulty in distinguishing this state even at low temperatures due to the admixture of lattice artifacts in the correlation function, compared with the S wave channel. This peak is observed to disappear immediately in the deconfined phase which indicates the dissociation of this state almost

as soon as the deconfined phase is reached.

The conclusions from the MEM of the survival of the S wave state in the plasma up to $1.90T_c$ and the immediate dissociation of the P wave state above T_c are effectively unchanged, then, from the $N_f = 2$ studies [94, 96]. A greater range of temperatures below T_c in the current study allows the P wave ground state to be discerned below T_c. No significant effect is then attributed to the inclusion of the strange quark in the thermal medium.

3.4.1 Systematic tests of MEM

A detailed examination of the reconstruction of the spectral functions is essential to have confidence in the interpretation of effects due to the variation of the temperature. Here, some pertinent issues relating the selection of the temporal range of the correlator and the frequency domain of the spectral function are discussed. Other effects such as the dependence on the default model and the statistical uncertainty have been investigated for similar data from the $N_f = 2$ ensembles [94, 96] where they were noted to have only a mild influence on the qualitative behaviour.

The stability of the spectral function with the variation of the temporal range of the correlation functions used in the reconstruction is shown in figure 3.12 in the S wave (top) and P wave (bottom) panels for two temperatures corresponding to $N_\tau = 28$ (left) and $N_\tau = 20$ (right). The spectral functions are observed to be stable as long as data at temporal separations close to N_τ are excluded. At the higher temperature with $N_\tau = 20$ in the P wave channel (bottom right), a peaked structure appears when the correlator data at $N_\tau - 1$ is included in the reconstruction. It is difficult to understand the resurgence of a peak structure on any physical grounds considering the absence of such a structure in this region of the spectral function at the lower temperature (bottom right). It has been suggested that the periodicity of gauge fields induces a lattice artifact at temporal separations near N_τ which motivates the exclusion of correlator data at separations near the boundary [96].

Alternatively, the peak structure observed in this reconstruction is an artifact due to a ringing effect, like the Gibbs phenomenon in Fourier analysis, when reconstructing rapid thresholds from a finite basis of functions. The instability of the reconstruction under variations of τ_2/a_τ may be a symptom of the fact that the relatively small SVD basis is inadequate to perform large cancellations over the entire support of the spectral function [119]. Regardless, the reconstruction is stable once the last correlator datum is omitted from the reconstruction. Therefore the reconstructed spectral function converges in all cases when the range of

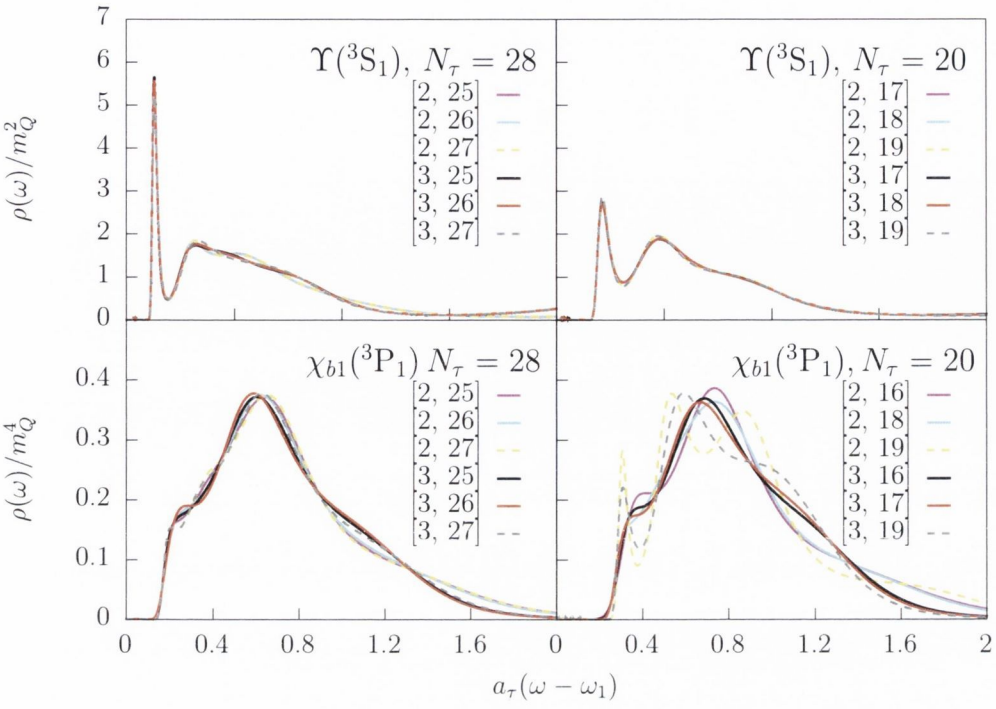

Figure 3.12: Stability of the reconstructed spectral function with respect to selection of temporal correlator data $[\tau_1/a_\tau, \tau_2/a_\tau]$ shown in the key for the Υ (top) and χ_{b1} (bottom) channels, for two temperatures corresponding to $N_\tau = 28$ (left) and $N_\tau = 20$ (right). The results when the largest temporal separation ($\tau/a_\tau = N_\tau - 1$) is included are shown with dashed lines.

correlator data, $[\tau_1/a_\tau, \tau_2/a_\tau]$, is chosen such that $\tau_1/a_\tau > 1$ and $\tau_2/a_\tau < N_\tau - 1$.

More evidence of the stability of the reconstruction is shown in figure 3.13, where only a subset of the available correlator is used to perform the reconstruction in the S wave channel at the lowest temperature with $N_\tau = 40$. In the left-hand panel, the reconstruction is performed using all of the usable correlator data (solid line) and also using only the even correlator data (dashed line), roughly half of the available data. Only a small variation in the ground state peak height is observed. This figure demonstrates that successful reconstructions of narrow peaks may be obtained even with a relatively small number of available basis functions. In the right-hand panel, the reconstruction at the temperature corresponding to $N_\tau = 24$ (dashed line) is compared with the reconstruction at the lower temperature corresponding to $N_\tau = 40$ using the same extent of the correlator data (solid line). This demonstrates the explicit physical effect of the temperature on the spectral function as the conditions of the reconstruction are

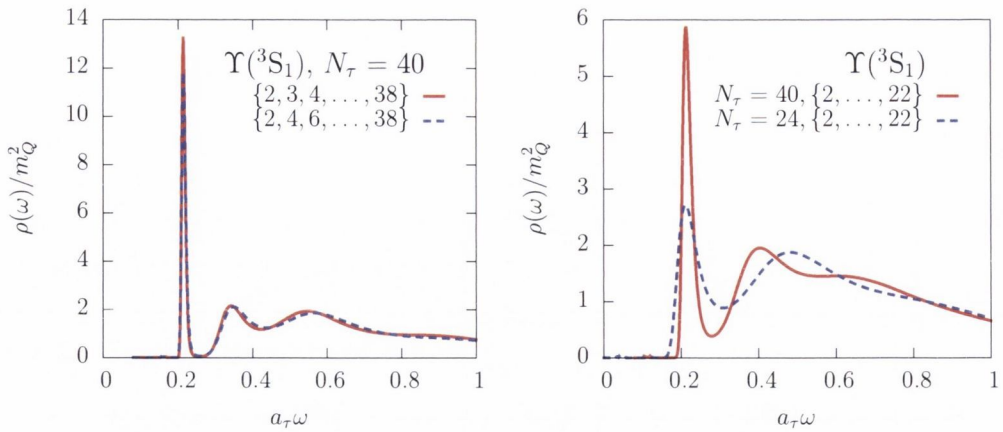

Figure 3.13: Stability of the reconstructed spectral function using all (solid line) and half (dashed line) of the available correlator data in the S wave channel at $N_\tau = 40$ (left). Comparison between reconstructions at $N_\tau = 24$ (dashed line) and $N_\tau = 40$ (solid line) using the same extent of correlator data in both cases (right).

identical in this case. This supports the claim that inferences about the temperature dependence of the spectral function obtained from MEM are physical and not artifacts of the changing SVD basis during the reconstruction.

The frequency domain chosen for each reconstruction of spectral function is given in table A.1. This interval must be chosen judiciously and may extend to negative frequencies due to the fact that the effective theory is defined around the two-quark threshold, so negative frequencies are not excluded a priori. Furthermore, this range must be sufficiently large to avoid forcing spectral weight to redistribute to satisfy the sum rule which conserves its area. Very little variation with the spectral function is observed as long as the frequency range is extended adequately.

The stability of the reconstructed spectral function from the maximum entropy method would lend support that the effects seen both channels are not dominated by artifacts due to the reconstruction and that the results can sensibly provide useful interpretation on the existence and modification of the bound states in the plasma.

3.5 Spectral functions from Bayesian reconstruction

In order to test the robustness of the spectral function reconstructed using MEM it is highly desirable to use the alternative regularization of the BR method outlined in section 2.3.6, especially due to the concerns regarding the reconstruction

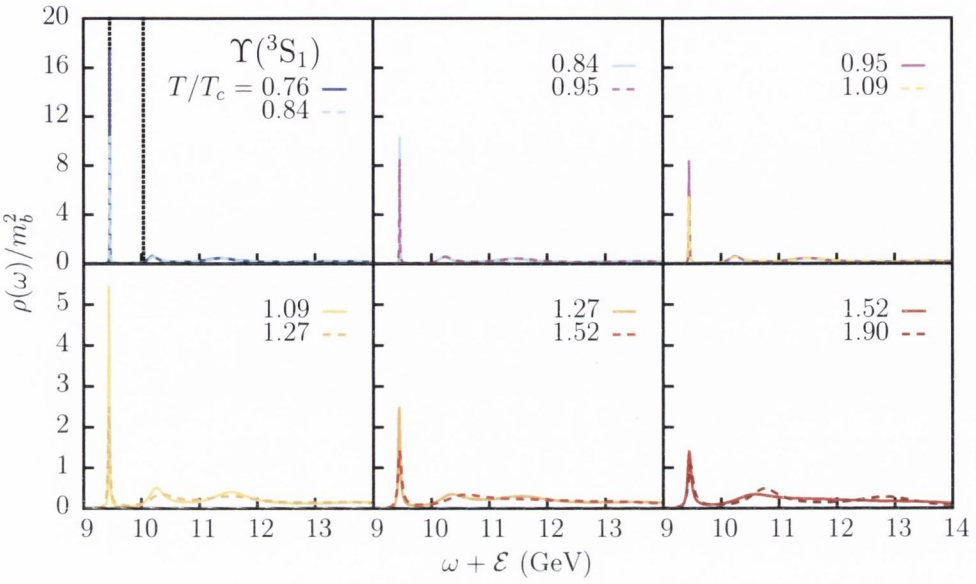

Figure 3.14: Temperature-dependence of the reconstructed spectral function in the S wave channel. The dashed black lines in the first panel indicate the ground state and first excited state energies determined from multi-exponential fits at zero temperature. Note the different ordinate scale between the upper and lower panels.

when there are few correlator data available at high temperatures. Like the MEM, the reconstruction on the finite temperature Euclidean correlator data proceeds identically to the zero-temperature reconstructions. The spectral functions are depicted for the S wave channel in figure 3.14 and the P wave channel in figure 3.15 in the same format as the previous section.

In the S wave channel, at low temperatures, the two lowest peak positions are coincident with the ground and first excited-state energies as before and therefore agree with the peak positions from MEM. At the lowest temperature, the ground-state peak is visibly narrower with a greater amplitude than the MEM spectral function. However, the temperature dependence is very similar with the ground state peak shrinking and broadening with increasing temperature. At low temperatures, the amplitude of the first excited-state peak is relatively reduced and the continuum background feature is much less prominent than in the MEM. As the temperature is increased, the feature of the first excited state shifts and broadens, just as for the MEM, and it is no longer discernible above $1.27T_c$. Qualitatively, therefore, the conclusions of the temperature-dependence in the S wave channel are very similar to those from the MEM although the resolution

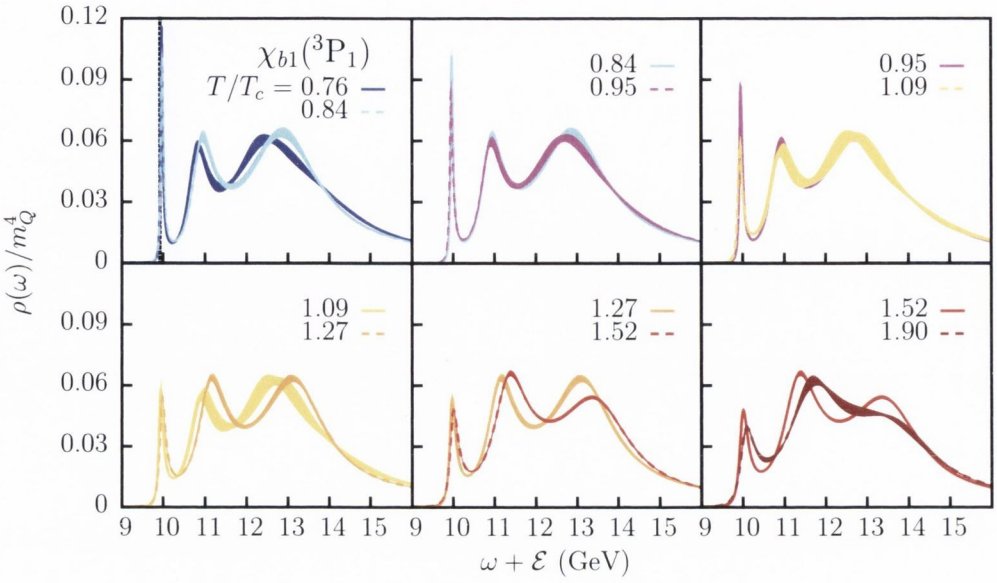

Figure 3.15: Temperature-dependence of the reconstructed spectral function in the P wave channel. The dashed black lines in the first panel indicate the ground state and first excited state energies determined from multi-exponential fits at zero temperature. Note the different ordinate scale between the upper and lower panels.

of the ground state peak at low temperatures seems clearer with the BR method.

In the P wave channel, the situation is markedly different. At low temperatures, the lowest-energy peak agrees well with the ground-state energy, just as for the MEM. The support of the spectral function in this channel is also comparable with the support of the reconstruction from the MEM. However, the background spectral features above the ground-state peak, which are attributed to lattice artifacts, exhibit more peaked structures. In contrast with the MEM the ground-state peak persists at all temperatures up to $1.90T_c$ and exhibits a smaller relative suppression in the peak height as the temperature is increased. This would suggest the survival of the P wave state well into the plasma phase up to at least the highest temperature investigated in this study. In the BR method, the separation between the optimization task and N_τ facilitates the investigation of the dependence of the reconstruction on the number of correlator data. In this context the dependence on the number of correlator data included should demonstrate the physical content of the correlators and not be susceptible to systematic variations of the reconstruction. In the MEM, the dependence of the reconstruction on the number of correlator data is conflated with the N_τ-dependence of the

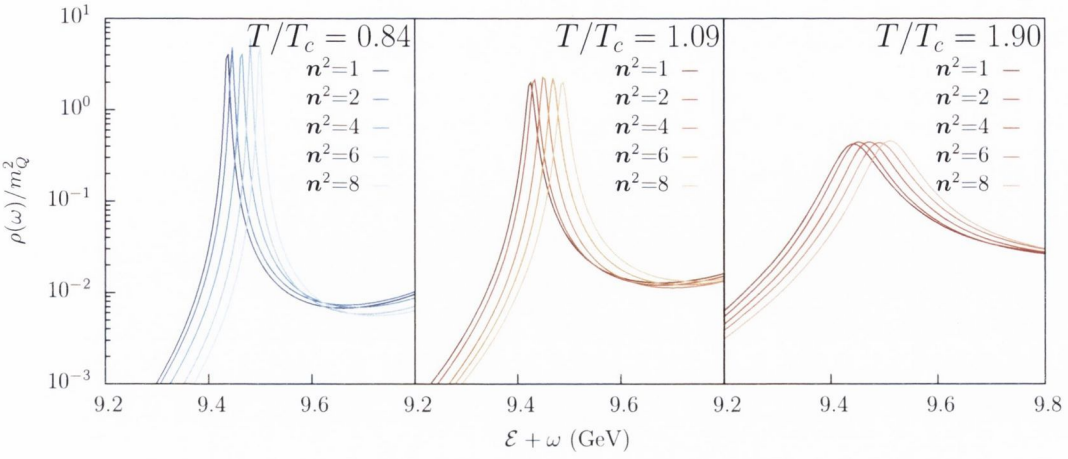

Figure 3.16: Temperature-dependence of the reconstructed spectral functions computed at finite momentum in the S wave channel at temperatures above and below the crossover temperature. No significant change in the momentum-dependence is observed with temperature. Namely, the momentum dependence is characterized only by shift of the peak position according the the dispersion relation (3.4), just as in the vacuum.

SVD basis and consequently it is a more subtle issue to determine the stability of the reconstruction. At finite temperature it is especially important to account for this systematic effect when the number of correlator data is small.

3.5.1 Momentum dependence of the ground-state S wave

In the S wave channel, the spectral function was also reconstructed at finite momentum at temperatures above the transition temperature. A selection of the reconstructions are shown in figure 3.16, where the peak position is observed to scale with the quadratic momentum. No significant variation of the peak width or height is observed as the momentum is increased at any temperature. Only momenta with the same degeneracies are shown for a fair comparison between the the statistical uncertainties, which are however expected to be mild.

3.5.2 Systematics of BR method

In this section, the dependence of the reconstruction on the extent of the correlator data used in the reconstruction is investigated. Specifically, the upper window of the correlator, τ_2, is varied as the primary concern is how the reconstruction depends on the inclusion of the most important correlator data for reconstruction the low-energy behaviour of the spectral functions, namely that at large Euclidean

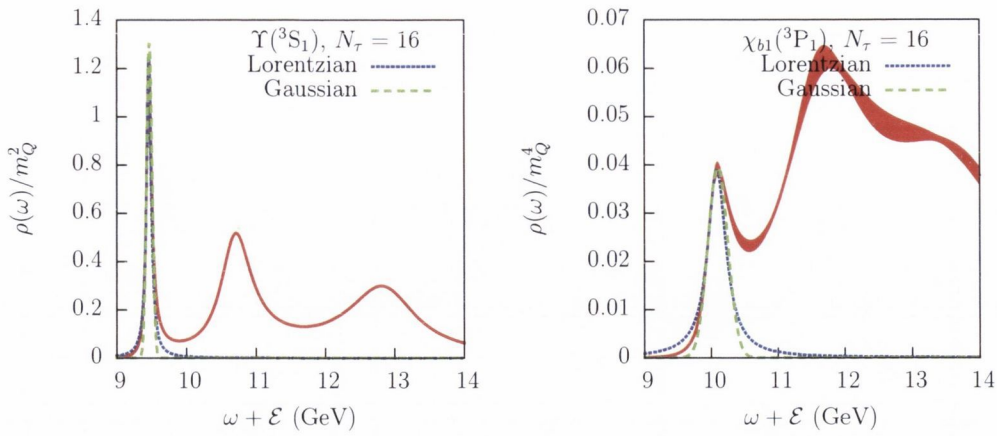

Figure 3.17: Examples of fits of a Lorentzian and Gaussian lineshape to the lowest peak in the spectral function in the S wave (left) and P wave (right) at the highest temperature corresponding to $N_\tau = 16$. The Lorentzian lineshape generally provides a better parameterization judging by the goodness of fit.

distances. In order to quantify the dependence of the ground-state peak on τ_2, the peak feature is fitted with a Lorentzian and Gaussian lineshape, examples of which are depicted in figure 3.17. The fit was performed over only the left-hand lineshape due to the contamination of the ground-state peak with contributions from the background, especially at higher temperatures. Additionally, the peak was fitted only over the region of the spectral function above the half-height of the ground-state peak. The Lorentzian lineshape generally provided a better parameterization of the lineshape motivated on physical grounds, although the Gaussian lineshape was satisfactory for most cases, judging by the goodness of fit. The reconstructions were repeated by varying the latest correlator datum used in the reconstruction, τ_2, and the dependence of the best fit parameters on τ_2 were examined. Although the statistical errors from the jackknife method were estimated in the noisier P wave channel, their magnitude is so much smaller than the systematic variations in the reconstruction that they can be safely ignored in the present analysis.

The dependence of the ground-state width on τ_2 is depicted in the S wave channel (left) and P wave channel (right) in figure 3.18. The abscissa is the inverse, a_τ/τ_2, so that an indication of the behaviour of the parameters if more Euclidean data were available could be ascertained. In the S wave channel, at low temperatures the width decreases rapidly as τ_2 is increased, indicating that the physical width is smaller than the reconstruction with finite data is able to probe. As the temperature is increased above the transition temperature, a plateau is visible at the highest temperatures in the S wave channel. In the P wave channel

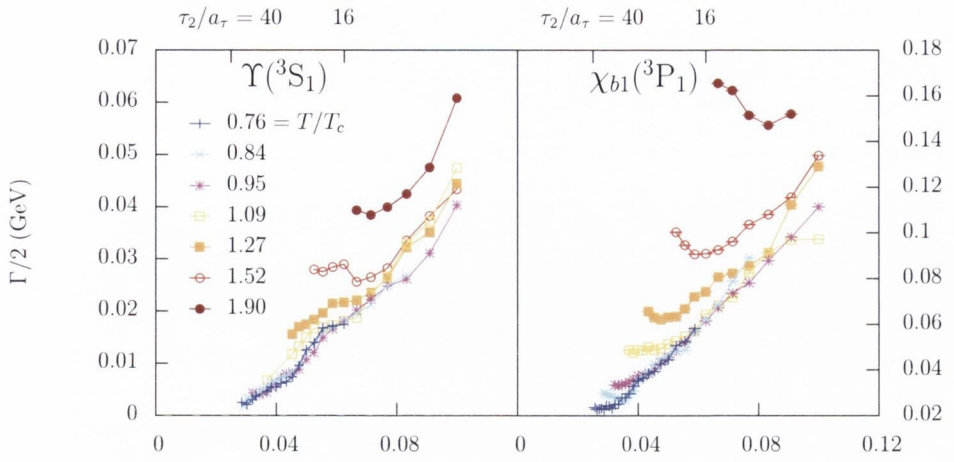

Figure 3.18: Illustration of the best-fit parameter of the width of the ground-state peak, Γ, versus the inverse of the latest correlator datum included in the reconstruction, a_τ/τ_2. Each temperature is depicted in the S wave (left) and P wave (right) channels with linespoints to guide the eye.

similar behaviour is visible except that at all temperatures some stabilizing of the width is visible with the available data is observed. An estimate for the width is then taken to be the width of the spectral feature with $\tau_2/a_\tau = N_\tau - 1$ fore each given temperature. A systematic error is obtained from the variation of the width over the plateau observed as τ_2/a_τ becomes large. For the noisier P wave channel, a statistical error bar is included on these best fit parameters which was estimated from a blocked jackknife analysis. Even this noisier channel, the errors are smaller than the thickness of the points which illustrates that the systematic errors of the reconstruction are much greater than the statistical uncertainty.

The temperature dependence of this estimate for the width from the BR method is shown in figure 3.19. Given the asymptotic behaviour of the width in the S wave channel at low temperatures, a non-zero width is only reported above the transition temperature where some stabilization of the width is observed with τ_2/a_τ. The estimates of the width from MEM in the S wave channel are included, where they are drawn suggestively as upper bounds due to the poorer resolution on the peaked features from this method with the finite SVD basis discussed in the previous chapter. The temperature-dependence of the P wave ground-state width is consistent with a linear rise, although the large systematic error cannot discriminate between a linear or quadratic model.

An analogous plot for the inverse maximum height of the ground-state spectral feature is the S wave (left) and P wave (right) channel is shown in figure 3.20. The ordinate is chosen to be the estimate for the inverse height in order to demon-

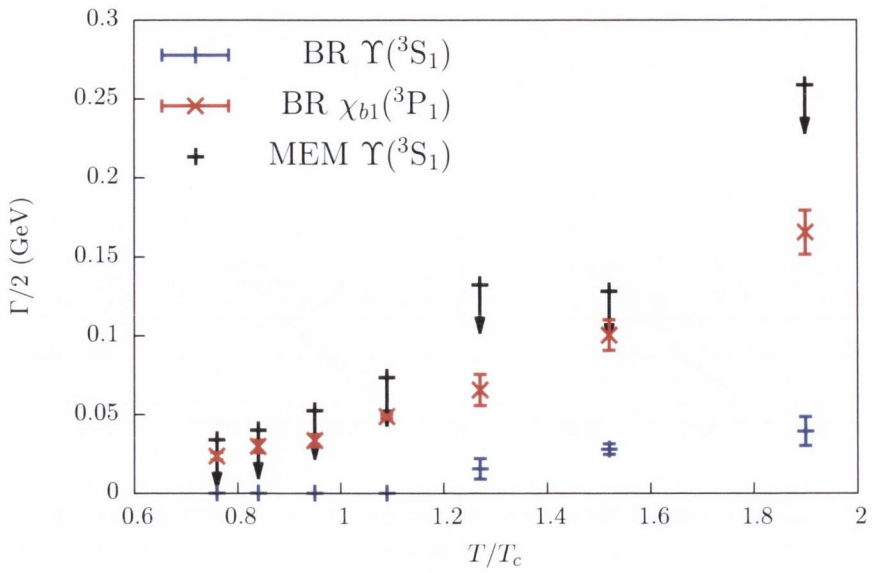

Figure 3.19: Temperature dependence of the ground-state best-fit width from the BR method in the S wave channel (blue crosses) and the P wave channel (red exes). The best-fit width from the MEM reconstruction in the S wave channel is also included with the black arrows which are interpreted as upper bounds due to the difficulty of the method in reconstructing the widths.

strate the extrapolation of the peak height to large values at low temperatures, visible in the S wave channel. As in the case of the width, figure 3.18, a jackknife error is included on the best fit parameters in the P wave channel. Above the transition temperature the heights no longer tend towards very large values suggesting the method is accurately capturing the peak height which is suppressed in the deconfined phase. In the P wave channel some puzzling behaviour can be observed which clearly distinguishes between the behaviour above and below the transition temperature. At low temperatures there appears to be some stability in the peak height as τ_2 is increased while above the deconfinement temperature the reconstructed peak height seems to decrease smoothly as more correlator data are included in the reconstruction. This may suggest that the dominance of lattice artifacts in this channel above the deconfinement transition temperature mean that an adequate reconstruction is poorly constrained by the data where they are not dominated by contributions from physical states, such as in the free case.

The difficulty of reconstructing spectral densities of continuum structures such as the free lattice spectral function is demonstrated in figure 3.21. Here, mock correlator data with $N_\tau = 40$ were created by composing the free lattice spectral

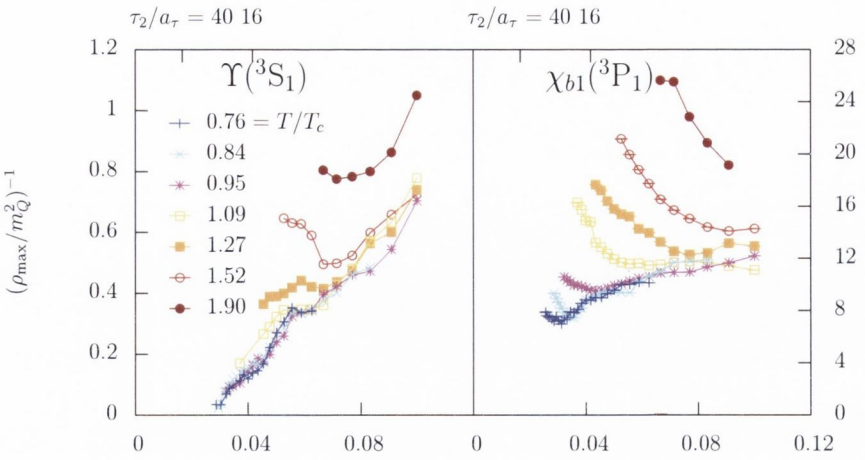

Figure 3.20: Illustration of the best-fit inverse peak height of the ground-state peak, $\rho_{\max}^{-1}$, versus the inverse of the latest correlator datum included in the reconstruction, $a/_\tau/\tau_2$. Each temperature is depicted in the S wave (left) and P wave (right) channels with linespoints to guide the eye.

function, in the S wave channel (left) and the P wave channel (right), with the kernel eqn. (2.44). Gaussian noise was added to the data with a strength corresponding to the signal-to-noise ratio of the available data in the lattice study for a fair comparison. As can be observed in the figure, the method struggles to reproduce the continuum faithfully without the appearance of peaked structures. However, the support of the reconstructed spectral function and the position of the features agrees quite well with the mock data. The area under both densities is scaled to unity for comparison. Ringing phenomena like this is a familiar effect, such the Gibbs effect in Fourier analysis.

In figure 3.22, the reconstructed free lattice spectral function is compared with the reconstructed spectral function from the S wave (left) and P wave (right) channels at the highest temperature. The free reconstruction has been shifted with the energy shift so that its threshold corresponds to the two-particle threshold of the zero-temperature theory. Furthermore it has been scaled with to the area of the high-temperature reconstructed spectral function for comparison.

The comparison of the reconstructed free lattice spectral function with the interacting case is one possible criteria for the survival of the bottomonium states. These criteria are not necessarily ideal and the comparison with the free lattice spectral function which has been suggested in ref. [152] proposes different criteria for matching. There, it is suggested that the free reconstruction be shifted so that the thresholds of interacting and free match and furthermore that the free lattice spectral function is scaled so that the free and interacting thresholds match in

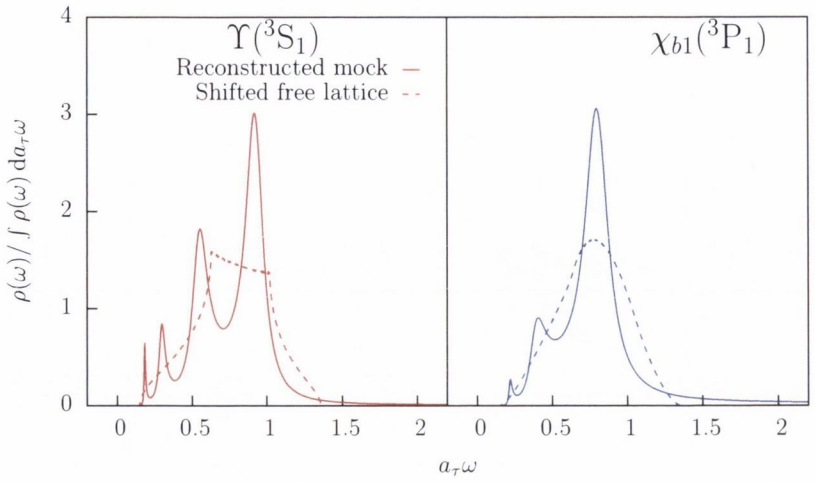

Figure 3.21: Reconstructions of the free lattice spectral function in the S wave (left) and P wave (right) channels from the BR method are shown in solid lines. This demonstrates the difficulty in reproducing features associated with the sharp cusps of the free lattice spectral function (dashed lines). The amplitudes of the spectral functions are normalized by fixing the area underneath them to unity.

the ultraviolet, where only lattice artifacts are present. The ground-state peak in the S wave channel is clearly visible with a large amplitude compared with the scaled free lattice spectral function, unambiguously confirming a signal in this channel. In the P wave channel, right, the relative amplitude of the remnant lowest peak is quite comparable with the amplitude of the free lattice spectral function in that region. Coupled with the curious behaviour of the P wave peak height with τ_2, and the conflict with the MEM results the systematic variation of the reconstruction remains to be resolved.

While the new method offers some advantages in decoupling the SVD basis from the minimization, further investigation of the effects of the different regularization functional will be required to support such discrepancies with existing and tested methods from the MEM. In particular, the information-theoretic grounds for the use of the MEM regularization are not as well understood for the looser ad hoc construction of the Bayesian reconstruction. In practical terms, the new regularization, while suppressing the appearance of unphysical peaks of small amplitude has the opposite effect of a weaker regularization of peaks of large amplitude compared with the prior. It is possible that the instability of the peak height with the number of correlator data is a manifestation of this property of allowing peaked structures to exist unless strongly constrained by the data. The survival of the P wave state in the plasma is not yet settled. The application of

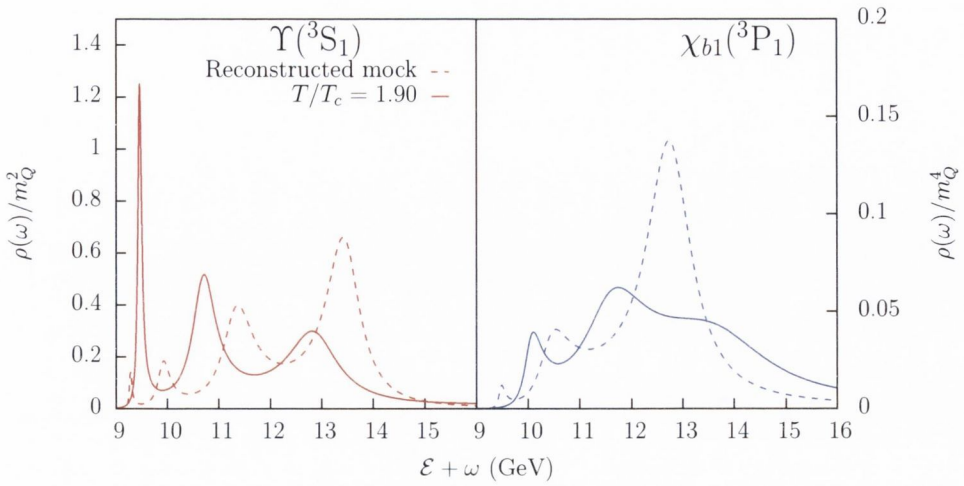

Figure 3.22: Comparison between the reconstructed free spectral function (dashed lines) and the interacting spectral function (solid lines) at the highest available temperature, $1.90T_c$, in the S wave (left) and P wave (right) channels. The area of the reconstructed free lattice spectral function is scaled to the area of the interacting counterpart, and the perturbative estimate of the energy shift is used to shift the threshold of the free lattice spectral functions.

the novel reconstruction method for which it was specifically tailored is outlined in the next chapter in the study of the quarkonium potential from Wilson line correlator data.

4 Heavy-quark potential

In this section another application of the spectral analysis of Euclidean correlators is presented. The determination of the heavy-quark potential at finite temperature can be cast in terms of the inference of the spectral function of a Euclidean Wilson loop. The motivation to understand the binding of heavy quarks in a QCD plasma from the medium-modified potential is closely related to the phenomenology of the in-medium modification of the quarkonium spectral functions presented in the previous chapter. The extraction of the heavy-quark potential suitable for potential models is highly desirable as outlined in the introductory chapter. However, the non-perturbative definition of the heavy-quark potential at finite temperature has been deliberated over for some time and the relevant potential has been identified variously with both the colour-singlet free or internal energies [153, 62]. The following definition of the heavy-quark potential follows from the spectral decomposition of the Wilson loop, or related, the gauge-fixed Wilson line correlators, as outlined in ref. [154]. The two potentials are known to agree only to leading order in resummed perturbation theory — whether they coincide non-pertubatively is not well understood and lattice studies aim to deepen such understanding.

4.1 Heavy-quark potential at finite temperature

The Euclidean Wilson loop is $W_\square(r,\tau) = \mathcal{P}\exp(-\oint_\gamma \mathrm{d}x^\mu\, A^\mu(x))$, where γ is the rectangular path with dimension, $r \times \tau$, and can be shown to have a spectral representation

$$W_\square(r,\tau) = \int \mathrm{d}\omega\, e^{-\omega\tau}\rho_\square(\omega), \tag{4.1}$$

whose analytic continuation satisfies a Schrödinger-like equation [155],

$$i\partial_t W_\square(r,t) = \varphi(t,r) W_\square(r,t). \tag{4.2}$$

Intuitively, this can be understood through the mapping of this operator to the world-line amplitude of a heavy-quark anti-quark pair. The late-time behaviour of this equation defines the heavy-quark potential, $V(r) \equiv \lim_{t\to\infty} \varphi(r,t)$. If a separation of scales exists such that the late-time behaviour dominates the low-energy spectral function, a Lorentzian lineshape encodes the heavy-quark potential through

$$\rho_\square(\omega) = \frac{\Gamma}{(\omega-\tilde{\omega})^2+\Gamma^2}, \tag{4.3}$$

with the identification $\Gamma(r) = \Im V(r)$ and $\tilde{\omega}(r) = \Re V(r)$ [156]. The existence of an imaginary part of the heavy-quark potential can be attributed to Landau damping and was first highlighted in the weak-coupling analyses [53, 56, 157]. The relation of the real and imaginary parts of heavy-quark potential to the Wilson loop spectral function and consequently the Euclidean correlation function invites the non-perturbative estimation of these quantities from the lattice. Pragmatically, the existence of an imaginary part of the potential at finite temperature precludes the accurate extraction of heavy-quark potential from an ansaetz of pure exponential decay of the Euclidean correlator at asymptotically large times [158]. Furthermore, a general analysis of the possible alterations to such a lineshape in the presence of the characteristic timescale, t_{QQ}, which captures the time after which $\varphi(r,t)$ becomes constant reveals that a spectral lineshape

$$\rho_\square(\omega) = \gamma\frac{\alpha(\omega-\tilde{\omega})+\beta|\Gamma|}{(\omega-\tilde{\omega})^2+\Gamma^2} + c_0 + c_1 t_{QQ}(\omega-\tilde{\omega}) + \ldots, \tag{4.4}$$

is possible as an expansion in t_{QQ}, where α,β,γ, c_0 and c_1 are functions of the distance, r. The effect of adding short-distance effects to the Wilson loop naturally skews the Lorentzian lineshape. Improved ansaetz inspired by the skewed Lorentzian form of eqn. (4.4), have been used to estimate the real and imaginary parts of the heavy-quark potential from dynamical lattice simulations [159]. In the following section, the results of the weak-coupling analyses are summarized which suggest a gauge-fixed Wilson-line correlator may provide a more useful observable to extract the potential from numerical simulations.

4.1.1 Heavy-quark potential from Wilson line correlators

The resummed framework of hard-thermal loop effective theory ameliorates the poor convergence in perturbative calculations in thermal field theory [160]. In a physically intuitive picture, this reorganization of perturbation theory shifts the expansion to one around gas of quasiparticles with the Debye mass. The heavy-quark potential was calculated in this formalism in the series of formative works which demonstrated the existence of an imaginary part of the potential as well as the familiar Debye-screened Coulomb part [53, 54, 56]. The imaginary component serves to decorrelate the heavy-quark anti-quark pair in a medium and whose interpretation is due to Landau damping of the binding gluons in the thermal medium. This potential can be derived from the static limit of the heavy quarkonium correlation function, and consequently can be used to determine the resummed quarkonium correlation and spectral functions by solving the Schroedinger equation which is obeyed by the correlation functions, eqn. (1.28), with the potential included.

The analysis of the spectral function in the resummed framework yields exactly the ansaetz of the skewed Lorentzian lineshape of eqn. (4.3) in the low-frequency region around the lowest peak. Furthermore, the numerical evaluation of the spectral function, which cannot be expressed in closed form, demonstrates the necessity of including skewing as well as polynomial terms in order to obtain a good fit and extract the correct potential.

In addition to the dimensionally regularized observable, a momentum regularization of the Wilson loop was imposed in ref. [154]. The non-renormalized Wilson loop, such as the lattice observable in the following study, is heavily suppressed at intermediate Euclidean times partially due to the cusp divergences present. This naturally has practical consequences for a numerical estimation of the Wilson loop if the signal is highly suppressed. The omission of the spatial links is known to produce a significantly improved signal-to-noise ratio in the context of zero-temperature simulations. Consequently, the investigation of the Wilson line correlators in the resummed framework revealed that the identical potential is encoded in the gauge-dependent Wilson line correlators to the same order in the perturbative calculation. Assuming that the same relationship holds non-perturbatively this suggests using the gauge-fixed Wilson-line correlator to extract the potential from numerical simulations.

In the work of ref. [161], MEM was employed to reconstruct the spectral functions from the corresponding perturbative Euclidean correlators in order to demonstrate the feasibility of the reconstruction from Euclidean data. Using the fit form inspired by the skewing of the lowest peak observed in the hard-

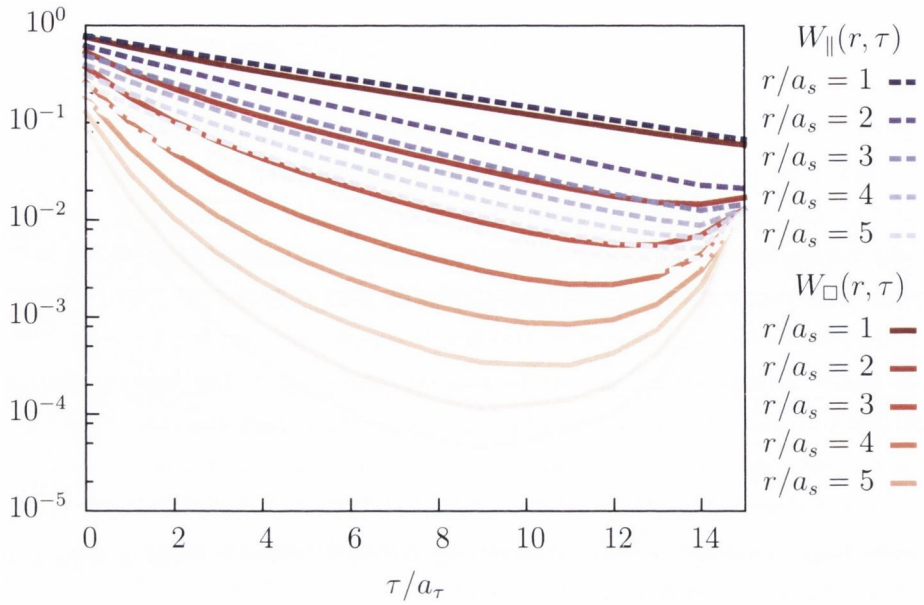

Figure 4.1: A comparison of the Wilson loop, $W_\square(r,\tau)$, (solid lines) and gauge-fixed Wilson line correlators $W_\parallel(r,\tau)$, (dashed lines) at $T/T_c = 1.90$, which demonstrates the large suppression of the Wilson loop signal compared with the gauge-fixed Wilson line at comparable separations, r.

thermal loop approach, it was observed that the real part of the potential was in good agreement with the direct calculation in the perturbative framework. However, the imaginary parts, namely the widths of the reconstructed spectral functions were overestimated. This observation provided the impetus for the Bayesian reconstruction method outlined in the previous chapter. In the following section, the potential from the Wilson line correlators is presented as work done in collaboration with the authors of ref. [120] as part of the FASTSUM+ collaboration.

4.1.2 Wilson line correlators from anisotropic lattices

The advantages of the anisotropic formulation in the performance of the reconstruction ought to provide a valuable opportunity to investigate both the complementary physical content of the Wilson line correlators and to compare the dominant systematic effects of the finite lattice spacing between studies of the heavy-quark potential. The cheap nature of the measurements of the pure gauge observable is somewhat spoiled by the relatively expensive gauge-fixing. The gauge was fixed to Coulomb gauge with a stronger criterion on the gauge-fixing violation of $\theta \leq 10^{-14}$ due to the gauge-dependence of the unclosed Wilson line

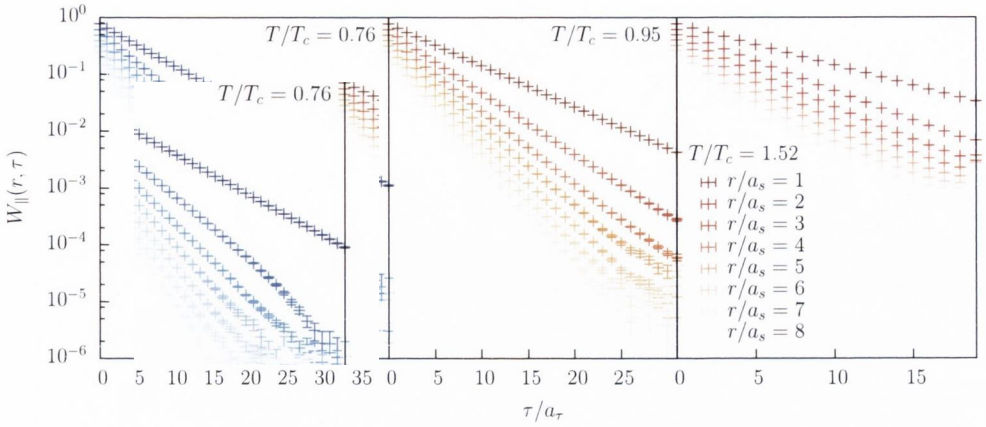

Figure 4.2: The Wilson line correlators with increasing temperature from left to right, which already suggests the salient temperature-dependence of the real part of the potential.

correlator. A typical trajectory of the gauge-fixing violation is visible in the appendix.

The correlators were then computed on four of the available temperatures, $T/T_c = 0.76$, 0.95, 1.52 and $T/T_c = 1.90$, which span the accessible temperature range. Separations of up to $r/a_s = 8$ were computed, which amounts to 54 distinct displacements upon including both on and off-axis measurements. A comparison between the Wilson loop and Wilson line correlators at $T/T_c = 1.90$ with the same number of measurements is shown in figure 4.1 for a selection of spatial separations. It is evident that the Wilson line correlator is much less suppressed than the Wilson loop and is less susceptible to lattice artifacts in the short-distance part of the correlator which hamper the extraction of the signal.

The Wilson line correlators are depicted for the other temperatures in figure 4.2 where the qualitative features of the rising potential are visible as the correlator decays faster as the distance is increased. Furthermore, the temperature dependence already signals that the potential becomes suppressed as is visible from the weakening of the decay with increasing temperature.

4.1.3 Spectral reconstructions and potential from the Bayesian reconstruction

Due to the deficiencies observed in reconstructing the hard-thermal loop spectral functions with MEM, the Bayesian reconstruction is the preferred implementation for the extraction of the potential from lattice data. The reconstruction proceeds exactly as for the heavy quarkonium correlators of the previous chap-

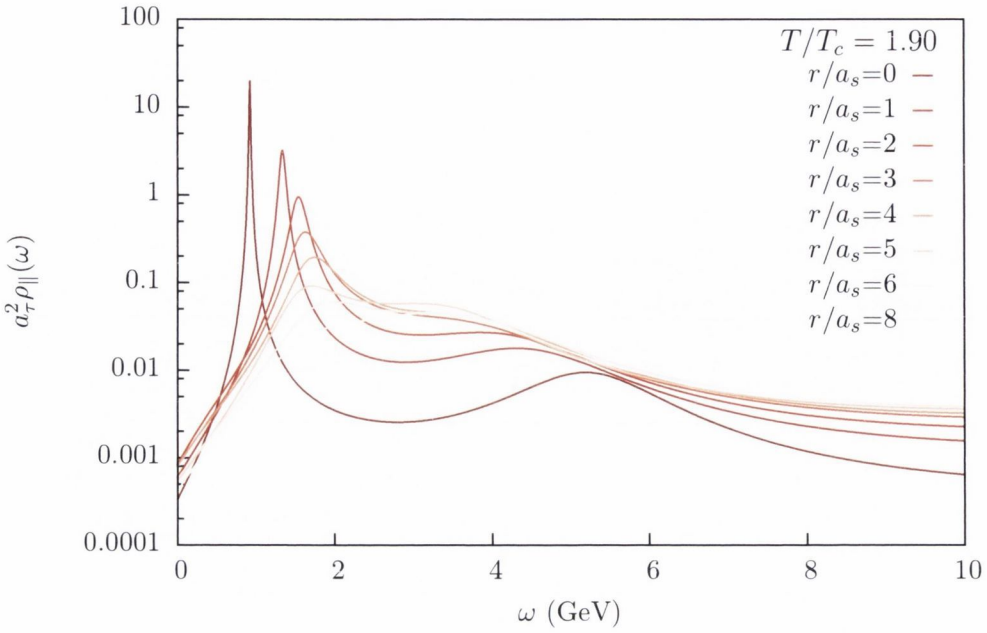

Figure 4.3: The reconstructed spectral function of the Wilson line correlators using the BR method (section 2.3.6) at $T/T_c = 1.50$, which illustrates the typical dependence of the lowest peak height and width on the separation, r.

ter. Parameters used in the reconstruction are listed in table A.4. A sample of the reconstructed spectral function is shown in figure 4.3 at the highest available temperature, $T/T_c = 1.90$. With increasing separation, three effects are noted on the lowest peak, namely the suppression of the peak height, the shift in the peak position and the growth in the width, which signals the increasing real and imaginary parts of the potential. The spectral reconstructions and their fits used to obtain the potentials in figures 4.4 and 4.5 were performed by A. Rothkopf.

The potential obtained from the fits of the Lorentzian lineshape and skewed Lorentzian background with constant background are compared for the highest temperature, $T/T_c = 1.90$ in figure 4.4. The systematic difference between the functional fit form, which is not accountable within the statistical errors, are reminiscent of the discrepancy observed between the fits for the Wilson loop data in ref. [154] which was caused by the failure of the reconstruction, MEM in that case. It can be guessed already from figure 4.3 that the spectral lineshape does not adhere to a Lorentzian or some small deformation of one at large separations. Obviously, at higher temperatures the possibility of the dominance of discretization effects ought to become troubling. Evidence that the features of the spectral function are not well separated from the continuum at high frequencies should raise questions of the systematic effects of the reconstruction. The qualitative

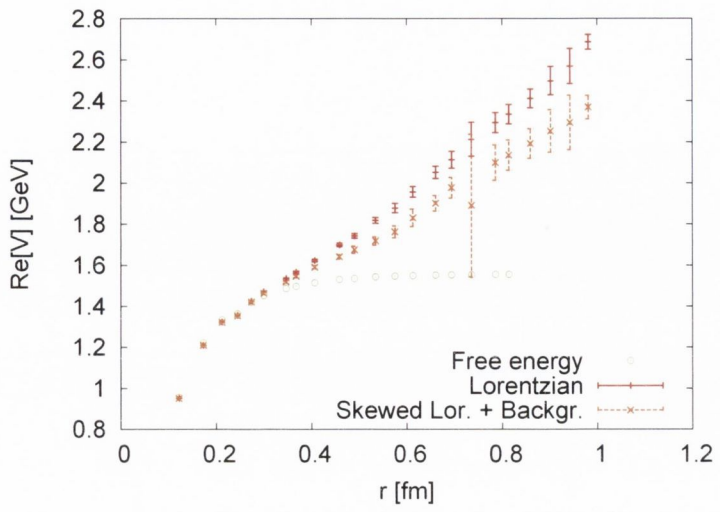

Figure 4.4: Comparison betweeen the real part of the potential obtained at the highest available temperature, $1.90T_c$, using the naive Lorentzian parameterizations of the lineshape (red points) and the skewing Lorentzian with constant background term (orange points). The free energy is also depicted for comparison (green points), showing a very different qualitative behaviour at this temperature. Figure provided courtesy of A. Rothkopf.

behaviour of the colour-singlet free energy is remarkably different and reiterates the importance of identifying the correct potential.

The temperature-dependence of the extracted potential is shown in figure 4.5. At separations of $r \leq 0.6$fm, the ordering of the real part of the potential adheres to the expectation of screening of the potential in the deconfined phase. However, beyond these separations the persistent linear rise of the real part at the highest temperature must be treated with skepticism.

Although increased measurements may alleviate some of the difficulties of the reconstruction at high temperatures where there are few correlator data which encode the physical potential, the suggestion that reconstructions of the spectral functions at the highest available temperature are strongly afflicted by lattice artifacts cannot be escaped. In that light, the strong rise in the imaginary part of the potential, which considerably overshoots the hard-thermal loop result [154]. The successful reconstruction of the heavy-quark potential allows for the extraction of the Debye mass and further work but further work is required to pin down the discretization effects in the lattice observable before such quantitative tests make sense. Nevertheless, this type of study demonstrates the feasibility of using

the reconstruction to extract valuable information on the heavy-quark potential from lattice QCD from relatively inexpensive obervables at finite temperature, whose development will continue to enrich the study of heavy-quark probes at finite temperature.

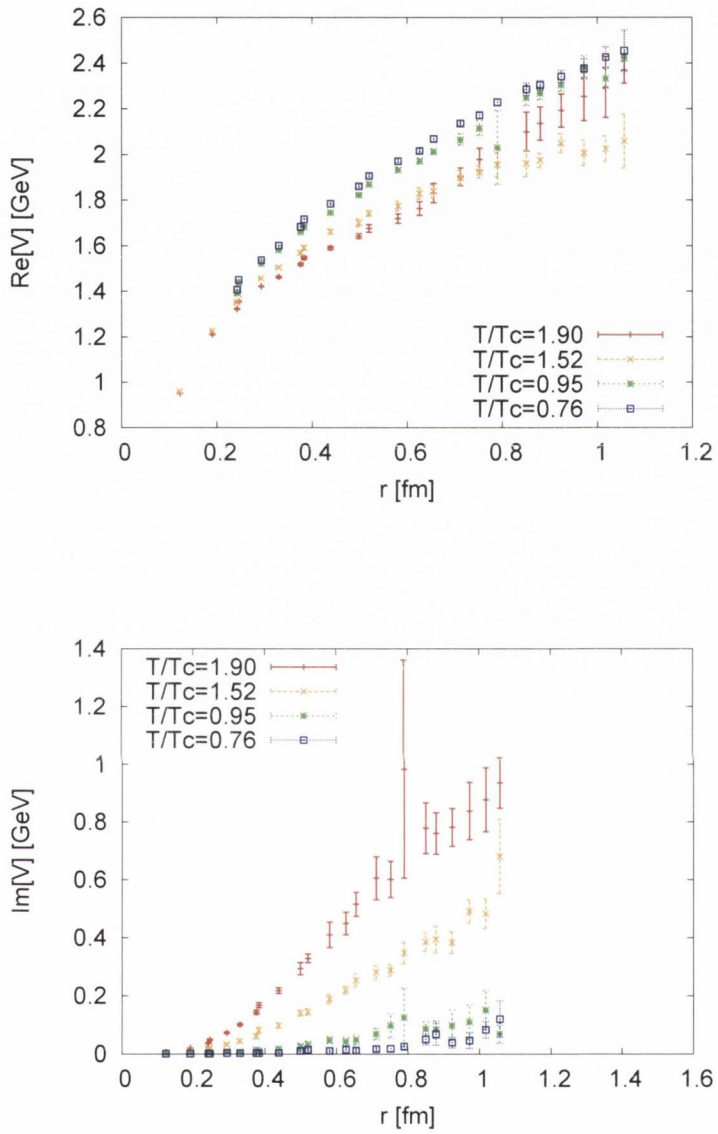

Figure 4.5: Temperature-dependence of the real (top) and imaginary (bottom) parts of the potential. Although a comparison with the hard-thermal loop potential [56, 154] is not explicitly shown, the imaginary part (right) of the potential overshoots this value considerably at the higher temperatures, $T/T_c = 1.52$ (orange) and $T/T_c = 1.90$ (red). Figure reproduced with kind permission of A. Rothkopf.

5 Conclusions

This work began with a review of the phenomenology of QCD at finite temperature which motivated the non-perturbative investigation of quarkonium correlators and spectral functions from first principles. Reliable data from lattice QCD could aid the interpretation of signals for the formation of a new phase of matter at high temperatures, such as the suppression of quarkonium yields, through the examination of the binding properties of heavy quarks in a thermal medium. A discretized version of NRQCD was used to perform a numerical study of bottomonium in an S wave and P wave channel above and below the deconfinement transition temperature using ensembles generated by the FASTSUM collaboration. Such a numerical approach is complementary to existing weak-coupling analyses.

The details of the lattice discretization were presented in the chapter 2 in which a cursory investigation of the zero-temperature bottomonium spectrum demonstrated the satisfactory performance of the effective theory. Two strategies, MEM and the BR method, were reviewed which address the challenges of extracting real-time observables from the Euclidean theory. The application of these methods to the Euclidean correlator data demonstrated the viability of both regularizations to solve the inverse problem at zero temperature. The systematic differences of the reconstructions using both methods were discussed, and the deficiencies of the MEM in certain cases were highlighted.

In chapter 3, an examination of the bottomonium correlation functions at finite temperature suggested different qualitative behaviour in the S wave and P wave channels above the deconfinement crossover temperature. Comparing with the behaviour of free heavy quarks, the ground-state S wave appeared unaltered but indications of unbinding of the heavy quarks in the P wave channel were observed in the deconfined phase. However, some difficulties were encountered in interpreting these results. This motivated the extraction of the spectral functions using both methods outlined in chapter 2. The MEM appeared to give results consistent with the analysis of the correlators regarding the survival of the

ground-state S wave up to $1.90T_c$ and the dissociation of the P wave state immediately in the deconfined phase. The conclusions from the BR method yielded incompatible results in the P wave channel, which suggested that this state may surive well into the plasma phase. However, the systematic dependence of the reconstruction on the available data reiterated the difficulty of performing the reconstruction on small temporal extents where lattice artifacts may dominate most of the signal. Further comparison with other discretizations should prove fruitful.

Finally, in the last chapter, preliminary results on the heavy-quark potential were obtained by employing the BR method to reconstruct the spectral function of a Wilson line correlator. Above the crossover temperature a screened potential with a finite imaginary part was observed. In a weakly-coupled plasma such effects may be interpreted as due to Debye screening and Landau damping respectively. At the highest temperature, the reconstruction was afflicted by systematic effects which require further investigation. Hopefully, the continuation of the work initiated in this study should help to clarify the performance of reconstruction of the closely related observables of the quarkonium spectral functions and the heavy-quark potential. The complementary nature of their systematic uncertainties should allow robust conclusions to be drawn from lattice studies on the fate of heavy quarkonium in the quark-gluon plasma.

Bibliography

[1] D. Gross and F. Wilczek, *Ultraviolet Behavior of Nonabelian Gauge Theories*, *Physical Review Letters* **30** (1973) 1343–1346.

[2] H. D. Politzer, *Reliable Perturbative Results for Strong Interactions?*, *Physical Review Letters* **30** (1973) 1346–1349.

[3] K. G. Wilson, *Confinement of quarks*, *Physical Review* **D10** (Oct., 1974) 2445–2459.

[4] A. Bazavov, T. Bhattacharya, M. Cheng, C. Detar, H.-T. Ding, S. Gottlieb, R. Gupta, P. Hegde, U. M. Heller, F. Karsch, E. Laermann, L. Levkova, S. Mukherjee, P. Petreczky, C. Schmidt, R. A. Soltz, W. Soeldner, R. Sugar, D. Toussaint, W. Unger and P. Vranas, *Chiral and deconfinement aspects of the QCD transition*, *Physical Review* **D85** (Mar., 2012) 054503 [arXiv:1111.1710].

[5] A. Mocsy, *Potential Models for Quarkonia*, *Eur.Phys.J.* **C61** (2009) 705–710 [arXiv:0811.0337].

[6] R. Hagedorn *Nuovo Cim. Suppl.* **3** (1965) 147.

[7] O. Kaczmarek, F. Karsch, P. Petreczky and F. Zantow, *Heavy quark anti-quark free energy and the renormalized Polyakov loop*, *Phys.Lett.* **B543** (2002) 41–47 [arXiv:hep-lat/0207002].

[8] L. D. McLerran and B. Svetitsky, *A Monte Carlo Study of SU(2) Yang-Mills Theory at Finite Temperature*, *Phys.Lett.* **B98** (1981) 195.

[9] S. Nadkarni, *Non-abelian debye screening: The color-averaged potential*, *Phys. Rev. D* **33** (Jun, 1986) 3738–3746.

[10] P. Petreczky, *Lattice QCD at non-zero temperature*, *J.Phys.* **G39** (2012) 093002 [arXiv:1203.5320].

[11] S. Sharma, *QCD Thermodynamics on the Lattice*, *Adv.High Energy Phys.* **2013** (2013) 452978 [arXiv:1403.2102].

[12] P. de Forcrand, S. Kim and O. Philipsen, *A QCD chiral critical point at small chemical potential: Is it there or not?*, *PoS* **LAT2007** (2007) 178 [arXiv:0711.0262].

[13] S. Digal, E. Laermann and H. Satz, *Deconfinement through chiral symmetry restoration in two flavor QCD*, *Eur.Phys.J.* **C18** (2001) 583–586 [arXiv:hep-ph/0007175].

[14] V. Dick, F. Karsch, E. Laermann, H. Sandmeyer, S. Sharma *et al.*, *Hadronic Correlators and Symmetries*, *Acta Phys.Polon.Supp.* **7** (2014), no. 1 27–34.

[15] H. Satz, *Calibrating the In-Medium Behavior of Quarkonia*, *Adv.High Energy Phys.* **2013** (2013) 242918 [arXiv:1303.3493].

[16] M. Cristoforetti, F. Di Renzo, A. Mukherjee and L. Scorzato, *Lefschetz thimbles and sign problem: first results in 0 and 4 dimensional field theories*, *PoS* **QCD-TNT-III** (2013) 010.

[17] G. Aarts, E. Seiler, D. Sexty and I.-O. Stamatescu, *Simulating QCD at nonzero baryon density to all orders in the hopping parameter expansion*, arXiv:1408.3770.

[18] A. Cherman, D. Dorigoni and M. Unsal, *Decoding perturbation theory using resurgence: Stokes phenomena, new saddle points and Lefschetz thimbles*, arXiv:1403.1277.

[19] U. W. Heinz, *Concepts of heavy ion physics*, arXiv:hep-ph/0407360.

[20] **STAR Collaboration**, J. Adams *et al.*, *Experimental and theoretical challenges in the search for the quark gluon plasma: The STAR Collaboration's critical assessment of the evidence from RHIC collisions*, *Nucl.Phys.* **A757** (2005) 102–183 [arXiv:nucl-ex/0501009].

[21] P. Kovtun, D. T. Son and A. O. Starinets, *Viscosity in strongly interacting quantum field theories from black hole physics*, *Phys.Rev.Lett.* **94** (2005) 111601 [arXiv:hep-th/0405231].

[22] E. Shuryak, *Why does the quark gluon plasma at RHIC behave as a nearly ideal fluid?*, *Prog.Part.Nucl.Phys.* **53** (2004) 273–303 [arXiv:hep-ph/0312227].

[23] S. I. Finazzo and J. Noronha, *Estimates for the Thermal Width of Heavy Quarkonia in Strongly Coupled Plasmas from Holography*, *JHEP* **1311** (2013) 042 [arXiv:1306.2613].

[24] G. Bergner, P. Giudice, G. Münster, S. Piemonte and D. Sandbrink, *Phase structure of the N=1 supersymmetric Yang-Mills theory at finite temperature*, arXiv:1405.3180.

[25] S. Borsanyi, Z. Fodor, C. Hoelbling, S. D. Katz, S. Krieg *et al.*, *Continuum EoS for QCD with $Nf = 2 + 1$ flavors*, *PoS* **LATTICE2013** (2013) 155 [arXiv:1312.2193].

[26] H. B. Meyer, *Transport Properties of the Quark-Gluon Plasma: A Lattice QCD Perspective*, *Eur.Phys.J.* **A47** (2011) 86 [arXiv:1104.3708].

[27] M. Panero, K. Rummukainen and A. Schäfer, *Jet quenching from the lattice*, arXiv:1407.2963.

[28] M. Laine and A. Rothkopf, *Towards understanding thermal jet quenching via lattice simulations*, *PoS* **LATTICE2013** (2013) 174 [arXiv:1310.2413].

[29] A. Bazavov, H. T. Ding, P. Hegde, O. Kaczmarek, F. Karsch *et al.*, *Strangeness at high temperatures: from hadrons to quarks*, *Phys. Rev. Lett. 111*, **082301** (2013) 082301 [arXiv:1304.7220].

[30] S. Borsanyi, Z. Fodor, S. Katz, S. Krieg, C. Ratti *et al.*, *Freeze-out parameters from electric charge and baryon number fluctuations: is there consistency?*, *Phys.Rev.Lett.* **113** (2014) 052301 [arXiv:1403.4576].

[31] F. Karsch, *Determination of Freeze-out Conditions from Lattice QCD Calculations*, *Central Eur.J.Phys.* **10** (2012) 1234–1237 [arXiv:1202.4173].

[32] H.-T. Ding, *Hard and thermal probes of QGP from the perspective of Lattice QCD*, arXiv:1404.5134.

[33] T. Matsui and H. Satz, *J/ψ Suppression by Quark-Gluon Plasma Formation*, *Phys.Lett.* **B178** (1986) 416.

[34] F. Karsch, D. Kharzeev and H. Satz, *Sequential charmonium dissociation*, *Phys.Lett.* **B637** (2006) 75–80 [arXiv:hep-ph/0512239].

[35] L. Kluberg, *20 years of j/ψ suppression at the cern sps*, *The European Physical Journal C - Particles and Fields* **43** (2005), no. 1-4 145–156.

[36] R. Vogt, *Cold Nuclear Matter Effects on J/ψ and Υ Production at the LHC*, *Phys.Rev.* **C81** (2010) 044903 [arXiv:1003.3497].

[37] R. Rapp, D. Blaschke and P. Crochet, *Charmonium and bottomonium production in heavy-ion collisions*, *Prog.Part.Nucl.Phys.* **65** (2010) 209–266 [arXiv:0807.2470].

[38] S. Digal, P. Petreczky and H. Satz, *Quarkonium feed down and sequential suppression*, *Phys.Rev.* **D64** (2001) 094015 [arXiv:hep-ph/0106017].

[39] A. Abdulsalam and P. Shukla, *Suppression of bottomonia states in finite size quark gluon plasma in PbPb collisions at Large Hadron Collider*, *Int.J.Mod.Phys.* **A28** (2013) 1350105 [arXiv:1210.7584].

[40] **CMS Collaboration**, Z. Hu and t. C. collaboration, *Observation of sequential Υ suppression in PbPb collisions*, *J.Phys.Conf.Ser.* **446** (2013) 012043.

[41] M. Strickland and D. Bazow, *Thermal Bottomonium Suppression at RHIC and LHC*, *Nucl.Phys.* **A879** (2012) 25–58 [arXiv:1112.2761].

[42] P. Braun-Munzinger and J. Stachel, *(Non)thermal aspects of charmonium production and a new look at J / psi suppression*, *Phys.Lett.* **B490** (2000) 196–202 [arXiv:nucl-th/0007059].

[43] L. D. McLerran and T. Toimela, *Photon and Dilepton Emission from the Quark - Gluon Plasma: Some General Considerations*, *Phys.Rev.* **D31** (1985) 545.

[44] **PHENIX Collaboration**, A. Adare *et al.*, *Measurement of Υ(1S+2S+3S) production in p+p and Au+Au collisions at $\sqrt{s_{NN}} = 200$ GeV*, arXiv:1404.2246.

[45] **STAR Collaboration**, L. Adamczyk *et al.*, *Suppression of Upsilon Production in d+Au and Au+Au Collisions at $\sqrt{(s_{NN})} = 200GeV$*, *Phys.Lett.* **B735** (2014) 127 [arXiv:1312.3675].

[46] J. I. Kapusta and C. Gale, *Finite-Temperature Field Theory: Principles and Applications*. Cambridge University Press, 2006.

[47] M. Le Bellac, *Thermal Field Theory*. Cambridge University Press, 1996.

[48] G. P. Lepage, L. Magnea, C. Nakhleh, U. Magnea and K. Hornbostel, *Improved nonrelativistic QCD for heavy quark physics*, *Phys.Rev.* **D46** (1992) 4052–4067 [arXiv:hep-lat/9205007].

[49] E. Braaten, *Introduction to the NRQCD Factorization Approach to Heavy Quarkonium*, arXiv:hep-ph/9702225.

[50] **ALPHA**, J. Heitger and R. Sommer, *Nonperturbative heavy quark effective theory*, *JHEP* **0402** (2004) 022 [arXiv:hep-lat/0310035].

[51] S. Bekavac, A. Grozin, P. Marquard, J. Piclum, D. Seidel *et al.*, *Matching QCD and HQET heavy-light currents at three loops*, *Nucl.Phys.* **B833** (2010) 46–63 [arXiv:0911.3356].

[52] L. L. Foldy and S. A. Wouthuysen, *On the dirac theory of spin 1/2 particles and its non-relativistic limit*, *Phys. Rev.* **78** (Apr, 1950) 29–36.

[53] M. Laine, *A Resummed perturbative estimate for the quarkonium spectral function in hot QCD*, *JHEP* **0705** (2007) 028 [arXiv:0704.1720].

[54] Y. Burnier, M. Laine and M. Vepsalainen, *Heavy quarkonium in any channel in resummed hot QCD*, *JHEP* **0801** (2008) 043 [arXiv:0711.1743].

[55] C. Davies and B. Thacker, *Heavy quark renormalization parameters in nonrelativistic QCD*, *Phys.Rev.* **D45** (1992) 915–923.

[56] M. Laine, O. Philipsen, P. Romatschke and M. Tassler, *Real-time static potential in hot QCD*, *JHEP* **0703** (2007) 054 [arXiv:hep-ph/0611300].

[57] A. Bazavov, F. Karsch, Y. Maezawa, S. Mukherjee and P. Petreczky, *In-medium meson properties and screening correlators*, *J.Phys.Conf.Ser.* **535** (2014) 012031.

[58] W. Florkowski and B. L. Friman, *Spatial dependence of the finite temperature meson correlation function*, *Z.Phys.* **A347** (1994) 271–276.

[59] Y. Maezawa, A. Bazavov, F. Karsch, P. Petreczky and S. Mukherjee, *Meson screening masses at finite temperature with Highly Improved Staggered Quarks*, *PoS* **LATTICE2013** (2013) 149 [arXiv:1312.4375].

[60] G. Aarts, "Private correspondence.".

[61] E. Eichten, K. Gottfried, T. Kinoshita, K. Lane and T.-M. Yan, *Charmonium: Comparison with Experiment*, *Phys.Rev.* **D21** (1980) 203.

[62] O. Kaczmarek, *Heavy-quark free energies, internal-energy and entropy contributions*, *Eur.Phys.J.* **C61** (2009) 811–817.

[63] C.-Y. Wong, *Heavy quarkonia in quark-gluon plasma*, *Phys.Rev.* **C72** (2005) 034906 [arXiv:hep-ph/0408020].

[64] Á. Mócsy and P. Petreczky, *Color screening melts quarkonium*, *Phys.Rev.Lett.* **99** (2007) 211602 [arXiv:0706.2183].

[65] Á. Mócsy and P. Petreczky, *Can quarkonia survive deconfinement?*, *Phys.Rev.* **D77** (2008) 014501 [arXiv:0705.2559].

[66] W. Alberico, A. Beraudo, A. De Pace and A. Molinari, *Quarkonia in the deconfined phase: Effective potentials and lattice correlators*, *Phys.Rev.* **D75** (2007) 074009 [arXiv:hep-ph/0612062].

[67] N. Brambilla, A. Pineda, J. Soto and A. Vairo, *Effective field theories for heavy quarkonium*, *Rev.Mod.Phys.* **77** (2005) 1423 [arXiv:hep-ph/0410047].

[68] N. Brambilla, M. Groher, H. E. Martinez and A. Vairo, *Effective string theory and the long-range relativistic corrections to the quark-antiquark potential*, arXiv:1407.7761.

[69] P. Petreczky, C. Miao and Á. Mócsy, *Quarkonium spectral functions with complex potential*, *Nucl.Phys.* **A855** (2011) 125–132 [arXiv:1012.4433].

[70] A. Rothkopf, *A first look at Bottomonium melting via a stochastic potential*, arXiv:1312.3246.

[71] A. Rothkopf, *From Complex to Stochastic Potential: Heavy Quarkonia in the Quark-Gluon Plasma*, *Mod.Phys.Lett.* **A28** (2013) 1330005 [arXiv:1302.6195].

[72] R.-A. Tripolt, N. Strodthoff, L. von Smekal and J. Wambach, *Finite-Temperature Spectral Functions from the Functional Renormalization Group*, arXiv:1311.4304.

[73] H. Rothe, *Lattice Gauge Theories.* World Scientific, 2005.

[74] C. Gattringer and L. C, *Quantum Chromodynamics on the Lattice: An Introductory Presentation.* Springer, 2010.

[75] M. Luscher and S. Schaefer, *Lattice QCD with open boundary conditions and twisted-mass reweighting*, *Comput.Phys.Commun.* **184** (2013) 519–528 [arXiv:1206.2809].

[76] J. J. Binney, N. J. Dorwick, A. J. Fisher and M. E. J. Newman, *The Theory of Critical Phenomena: An Introduction to the Renormalization Group.* Oxford University Press, 1992.

[77] M. Luscher, *Volume Dependence of the Energy Spectrum in Massive Quantum Field Theories. 1. Stable Particle States, Commun.Math.Phys.* **104** (1986) 177.

[78] **ALPHA Collaboration**, S. Schaefer, R. Sommer and F. Virotta, *Critical slowing down and error analysis in lattice QCD simulations, Nucl.Phys.* **B845** (2011) 93–119 [arXiv:1009.5228].

[79] K. Symanzik, *Continuum Limit and Improved Action in Lattice Theories. 1. Principles and phi**4 Theory, Nuclear Physics* **B226** (1983) 187.

[80] M. Lüscher and P. Weisz, *On-Shell Improved Lattice Gauge Theories, Communications in Mathematical Physics* **97** (1985) 59.

[81] G. P. Lepage and P. B. Mackenzie, *On the viability of lattice perturbation theory, Physical Review* **D48** (1993) 2250–2264 [arXiv:hep-lat/9209022].

[82] G. Lepage, *Redesigning lattice QCD*, in *Lecture Notes in Physics, Berlin Springer Verlag* (H. Latal and W. Schweiger, eds.), vol. 479 of *Lecture Notes in Physics, Berlin Springer Verlag*, p. 1, 1997. arXiv:hep-lat/9607076.

[83] P. Chen, *Heavy quarks on anisotropic lattices: the charmonium spectrum, Physical Review* **D64** (Aug., 2001) 034509 [arXiv:hep-lat/0006019].

[84] **Hadron Spectrum Collaboration**, L. Liu *et al.*, *Excited and exotic charmonium spectroscopy from lattice QCD, JHEP* **1207** (2012) 126 [arXiv:1204.5425].

[85] **RBC Collaboration, UKQCD Collaboration**, Y. Aoki *et al.*, *Nonperturbative tuning of an improved relativistic heavy-quark action with application to bottom spectroscopy, Physical Review* **D86** (2012) 116003 [arXiv:1206.2554].

[86] **TrinLat Collaboration**, J. Foley, A. O'Cais, M. Peardon and S. M. Ryan, *A Non-perturbative study of the action parameters for anisotropic-lattice quarks, Physical Review* **D73** (2006) 014514 [arXiv:hep-lat/0405030].

[87] C. Morningstar and M. Peardon, *Efficient glueball simulations on anisotropic lattices*, *Physical Review* **D56** (Oct., 1997) 4043–4061 [arXiv:hep-lat/9704011].

[88] C. Morningstar and M. Peardon, *Analytic smearing of* SU(3) *link variables in lattice QCD*, *Physical Review* **D69** (Mar, 2004) 054501.

[89] M. Clark, *The Rational Hybrid Monte Carlo Algorithm*, *Proceedings of Science* **LAT2006** (2006) 004 [arXiv:hep-lat/0610048].

[90] T. R. Klassen, *The Anisotropic Wilson gauge action*, *Nuclear Physics* **B533** (1998) 557–575 [arXiv:hep-lat/9803010].

[91] R. Morrin, A. Ó Cais, M. Peardon, S. M. Ryan and J.-I. Skullerud, *Dynamical QCD simulations on anisotropic lattices*, *Phys.Rev.* **D74** (2006) 014505 [arXiv:hep-lat/0604021].

[92] M. B. Oktay and J.-I. Skullerud, *Momentum-dependence of charmonium spectral functions from lattice QCD*, arXiv:1005.1209.

[93] G. Aarts, S. Kim, M. Lombardo, M. Oktay, S. Ryan *et al.*, *Bottomonium above deconfinement in lattice nonrelativistic QCD*, *Phys.Rev.Lett.* **106** (2011) 061602 [arXiv:1010.3725].

[94] G. Aarts, C. Allton, S. Kim, M. Lombardo, M. Oktay *et al.*, *What happens to the* Υ *and* η_b *in the quark-gluon plasma? Bottomonium spectral functions from lattice QCD*, *JHEP* **1111** (2011) 103 [arXiv:1109.4496].

[95] G. Aarts, C. Allton, S. Kim, M. P. Lombardo, M. B. Oktay *et al.*, *S wave bottomonium states moving in a quark-gluon plasma from lattice NRQCD*, *JHEP* **1303** (2013) 084 [arXiv:1210.2903].

[96] G. Aarts, C. Allton, S. Kim, M. Lombardo, S. Ryan *et al.*, *Melting of P wave bottomonium states in the quark-gluon plasma from lattice NRQCD*, *JHEP* **1312** (2013) 064 [arXiv:1310.5467].

[97] C. Davies, K. Hornbostel, A. Langnau, G. Lepage, A. Lidsey *et al.*, *Precision Upsilon spectroscopy from nonrelativistic lattice QCD*, *Phys.Rev.* **D50** (1994) 6963–6977 [arXiv:hep-lat/9406017].

[98] **HPQCD**, R. Dowdall, C. Davies, T. Hammant and R. Horgan, *Bottomonium hyperfine splittings from lattice nonrelativistic QCD including radiative and relativistic corrections*, *Phys.Rev.* **D89** (2014), no. 3 031502 [arXiv:1309.5797].

[99] B. Colquhoun, R. Dowdall, C. Davies, K. Hornbostel and G. Lepage, *The Υ and Υ' Leptonic Widths, a_μ^b and m_b from full lattice QCD*, arXiv:1408.5768.

[100] W. Detmold, S. Meinel and Z. Shi, *Quarkonium at non-zero isospin density*, arXiv:1211.3156.

[101] E. H. Muller, C. T. Davies, A. Hart, G. M. von Hippel, R. R. Horgan *et al.*, *Radiative corrections to the m(oving)NRQCD action and heavy-light operators*, *PoS* **LAT2009** (2009) 241 [arXiv:0909.5126].

[102] G. Moir, M. Peardon, S. M. Ryan, C. E. Thomas and L. Liu, *Excited spectroscopy of charmed mesons from lattice QCD*, *JHEP* **1305** (2013) 021 [arXiv:1301.7670].

[103] R. Lewis and R. Woloshyn, *Higher angular momentum states of bottomonium in lattice NRQCD*, *Phys.Rev.* **D85** (2012) 114509 [arXiv:1204.4675].

[104] M. Wurtz, R. Lewis and R. Woloshyn, *Free-form Smeared Bottomonium Correlation Functions*, arXiv:1409.7103.

[105] **HPQCD Collaboration**, C. Davies, E. Follana, I. Kendall, G. P. Lepage and C. McNeile, *Precise determination of the lattice spacing in full lattice QCD*, *Phys.Rev.* **D81** (2010) 034506 [arXiv:0910.1229].

[106] F. James, *RANLUX: A FORTRAN implementation of the high quality pseudorandom number generator of Luscher*, *Comput.Phys.Commun.* **79** (1994) 111–114.

[107] L. Giusti, M. Paciello, C. Parrinello, S. Petrarca and B. Taglienti, *Problems on lattice gauge fixing*, *Int.J.Mod.Phys.* **A16** (2001) 3487–3534 [arXiv:hep-lat/0104012].

[108] W. Press, S. Teukolsky, W. Vetterling and B. Flannery, *Numerical Recipes 3rd Edition: The Art of Scientific Computing*. Cambridge University Press, 2007.

[109] **HPQCD Collaboration**, R. Dowdall *et al.*, *The Υ spectrum and the determination of the lattice spacing from lattice QCD including charm quarks in the sea*, *Phys.Rev.* **D85** (2012) 054509 [arXiv:1110.6887].

[110] **Particle Data Group**, J. Beringer *et al.*, *Review of Particle Physics (RPP)*, *Phys.Rev.* **D86** (2012) 010001.

[111] K. Hornbostel, G. Lepage, C. Davies, R. Dowdall, H. Na *et al.*, *Fast fits for lattice QCD correlators*, *Phys.Rev.* **D85** (2012) 031504 [arXiv:1111.1363].

[112] P. J. Silva, D. Dudal and O. Oliveira, *Spectral densities from the lattice*, arXiv:1311.3643.

[113] A. Kirsch, *Introduction to the Mathematical Theory of Inverse Problems*. Springer New York.

[114] O. Kaczmarek and M. Müller, *Temperature dependence of electrical conductivity and dilepton rates from hot quenched lattice QCD*, *PoS* **LATTICE2013** (2013) 175 [arXiv:1312.5609].

[115] M. Asakawa, T. Hatsuda and Y. Nakahara, *Maximum entropy analysis of the spectral functions in lattice QCD*, *Prog.Part.Nucl.Phys.* **46** (2001) 459–508 [arXiv:hep-lat/0011040].

[116] D. Nickel, *Extraction of Spectral Functions from Dyson-Schwinger Studies via the Maximum Entropy Method*, *Annals Phys.* **322** (2007) 1949–1960 [arXiv:hep-ph/0607224].

[117] R. Bryan, *Maximum entropy analysis of oversampled data problems*, *European Biophysics Journal* **18** (1990), no. 3 165–174.

[118] C. Allton, D. Blythe and J. Clowser, *Spectral functions, maximum entropy method and unconventional methods in lattice field theory*, *Nucl.Phys.Proc.Suppl.* **109A** (2002) 192–196 [arXiv:hep-lat/0202024].

[119] A. Rothkopf, *Improved maximum entropy method with an extended search space*, arXiv:1208.5162.

[120] Y. Burnier and A. Rothkopf, *Bayesian Approach to Spectral Function Reconstruction for Euclidean Quantum Field Theories*, *Phys.Rev.Lett.* **111** (2013), no. 18 182003 [arXiv:1307.6106].

[121] S. Bochkanov and V. Bystritsky, *Alglib*, 1999.

[122] T. Matsubara, *A New approach to quantum statistical mechanics*, *Prog.Theor.Phys.* **14** (1955) 351–378.

[123] L. Giusti and H. B. Meyer, *Implications of Poincare symmetry for thermal field theories in finite-volume*, *JHEP* **1301** (2013) 140 [arXiv:1211.6669].

[124] **HotQCD Collaboration**, A. Bazavov *et al.*, *The equation of state in (2+1)-flavor QCD*, arXiv:1407.6387.

[125] A. Amato, G. Aarts, C. Allton, P. Giudice, S. Hands *et al.*, *Electrical conductivity of the quark-gluon plasma across the deconfinement transition*, *Phys.Rev.Lett.* **111** (2013) 172001 [arXiv:1307.6763].

[126] C. Allton, G. Aarts, A. Amato, W. Evans, P. Giudice *et al.*, *2+1 flavour thermal studies on an anisotropic lattice*, arXiv:1401.2116.

[127] R. G. Edwards, B. Joó and H.-W. Lin, *Tuning for three-flavors of anisotropic clover fermions with stout-link smearing*, *Phys.Rev.* **D78** (2008) 054501 [arXiv:0803.3960].

[128] S. Kim, P. Petreczky and A. Rothkopf, *Lattice NRQCD study of S- and P-wave bottomonium states in a thermal medium with $N_f = 2 + 1$ light flavors*, arXiv:1409.3630.

[129] S. Borsanyi, S. Durr, Z. Fodor, S. D. Katz, S. Krieg *et al.*, *Anisotropy tuning with the Wilson flow*, arXiv:1205.0781.

[130] **Wuppertal-Budapest Collaboration**, S. Borsanyi *et al.*, *Is there still any T_c mystery in lattice QCD? Results with physical masses in the continuum limit III*, *JHEP* **1009** (2010) 073 [arXiv:1005.3508].

[131] O. Kaczmarek, *Continuum estimate of the heavy quark momentum diffusion coefficient κ*, arXiv:1409.3724.

[132] E. V. Shuryak, *Which chiral symmetry is restored in hot QCD?*, *Comments Nucl.Part.Phys.* **21** (1994) 235–248 [arXiv:hep-ph/9310253].

[133] M. I. Buchoff, M. Cheng, N. H. Christ, H. T. Ding, C. Jung *et al.*, *The QCD chiral transition, $U_A(1)$ symmetry and the Dirac spectrum using domain wall fermions*, *Phys.Rev.* **D89** (2014) 054514 [arXiv:1309.4149].

[134] A. Bazavov, H. T. Ding, P. Hegde, O. Kaczmarek, F. Karsch *et al.*, *The melting and abundance of open charm hadrons*, *Phys.Lett.* **B737** (2014) 210 [arXiv:1404.4043].

[135] M. Asakawa and T. Hatsuda, *J/ψ and η_c in the deconfined plasma from lattice QCD*, *Phys.Rev.Lett.* **92** (2004) 012001 [arXiv:hep-lat/0308034].

[136] S. Datta, F. Karsch, P. Petreczky and I. Wetzorke, *Behavior of charmonium systems after deconfinement*, *Phys.Rev.* **D69** (2004) 094507 [arXiv:hep-lat/0312037].

[137] A. Jakovác, P. Petreczky, K. Petrov and A. Velytsky, *Quarkonium correlators and spectral functions at zero and finite temperature*, *Phys.Rev.* **D75** (2007) 014506 [arXiv:hep-lat/0611017].

[138] G. Aarts, C. Allton, M. B. Oktay, M. Peardon and J.-I. Skullerud, *Charmonium at high temperature in two-flavor QCD*, *Phys.Rev.* **D76** (2007) 094513 [arXiv:0705.2198].

[139] H. Ding, A. Francis, O. Kaczmarek, F. Karsch, H. Satz *et al.*, *Charmonium properties in hot quenched lattice QCD*, *Phys.Rev.* **D86** (2012) 014509 [arXiv:1204.4945].

[140] H. Ohno, *Quarkonium correlation functions at finite temperature in the charm to bottom region*, arXiv:1311.4565.

[141] S. Borsányi, S. Dürr, Z. Fodor, C. Hoelbling, S. D. Katz *et al.*, *Charmonium spectral functions from 2+1 flavour lattice QCD*, arXiv:1401.5940.

[142] J. Fingberg, *Heavy quarkonia at high temperature*, *Phys.Lett.* **B424** (1998) 343–354 [arXiv:hep-lat/9707012].

[143] H. van Hees, V. Greco and R. Rapp, *Thermalization and flow of heavy quarks in the quark-gluon plasma*, *AIP Conf.Proc.* **842** (2006) 77–79 [arXiv:hep-ph/0601166].

[144] G. Aarts, C. Allton, S. Kim, M. P. Lombardo, M. B. Oktay, S. M. Ryan, D. K. Sinclair and J.-I. Skullerud, *What happens to the Υ and η_b in the quark-gluon plasma? Bottomonium spectral functions from lattice QCD*, *Journal of High Energy Physics* **11** (Nov., 2011) 103 [arXiv:1109.4496].

[145] G. Aarts, C. Allton, S. Kim, M. P. Lombardo, M. B. Oktay *et al.*, *Bottomonium at Non-zero Temperature from Lattice Non-relativistic QCD*, *AIP Conf.Proc.* **1441** (2012) 910–912 [arXiv:1109.1475].

[146] **UKQCD Collaboration**, G. Aarts and J. Foley, *Meson spectral functions with chirally symmetric lattice fermions*, *JHEP* **0702** (2007) 062 [arXiv:hep-lat/0612007].

[147] G. Aarts and J. M. Martinez Resco, *Continuum and lattice meson spectral functions at nonzero momentum and high temperature*, *Nucl.Phys.* **B726** (2005) 93–108 [arXiv:hep-lat/0507004].

[148] A. Hart, G. von Hippel, R. Horgan and E. Muller, *Automated generation of lattice QCD Feynman rules*, *Comput.Phys.Commun.* **180** (2009) 2698–2716 [arXiv:0904.0375].

[149] **WHOT-QCD Collaboration**, H. Ohno *et al.*, *Charmonium spectral functions with the variational method in zero and finite temperature lattice QCD*, *Phys.Rev.* **D84** (2011) 094504 [arXiv:1104.3384].

[150] T. Umeda, *A Constant contribution in meson correlators at finite temperature*, *Phys.Rev.* **D75** (2007) 094502 [arXiv:hep-lat/0701005].

[151] S. Kim, G. Aarts, C. Allton, M. P. Lombardo, M. B. Oktay *et al.*, *Two topics from lattice NRQCD at non-zero temperature: heavy quark mass dependence and S-wave bottomonium states moving in a thermal bath*, *PoS* **LATTICE2012** (2012) 086 [arXiv:1210.7586].

[152] S. Kim, P. Petreczky and A. Rothkopf, *Lattice NRQCD study of in-medium bottomonium states using $N_f = 2 + 1, 48^3 \times 12$ HotQCD configurations*, arXiv:1310.6461.

[153] H. Satz, *Heavy Quark Interactions and Quarkonium Binding*, *J.Phys.* **G36** (2009) 064011 [arXiv:0812.3829].

[154] Y. Burnier and A. Rothkopf, *A hard thermal loop benchmark for the extraction of the nonperturbative $Q\bar{Q}$ potential*, *Phys.Rev.* **D87** (2013), no. 11 114019 [arXiv:1304.4154].

[155] A. Rothkopf, T. Hatsuda and S. Sasaki, *Proper heavy-quark potential from a spectral decomposition of the thermal Wilson loop*, *PoS* **LAT2009** (2009) 162 [arXiv:0910.2321].

[156] Y. Burnier and A. Rothkopf, *Disentangling the timescales behind the non-perturbative heavy quark potential*, *Phys.Rev.* **D86** (2012) 051503 [arXiv:1208.1899].

[157] A. Beraudo, J.-P. Blaizot and C. Ratti, *Real and imaginary-time Q anti-Q correlators in a thermal medium*, *Nucl.Phys.* **A806** (2008) 312–338 [arXiv:0712.4394].

[158] A. Bazavov and P. Petreczky, *On static quark anti-quark potential at non-zero temperature*, *Nucl.Phys.* **A904-905** (2013) 599c–602c [arXiv:1210.6314].

[159] A. Bazavov, Y. Burnier and P. Petreczky, *Lattice calculation of the heavy quark potential at non-zero temperature*, arXiv:1404.4267.

[160] N. Su, *A brief overview of hard-thermal-loop perturbation theory*, *Commun.Theor.Phys.* **57** (2012) 409 [arXiv:1204.0260].

[161] Y. Burnier and A. Rothkopf, *Benchmarking the Bayesian reconstruction of the non-perturbative heavy $Q\bar{Q}$ potential*, *PoS* **LATTICE2013** (2014) 491 [arXiv:1310.0165].

A Auxiliary tables and figures

	$\Upsilon(^3S_1)$		$\chi_{b1}(^3P_1)$	
N_τ	$a_\tau\omega_1$, $a_\tau\omega_2$	$\tau_1/a_\tau, \tau_2/a_\tau$	$a_\tau\omega_1$, $a_\tau\omega_2$	$\tau_1/a_\tau, \tau_2/a_\tau$
128	0.12, 2.12	1, 127	0.18, 2.18	2, 110
40	0.08, 2.08	2, 38	0.16, 2.16	2, 38
36	0.08, 2.08	2, 34	0.16, 2.16	2, 34
32	0.08, 2.08	2, 30	0.16, 2.16	2, 30
28	0.08, 2.08	2, 26	0.10, 2.10	2, 26
24	0.08, 2.08	2, 22	0.08, 2.08	2, 22
20	0.00, 2.00	2, 18	0.00, 2.00	2, 18
16	-0.04, 1.96	2, 14	-0.04, 1.96	2, 14

Table A.1: Frequency and Euclidean time ranges used in MEM reconstruction of the spectral functions. The frequency interval is discretized into $N_\omega = 1000$ points for each N_τ.

	$\Upsilon(^3S_1)$		$\chi_{b1}(^3P_1)$	
N_τ	$a_\tau\omega_1$, $a_\tau\omega_2$	$\tau_1/a_\tau, \tau_2/a_\tau$	$a_\tau\omega_1$, $a_\tau\omega_2$	$\tau_1/a_\tau, \tau_2/a_\tau$
128	-0.2, 2.4	2, 127	-0.4, 2.4	2, 127
40	-0.2, 2.4	2, 39	-0.2, 2.4	2, 39
36	-0.2, 2.4	2, 35	-0.2, 2.4	2, 35
32	-0.2, 2.4	2, 31	-0.2, 2.4	2, 31
28	-0.2, 2.4	2, 27	-0.2, 2.4	2, 27
24	-0.2, 2.4	2, 23	-0.2, 2.4	2, 23
20	-0.4, 2.4	2, 19	-0.4, 2.4	2, 19
16	-0.4, 2.4	3, 15	-0.4, 2.4	2, 15

Table A.2: Frequency and Euclidean time ranges used in BR reconstruction of the spectral functions. The frequency interval is discretized into $N_\omega = 4000$ points for each N_τ.

J^{PC} (Λ^{PC})	$n^{2S+1}L_J$	$c_4 = 1$, $k = 1$		$c_4 = 1$, $k = 3$		$c_4 = 1.2$, $k = 1$	
		$a_\tau M_1$	$\mathcal{E} + M_1$ (GeV)	$a_\tau M_1$	$\mathcal{E} + M_1$ (GeV)	$a_\tau M_1$	$\mathcal{E} + M_1$ (GeV)
0^{-+}	1^1S_1	0.20549(4)	9409.7(2)	0.20521(5)	9407.1(3)	0.19694(4)	9388.2(2)
1^{--}	1^3S_1	0.21460(5)	9460*	0.21437(6)	9460*	0.20969(5)	9460*
1^{-+}	1^1P_1	0.2963(4)	9920(2)	0.2969(4)	9923(2)	0.2911(2)	9918(1)
0^{++}	1^3P_0	0.2920(3)	9896(2)	0.2924(4)	9898(2)	0.2864(2)	9891(1)
1^{++}	1^3P_1	0.2964(4)	9920(2)	0.2969(4)	9923(2)	0.2914(2)	9920(1)
2^{++}	1^3P_2	0.297(2)	9928(8)	0.298(2)	9932(9)	0.292(1)	9928(8)
(E^{++})	1^3P_2	0.2990(3)	9935(1)				
(T_2^{++})	1^3P_2	0.2975(3)	9927(2)				
0^{-+}	2^1S_1	0.311(3)	10003(14)				
1^{--}	2^3S_1	0.318(3)	10042(15)				

Table A.3: Estimates for the energies obtained by single and multi-exponential fits [111] to the NRQCD correlators used in figure 2.9. The experimental $\Upsilon(^3S_1)$ has been used to fix the NRQCD scale, $\mathcal{E} = M_{\text{expt}}(\Upsilon(^3S_1)) - M_1(\Upsilon(^3S_1))$. The spectrum was recalculated with Lepage's parameter set to $k = 3$ and no systematic differences were obtained. Setting the matching coefficient of the chromomagnetic operator, c_4, away from unity only affects the hyperfine splitting.

N_τ	N_{conf}	$a_\tau\omega_1, a_\tau\omega_2$	N_ω	N_{jack}	$m(\omega)$
$\{16, 20, 32, 40\}$	$\{890, 996, 987, 527\}$	$-10, 11.25$	4600	10	1

Table A.4: Parameters used in the Bayesian reconstruction of the Wilson line spectral function, where N_{conf} is the number of measurements used and N_{jack} is the number of jackknife blocks used to estimate the statistical uncertainties.

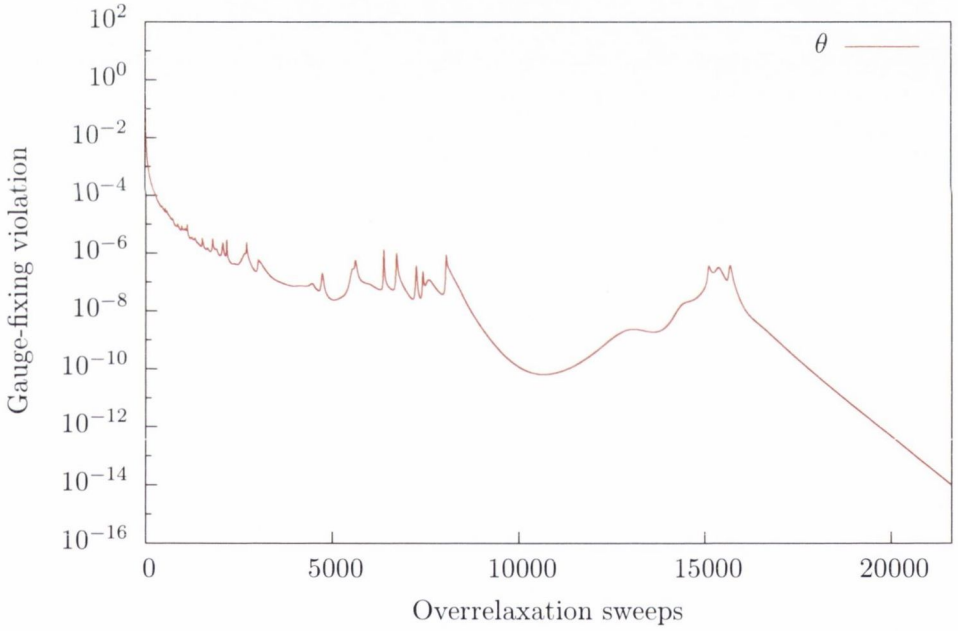

Figure A.1: Example of the behaviour of the typical behaviour of the gauge fixing violation with number of overrelation sweeps from a thermalized configuration on a $V = 24^3 \times 16$ volume with increased tolerance of $\theta < 10^{-14}$.